Ahn, Byung-Ho

ELECTRIC CONDUCTIVITIES, CURRENTS AND ENERGY DISSIPATION IN THE POLAR IONOSPHERE

University of Alaska

PH.D. 1983

ELECTRIC CONDUCTIVITIES, CURRENTS AND ENERGY DISSIPATION IN THE POLAR IONOSPHERE

A

THESIS

Presented to the Faculty of the University of Alaska

in Partial Fulfillment of the Requirements

for the Degree of

DOCTOR OF PHILOSOPHY

By

Byung-Ho Ahn, B.S., M.S.

Fairbanks, Alaska

May, 1983

ELECTRIC CONDUCTIVITIES, CURRENTS AND ENERGY

DISSIPATION IN THE POLAR IONOSPHERE

RECOMMENDED:

Joe-chuang Lee

Gary A. Gislason

Chairman, Advisory Committee

Head, Space Physics and Atmospheric Sciences Program

Director, Division of Geosciences

APPROVED:

for Vice Chancellor for Research and Advanced Study

May 6, 1983

Date

ABSTRACT

During the International Magnetospheric Study (IMS), magnetic records from the six IMS meridian chain stations were obtained on March 17, 18 and 19, 1978. The data set is one of the most comprehensive ever obtained. Furthermore, several advanced computer codes calculating ionospheric current distributions based on the ground magnetic data were recently introduced. Combining the data set and the computer code developed by Kamide et al. (1981), it is attempted to re-examine the longstanding uncertainties in the current distributions and the energy dissipation rates in the polar ionosphere during substorms.

For this purpose, a conductivity model which can reflect substorm conditions on an instantaneous basis was obtained based on the empirical relations of the north-south component (ΔH) of the magnetic disturbance field observed at College, with the Pedersen and Hall conductivities deduced from Chatanika radar observations. In addition, the relationship of the particle energy injection rate, estimated from the radar, to ΔH is also established. Based on the conductivity model thus obtained and the computer code, the ionospheric current distributions of 5-minute time resolution are obtained. Several interesting features in the current distributions during each phase of substorm are discussed. Furthermore, a new ionospheric current model during a substorm is schematically suggested. The IMF effects on the current patterns are also discussed. For several events, the roles of the ionospheric Pedersen and Hall currents are examined separately.

By constructing the hourly distribution map of the Joule heat production rate, the particle energy injection rate and their sum over the entire polar region, it is possible to estimate the global Joule heat production rate, the global particle energy injection rate and the sum of the two quantities. It is found that the three global quantities are related almost linearly to the AE and AL indices.

ACKNOWLEDGEMENTS

I would like to express my deepest appreciation to Dr. S.-I. Akasofu, without his guidance, enthusiasm and encouragement, this thesis would have been impossible.

My gratitude also goes to the Committee Members, Drs. M.H. Rees, J.R. Kan, G.A. Gislason and L.-C. Lee, for their suggestions and criticisms. Dr. Y. Kamide, Kyoto Sangyo University, Japan, deserves special thanks for his enlightening comments and encouragement. My thanks also extend to: Dr. A.D. Richmond, NOAA, Space Environment Laboratory, for his valuable comments on computer programming; Dr. R.M. Robinson, SRI International, for providing me the Chatanika radar data and helpful suggestions; Dr. J.L. Kisabeth, for his valuable comments on the initial stage of this work; Dr. J.H. King, National Space Science Data Center, NASA, Goddard Space Flight Center, Greenbelt, Maryland, for providing me with interplanetary magnetic field data.

My work is based on mainly magnetic records from the six IMS meridian chains. I would like to thank all persons involved in the operation of the meridian chains: Dr. S.-I. Akasofu, Geophysical Institute, University of Alaska, Fairbanks, Alaska; Dr. W. Baumjohann, Max-Planck Institut für physik and Astrophysik, Garching, W. Germany; Dr. E. Friis-Christensen, Meteorological Institute, Copenhagen, Denmark; Dr. H.W. Kroehl, NOAA, Environmental Data and Information Service, NGSTDC, Boulder, Colorado; Dr. H. Maurer, Institut für Geophysik and Meteorologie, Braunschweig, W. Germany; Dr. G. Rostoker, Insitute of Earth and Planetary Physics and Department of Physics, University of

Alberta, Edmonton, Canada; J.K. Walker, Earth Physics Branch, Department of Energy, Mines and Resources, Ottawa, Canada; A.N. Zaitzev, Polar Geomagnetic Research Laboratory, IZMIRAN, Troitsk, U.S.S.R.

Thanks are due to former and present fellow students, R.K. Albano, G.D. Fry, P.C. Gray, K. Hakamada, D.U. Longenecker, R.L. Williams and W.H. Yang. Their warm friendship and continued assistances were invaluable in completing this thesis. I wish to express my indebtedness to R.M. Guritz, G. Corrick and R.P. Million for their data processing and computer programming. J.R. Burton and his crew of the drafting and photo departments are also appreciated. I owe special thanks to Ms. Shauna Sullen for the typing of this thesis.

Finally, but not least, I sincerely thank my wife, See-Mae, my son, Kee-Won, and my daughter, Sue-Yun, who put up with numerous deserted arctic winter nights due to my studying.

This research was supported under the National Science Foundation Grants, ATM81-08994 and ATM81-15321.

TABLE OF CONTENTS

LIST OF FIGURES

LIST OF TABLES

CHAPTER I INTRODUCTION

1. Historical Review of the Ionospheric Current System

Extensive studies of the large magnetic variations observed during auroral displays began in the early part of the twentieth century. It was Birkeland (1908, 1913) who first attempted to explain the magnetic variations by a three-dimensional current system (Figure I-1). He coined the term 'polar elementary storm' for such magnetic disturbances. In fact, the polar elementary substorm is one of the aspects of what are now called the polar magnetic substorm.

Since then, considerable progress has been made in inferring the substorm current system. Chapman (1935) suggested a model in which all currents responsible for the observed magnetic perturbations were confined to the ionosphere. Based on the Chapman's study on polar magnetic substorms, Silsbee and Vestine (1942) proposed an equivalent current system for polar magnetic substorms, in which a strong westward electrojet flows in the midnight and early morning sector, and a weak eastward electrojet in the early post-noon sector (Figure I-2). The next important study of polar substorms was made by Fukushima (1953). Using the actual magnetic records collected worldwide instead of hourly mean value, he showed that the equivalent current system of an isolated substorm was a single cell and any intensification of eastward electrojet tended to occur later in the substorm than the westward electrojet. Akasofu et al. (1965) proposed a new current system, in which they tried to explain the positive disturbance of the H component

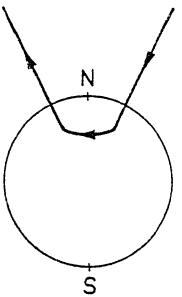

Figure I-1 Three-dimensional current system for a polar magnetic substorm proposed by Birkeland (1908).

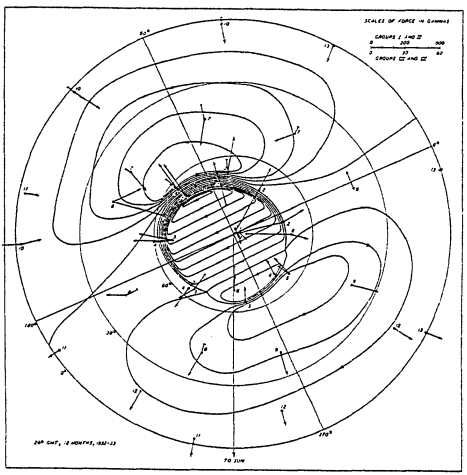

Figure I-2 Mean 3-hour disturbance vectors of magnetic bays centered at 21 hr, 24 hr and 3 hr GMT and corresponding average electric current system of height 150 km (Silsbee and Vestine, 1942).

in the afternoon and evening sectors by an eastward return current as shown in Figure I-3.

All previous current models assumed that the current systems were confined in the ionosphere. However, it became apparent that there was not enough energy source in the ionosphere to cover the energy losses of the auroral electrojets. Thus, the source must be found in the outer part of the magnetosphere and currents must flow along the geomagnetic field lines from the source region to the polar ionosphere. Boström (1964) introduced two basic types of three-dimensional current system. Figure I-4 shows his two basic current types. Subsequent observational evidences for the field-aligned currents (Zmuda et al., 1966; Zmuda et al., 1970; Armstrong and Zmuda, 1970, 1973; Iijima and Poetemra, 1976, 1978) have stimulated many workers to construct three-dimensional current systems as a representation of the substorm current system (Boström, 1968; Akasofu and Meng, 1969; Fukushima, 1969; Meng and Akasofu, 1969; Bonnevier et al., 1970; Kisabeth and Rostoker, 1971; Kamide and Fukushima, 1972; Yasuhara et al., 1975; Hughes and Rostoker, 1979; Rostoker and Hughes, 1979 and Baumjohann et al., 1981). For a comprehensive view for the recent development of current systems, see Rostoker (1972) and Kamide (1982).

During the last several years, different techniques have been developed to analyze global magnetometer data in order to infer the three-dimensional distribution of electric currents around the earth (Kisabeth, 1979; Mishin et al., 1980; Kamide et al., 1981). In the mean time, the IMS (International Magnetospheric Study) meridian chain

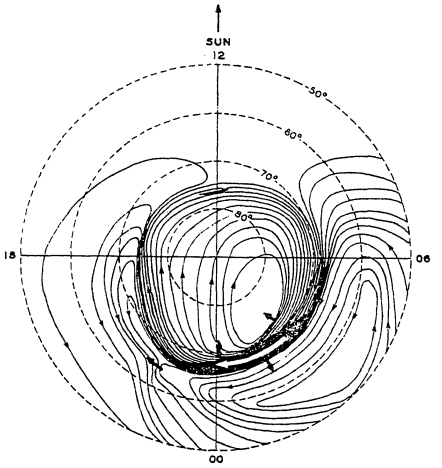

Figure I-3 Proposed model current system for an intense polar magnetic substorm; view from above dp, north pole; the direction of the sun is indicated at the maximum epoch (Akasofu et al., 1965).

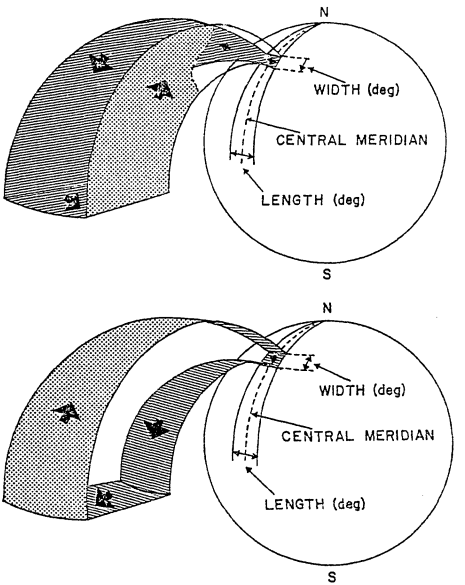

Figure I-4 Model three-dimensional E-W (top) and N-S current systems, each of finite latitudinal and longitudinal extent. These correspond to the Boström no. 1 and Boström no. 2 model, respectively (Kisabeth, 1979).

stations provided perhaps one of the most comprehensive ground magnetic data sets ever obtained for a study of geomagnetic disturbances.

In this thesis, an attempt is made to re-examine several longstanding problems of the three-dimensional currents associated with magnetospheric substorms by combining the advanced computer codes and the extensive ground magnetic data set. In particular, the ionospheric current system and the energy deposition into the polar ionosphere by means of Joule heat dissipation and auroral particle energy injection during substorms are treated as one of the main topics. For the purpose, as will be discussed in Chapter II, a new conductivity model for the polar ionosphere is introduced by analyzing the conductivity data estimated from the Chatanika incoherent radar and the magnetic disturbance data observed at College. In Chapter III, characteristics of the ionospheric currents during each phase of substorm will be presented and a model current system will be suggested. Finally, in Chapter IV the global energy deposition rate will be calculated based on the IMS meridian chain station data and empirical relations between energy deposition rates and geomagnetic indices will be given.

2. Ionospheric Current Systems of Polar Disturbances (DP)

The world geomagnetic disturbances D have at least five major components (Akasofu and Chapman, 1961; Cole, 1966; Fukushima and Kamide, 1972),

$$D = DCF + DR + DP + DT + DG$$

where DCF is the disturbance due to electric currents at the magnetopause owing to the interaction of the earth dipole field and the solar wind, DR is the disturbance due to ring current flowing in the equatorial plane of the magnetosphere, DP is the disturbance due to intense electrojets flowing in the ionosphere of the polar region (including the auroral zone) and their accompanying currents in the ionosphere or magnetosphere, or both, DT is the disturbance due to magnetospheric tail currents and DG is the disturbance due to induced ground currents.

From the morphological point of view, the geomagnetic disturbances can also be classified into several groups; (i) the solar and lunar daily variation on quiet day (S_q, L), (ii) the polar substorm and disturbance longitudinal inequality (DS), and (iii) the twin current vortices (S_q^P and others). For these topics, see the review papers by Obayashi and Nishida (1968) and Feldstein (1968). In this study, we are mainly interested in (ii) and (iii) disturbances which are considered to have magnetospheric origin and are called as DP1 and DP2, respectively.

(a) DP 1 current

The current system is responsible for the strong disturbance fields at the auroral oval latitudes in the night sector (westward electrojet) and in the evening sector (eastward electrojet). The essential feature of DP 1 is that it originates from the electrojet flowing along the auroral oval. Three types of current system proposed as the equivalent current system are shown in Figure I-5. Figure I-5a shows the classical

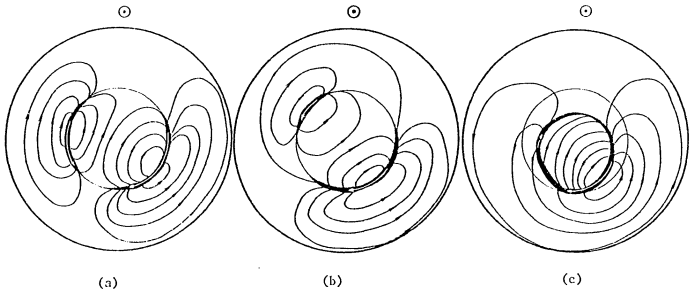

Figure I-5 Proposed equivalent current systems of DP1. (a) classical DS current system (b) and (c) are the models proposed by Fukushima (1953) and Akasofu et al. (1965), respectively.

DS current system. Figures I-5b and I-5c are the model proposed by Fukushima (1953) and Akasofu et al. (1965), respectively.

(b) DP 2 current

Nagata and Kokubun (1962) proposed a current system of magnetic field variation, S_q^p which is not associated with auroral electrojets. This daily variation was examined in detail by Kawasaki and Akasofu (1967) and Feldstein and Zaitsev (1967). The equivalent current system of the S_q^p field is shown in Figure I-6.

On the other hand, Nishida et al. (1966) proposed a distinctive type of world-wide magnetic variation, DP 2, which is not directly associated with auroral electrojet enhancement and correlated closely with the change of orientation of the IMF B_z component. The DP 2 current system is composed of two cell currents located in the morning and evening sector; the polar cap current flows from the night to the dayside. The equivalent current system of the DP2 is shown in Figure I-7. The similarity of the S_q^p and DP 2 current system suggests that they are probably of common nature and that DP 2 is due to the rapid increase of S_q^p when IMF turns southward (Feldstein, 1976).

3. Data Processing

During the International Magnetospheric Study (IMS), a joint effort was made to set up magnetometer chains along several magnetic meridians. As a result seven meridian chains were operating in 1978 and 1979: they were the Alaska chain, the Alberta chain, the Fort Churchill chain, the Greenland chain, the Scandinavia chain, the IZMIRAN chain, and the SibIZMIR chain. In addition to the projects conducted by

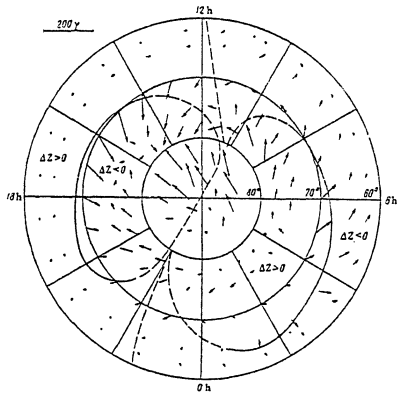

Figure I-5 Distribution of magnetic field vectors (S_q^p) at high latitudes on quiet days in summer during the IGY (Feldstein and Zaitzev, 1967).

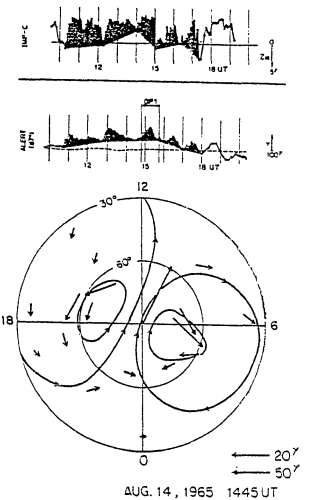

Figure I-7 Modulation of the S_q^p variations by the IMF B_z component, namely, the DP2 variation and its equivalent current system (Nishida, 1971).

individual meridian chain groups, the IMS meridian chain group has as a whole agreed to study jointly the magnetospheric substorm events. For the purpose, three consecutive days, March 17, 18 and 19, 1978, were selected, since the largest number of magnetic stations of the six meridian chains were operated. In data processing, the University of Alaska group took the responsibility of assembling, digitizing and formating the necessary data set (5-min average values).

Magnetic records from 71 stations above 50° in geomagnetic latitude were used in this study, and those stations are listed in Table I-1. For better determination of the auroral electrojet location, several subauroral region stations were included. Their distribution in eccentric dipole coordinates (Cole, 1963) is shown in Figure I-8. The geomagnetic index ΣKp on those days were 31_, 30_ and 23o, respectively.

In the following, the procedure of data processing is briefly outlined. (i) Digitization of the H and D (or X and Y) components from magnetograms from each station. Approximately 25% of all the stations used digital recorders, so that only a formating process was required for those stations. However, errors are generated during the digitization process for most of the other stations. We have attempted to minimize this problem and consider timing of all digital values to be within 2.5 minutes of their actual time. (ii) Subtraction of the base line for each station by choosing March 12, 1978 as a quiet day, (iii) transformation of the H, D (or X, Y) component into the geomagnetic north, X_m, and geomagnetic east, Y_m, components. In this

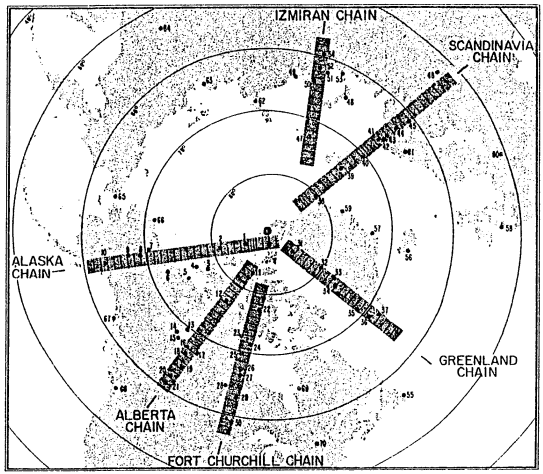

Figure I-8 Map (in eccentric dipole coordinates) of the six IMS meridian chains of magnetometer stations and of standard observatories, whose data are used in the present modeling. For identification of station name, see Table I-1 (Kamide et al., 1982a).

study, the X_m and Y_m components refer to the northward and eastward components in eccentric dipole coordinates. Thus, the data used in this study represent horizontal magnetic perturbations relative to the average magnetic field level on March 12, 1978.

Figure I-9 shows the combined X_m component traces from all the 71 stations for March 17, 18 and 19, 1978. The upper and lower envelopes provide the AU(71) and AL(71) indices, respectively, and the distance between the two envelopes gives the AE(71) index. For the details of the new geomagnetic indices, see Kamide et al. (1982a).

4. Modeling of the Three-dimensional Currents

Recently, two advanced computer codes for numerical modeling of inferring the three-dimensional current system have been developed independently by Kisabeth (1979) and Kamide et al. (1981). The two computer codes are referred to here as the K (Kisabeth) method and the KRM (Kamide, Richmond and Matsushita) method, respectively. Both algorithms take the distribution of magnetic field vectors observed on the earth's surface as the input data and provide the distribution of ionospheric currents, field-aligned currents, and other related quantities as outputs for a given set of assumptions.

They were developed on the basis of entirely different principles. Thus, if the deduced current systems were to be in reasonable agreement, it might be concluded that the non-uniqueness problem is, for practical purposes, removed. For this reason, the outcome of this test would determine the future of the modeling effort.

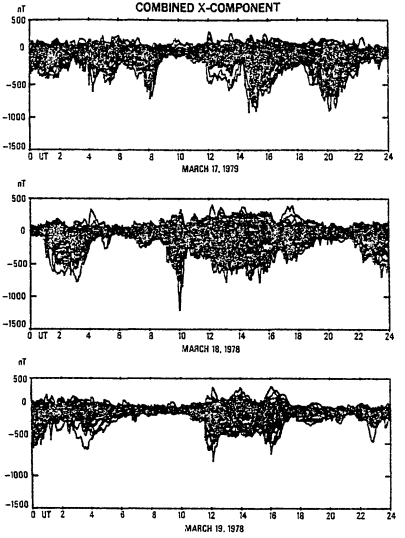

Figure I-9 The combined X_m component from 71 high-latitude stations for March 17, 18 and 19, 1978. The upper and lower envelopes give the AU(71) and AL(71) indices, respectively. The distance between the two envelopes gives AE(71) index (Kamide et al., 1982a).

Table I-1

List of the magnetic stations whose data are used in this study.

	Station Name	Geographic		Eccentric Dipole	
		Lat.	Long.	Lat.	Long.
	Alaska Chain				
0.	Eureka	80.0	274.3	89.0	325.3
1.	Isachsen	78.8	256.0	86.0	268.4
2.	Mould Bay	76.2	240.6	81.7	262.5
3.	Johnson Point	72.5	241.7	78.7	276.1
4.	Sachs Harbor	72.0	234.7	77.3	268.0
5.	Cape Parry	70.2	235.3	75.7	272.2
6.	Inuvik	68.3	226.7	72.7	264.8
7.	Arctic Village	68.1	214.4	70.5	251.6
8.	Fort Yukon	66.6	214.7	69.2	253.8
9.	College	64.7	211.9	66.9	252.9
10.	Anchorage	61.2	210.1	63.3	254.0
	Alberta Chain				
11.	Resolute Bay	74.7	265.1	83.3	311.5
12.	Cambridge Bay	69.1	255.0	77.1	301.7
13.	Yellowknife	62.5	245.5	69.6	294.1
14.	Fort Providence	61.4	242.6	68.2	291.1
15.	Hay River	60.8	244.2	67.8	293.5
16.	Fort Smith	60.0	248.0	67.4	298.9

17.	Uranium City	59.6	251.5	67.4	303.6
18.	Fort Chipewyan	58.8	248.0	66.2	299.5
19.	Fort McMurray	56.7	248.8	64.2	301.4
20	Meanook	54.6	246.7	61.9	299.6
21.	Leduc	53.3	246.6	60.6	300.0
	Fort Churchill Chain				
22.	Pelly Bay	68.5	270.5	77.4	327.4
23.	Baker Lake	64.3	264.0	72.9	318.7
24.	Rankin Inlet	62.8	267.7	71.6	324.6
25.	Eskimo Point	61.1	265.9	69.8	322.5
26.	Fort Churchill	58.8	265.9	67.5	323.0
27.	Back	57.7	265.7	66.4	322.9
28.	Thompson	55.0	263.0	63.6	320.0
29.	Island Lake	53.9	265.3	62.6	323.1
30.	Whiteshell	49.8	264.8	58.6	323.1
	Greenland Chain				
31.	Thule	77.5	290.8	85.5	22.7
32.	Upernavik	72.8	303.8	79.8	28.0
33.	Umanak	70.7	307.8	77.4	29.5
34.	Godhavn	69.3	306.5	76.2	25.5
35.	Godthab	64.2	308.3	71.2	22.5
36.	Frederikshab	62.0	310.3	68.9	23.4
37.	Narssarssuaq	61.0	314.6	67.4	28.0

	Scandinavia Chain				
38.	Nord	81.6	343.3	80.2	101.6
39.	Ny Alesund	78.9	12.0	74.8	107.3
40.	Bjornoya	74.5	19.2	70.2	104.1
41.	Skarsvag	71.1	25.8	66.3	105.1
42.	Kunes	70.4	26.5	65.6	104.9
43.	Kevo	69.8	27.0	64.9	104.8
44.	Martti	67.5	28.3	62.6	104.0
45.	Kuusamo	65.9	29.1	61.0	103.6
46.	Borok	58.0	38.3	52.2	107.2
	IZMIRAN Chain				
47.	Heiss Island	80.6	58.0	72.3	135.3
48.	Karmakuly	72.3	52.5	64.7	125.1
49.	Dixon Island	73.5	80.6	64.3	144.6
50.	Belyy Island	73.0	71.1	64.1	138.5
51.	Kharasavey	71.5	67.5	62.8	135.1
52.	Tambei	71.5	71.9	62.6	138.2
53.	Amderma	69.7	61.6	61.4	130.2
54.	Kamennyi	68.4	73.5	59.4	138.4
	Other Stations				
55.	St. John's	47.6	307.3	55.4	14.0
56.	Leirvogur	64.2	338.3	67.0	56.9
57.	Kap Tobin	70.4	338.0	72.7	64.1
58.	Hartland	51.0	355.5	52.0	65.9
59.	Danmarkshavn	76.8	341.4	77.4	81.3

60.	Niemegk	52.1	12.7	50.3	82.4
61.	Abisko	68.4	18.8	64.7	97.2
62.	Cape Chelyuskin	77.7	104.3	68.4	159.8
63.	Tixie Bay	71.6	129.0	63.1	177.9
64.	Yakutsk	62.0	129.7	53.3	181.5
65.	Cape Wellen	66.2	190.2	64.8	230.3
66.	Barrow	71.3	203.2	71.7	236.0
67.	Sitka	57.1	224.7	61.6	272.6
68.	Victoria	48.5	236.6	54.7	289.9
69.	Great Whale River	55.3	282.2	64.3	344.8
70.	Ottawa	45.5	284.5	54.6	347.1

In Figure I-10, the procedures taken by the two methods are summarized (Akasofu et al., 1981). Both methods assume that (i) geomagnetic field lines are equipotential (ii) the dynamo effects of ionospheric winds can be neglected, and (iii) the magnetic fields of the magnetospheric ring current, the magnetopause current, and the tail current can be neglected.

(a) K method

In this modeling, a spherical earth with a dipole field is considered, but it can easily be adopted for non-dipole fields. The high latitude ionosphere is divided into a large number of cells (typically ~150). Each cell is associated with two elementary three-dimensional east-west and north-south current systems. These correspond to the Boström No. 1 and Boström No. 2 model (Boström, 1964), respectively, see Figure I-4. Thus the current in each cell can be synthesized by using the two basic current systems. In the east-west current system, the current flows in the east-west direction across a cell, and it is connected to field-aligned currents at the eastern and western boundaries of the cell; also the field-aligned currents are assumed to flow along dipole field lines and to close in the equatorial plane of the magnetosphere. In the north-south current system, the current flows in the north-south direction across the cell, and it is connected to the field-aligned currents at the northern and southern boundaries; the field-aligned currents are assumed to close in the equatorial plane of the magnetosphere.

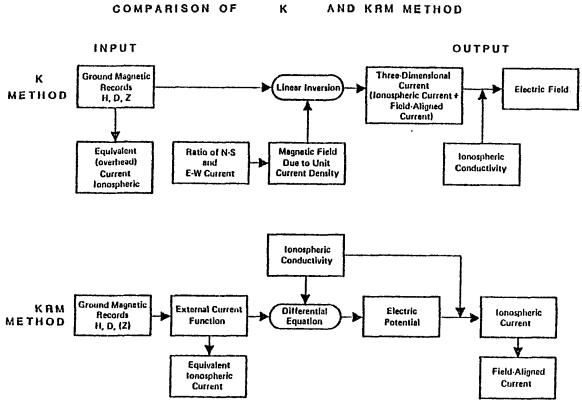

Figure I-10 Flow chart showing the comparison of the K and KRM methods (Akasofu et al., 1983).

The computer code is designed to find a set of the east-west and north-south current densities for all cells which reproduce best the input data. The procedure is to calculate first the magnetic field at all observation points due to a chosen set of unit current densities in each cell (the 'source cell'), 1 A/m for the east-west current and -0.5 A/m for the north-south current in this particular example. This choice of current densities is equivalent to utilizing a height-integrated Hall to Pedersen conductivity ratio of 2.0, provided the ionospheric electric field has only a north-south component. Once the magnetic field data (B) are calculated at all observation points due to the test current distribution (P), one can express the relation between the two quantities as a simple matrix equation,

$$B = A\,P \qquad (1)$$

where A is a huge conversion matrix. Each element of the matrix A represents the way how each component (east-west and north-south) of the current density in a source cell contributes to each component (H, D and Z) of the magnetic field at each observation point. Thus, the current distributions of the all cell (P) are calculated simply by solving the above equation with given observation data (B). Since A is not necessarily a square matrix, the following algebra is needed.

$$P = (A^T A)^{-1} A^T B \qquad (2)$$

where A^T is the transpose matrix of A.

For practical purposes, the high latitude ionosphere is divided into seven current cell rings with equal latitudinal width of 3°, extending from 61° to 82°. Note that all ionospheric currents are thus assumed to be confined in this latitude range. Each current cell ring is divided longitudinally into 24 cells, thus giving a total of 168 cells. The magnetic field is computed at 10 points along each MLT hour meridian, thus the total number of observation points is 240. In this case P, B and A matrices consist of (168 x 1), (720 x 1) and (720 x 168) elements, respectively.

(b) KRM method

The KRM method is significantly different from the K method in terms of the principles and concepts involved and requires first of all, that an ionospheric equivalent current system can be adequately derived from the ground-based data set. The equivalent current system is the toroidal horizontal sheet current $\underline{i}_T$ flowing in a shell at 110 km altitude, and the associated magnetic variation field which includes both the external (namely, primary) field and the induced field. The toroidal current can be expressed in terms of an equivalent current function ψ as

$$\underline{i}_T = \underline{n}_r \times \text{grad } \psi \qquad (3)$$

where $\underline{n}_r$ is a unit radial vector.

On the earth's surface, the magnetic variation can be expressed in terms of a magnetic potential V. Then the external portion of V is uniquely related to ψ by straightforward mathematical relations (Chapman and Bartels, p. 631, 1940). Fully automated derivations of V from instantaneous magnetic variation observations have been reported by Boström, (1971) Kamide et al. (1976b), Richmond et al. (1979) and Kroehl and Richmond (1980). The procedure is briefly outlined here (Kamide et al., 1982c).

The observed magnetic data from the 71 stations were fitted to a magnetic potential function V which is represented by a spherical harmonic series with longitudinal wave numbers, m, from 0 to 6 and order n = m to 56, as expected by the standard form:

$$V(\theta,\lambda) = \sum_{m=o}^{6} \sum_{n=m}^{56} (a_n^m \cos m\lambda + b_n^m \sin m\lambda)\, p_n^m (\cos\theta) \qquad (4)$$

where θ and λ are colatitude and east longitude (measured from midnight), respectively, in the eccentric dipole coordinate system. All terms involving associated Legendre polynomials p_n^m with even (n-m) are omitted from the series, except the term n=m, as the odd terms alone are basically sufficient to represent the northern hemispheric potential. The X_m and Y_m components at each station are expressed by

$$X_m = -\sum_m \sum_n (a_n^m \cos m\lambda + b_n^m \sin m\lambda) \frac{dp_n^m}{d\theta} \qquad (5)$$

$$Y_m = -\sum_m \sum_n m (a_n^m \sin m\lambda - b_n^m \cos m\lambda) \frac{p_n^m}{\sin\theta} \qquad (6)$$

The choice of these maximum n and m values is based on trial and error tests with a variety of values. There are in total 358 coefficients, a_n^m and b_n^m, to be determined in the harmonic series (4).

In seeking an appropriate potential function V, it is required here that the negative gradient of the potential should match up reasonably well to the observed magnetic variation vector at each station. Further the potential thus obtained should vary smoothly between stations. The principle adopted by Richmond et al. (1979) to determine the coefficients is the minimization of the following function Ψ with respect to variations of the coefficients a_n^m and b_n^m:

$$\Psi(V) = \sum_j \left\{ \left[X_m^j - \frac{\partial V(\theta^j,\lambda^j)}{\partial\theta} \right]^2 + \left[Y_m^j + \frac{1}{\sin\theta} \frac{\partial V(\theta^j,\lambda^j)}{\partial\lambda} \right]^2 \right\}$$
$$+ \frac{\Gamma}{2\pi} \int_0^{\pi/2} \sin\theta d\theta \int_0^{2\pi} d\lambda \left\{ \frac{1}{\sin\theta} \frac{\partial}{\partial\theta} \left[\sin\theta \frac{\partial V}{\partial\theta} \right] + \frac{1}{\sin^2\theta} \frac{\partial^2 V}{\partial\lambda^2} \right\}^2$$
$$+ \frac{\gamma}{2\pi} \int_0^{2\pi} d\lambda \left[\frac{\partial^2 V(\pi/2,\lambda)}{\partial\lambda^2} \right]^2 \qquad (7)$$

where X_m^j and Y_m^j are the observed geomagnetic north and east perturbations at the j th stations; Γ and γ are pre-chosen weighting factors. It is found that the results obtained from this algorithm could be improved by making several ad hoc modifications to the

smoothing constraints, primarily by increasing the smoothing in longitude with respect to smoothing in latitude. This permitted a reduction in the maximum m value and an increase in the maximum n value without increasing the total number of coefficients. The root-mean-square difference between computed and observed magnetic perturbations is typically 15%. However, at certain times the discrepancy rises above 20%.

It is then assumed that there is a relatively small internal contribution to the magnetic potential caused by a perfectly conducting layer 300 km below the earth's surface. The remaining external potential $V^{(e)}$ is extrapolated to 110 km altitude and converted to an equivalent ionospheric current function ψ by the standard procedure:

$$\psi_n = \frac{1}{\mu_o} \frac{2n+1}{n+1} \left(\frac{a}{R_E} \right)^n V_n^{(e)} \qquad (8)$$

where

$$\psi = \sum_n \psi_n (\theta, \lambda)$$

$$a = R_E + 110 \text{ km}$$

$$\mu_o = 4\pi \times 10^{-7} \text{ H/m}$$

With a given equivalent current function ψ and a given conductivity model which will be discussed in the next chapter, the ionospheric currents, electric field and field-aligned currents can be obtained under the assumption that geomagnetic field lines are radial. Thus the KRM method is not suitable in studying the low latitude field, but is unlikely to substantially affect high latitude results.

The total height-integrated ionospheric current is considered to consist of two parts.

$$\underline{J} = \underline{J}_T + \underline{J}_p \tag{9}$$

the toroidal (solenoidal) current $\underline{J}_T$ is related to a current function ψ, which can be expressed in terms of a magnetic potential V, which in turn can be obtained from the meridian magnetic data. The other part, the poloidal current $\underline{J}_p$ can be considered as a closing current for field-aligned currents $j_\parallel$: Note that $j_\parallel = \text{div } \underline{J}_p$ and $\text{div } \underline{J}_T = 0$ by definition, and that $j_\parallel$ and $\underline{J}_p$ together produce no ground magnetic variation under the assumption of magnetic field lines penetrating vertically into the horizontal ionosphere; field-aligned currents are assumed to flow perpendicular to a horizontal ionosphere.

The total horizontal ionospheric current is related to the electric field $\underline{E}$ by Ohm's law:

$$\underline{J} = \Sigma_P \underline{E} + \Sigma_H \underline{E} \times \underline{n}_r \tag{10}$$

where Σ_P and Σ_H are the height-integrated Pedersen and Hall conductivities and $\underline{n_r}$ is a unit radial vector. The electric field is derivable from an electrostatic potential ϕ as

$$\underline{E} = -\text{grad } \phi \tag{11}$$

A partial differential equation for ϕ in terms of ψ can be obtained by equating the two different expressions of $\underline{J}$ and taking the curl of the resulting equation. In spherical coordinates θ (colatitude) and λ (east longitude), these results

$$A\frac{\partial^2\phi}{\partial\theta^2} + B\frac{\partial\phi}{\partial\theta} + C\frac{\partial^2\phi}{\partial\lambda^2} + D\frac{\partial\phi}{\partial\lambda} = F \tag{12}$$

where the coefficients are given by

$$A = \sin\theta\ \Sigma_H$$

$$B = \frac{\partial}{\partial\theta}(\sin\theta\ \Sigma_H) + \frac{\partial}{\partial\lambda}\Sigma_P$$

$$C = \Sigma_H/\sin\theta$$

$$D = -\frac{\partial}{\partial\theta}\Sigma_P + \frac{\partial}{\partial\lambda}\frac{\Sigma_H}{\sin\theta}$$

$$F = \frac{\partial}{\partial\theta}\sin\theta\frac{\partial\psi}{\partial\theta} + \frac{1}{\sin\theta}\frac{\partial^2\psi}{\partial\lambda^2}$$

In solving the above equation, we use the following boundary conditions on $\phi(\theta,\lambda)$:

$$\phi(0,\lambda) = 0, \tag{13}$$

$$\frac{\partial\phi}{\partial\theta}\left(\frac{\pi}{2},\ \lambda\right) = 0. \tag{14}$$

The boundary condition at the equator is of little significance to the solution of ϕ in the high latitude regions of interest to us. It is used for numerical convenience.

The equation (12) is solved numerically by a finite-difference scheme over a network of points spaced 1° in latitude and 15° in longitude. Once the electrostatic potential is obtained, we derive the electric field from (11), the ionospheric current from (10), and the field-aligned current by taking divergence of the ionospheric current.

(c) Comparison of the results obtained by the two methods

It has long been feared by a number of workers that owing to the non-uniqueness problem, entirely different current patterns may result from the same input data set for different methods, and thus that such a modeling effect is not very worthwhile. However, Akasofu et al. (1981) showed that with an appropriate data set, the two independent codes have been developed to the point that the non-uniqueness of the solution is no longer a serious problem, at least as far as the large-scale pattern of ionospheric currents is concerned. In spite of the total different principles and the conductivity models used in the computations, the two

methods provide similar large-scale patterns of the ionospheric and field-aligned currents in high latitudes. In addition, the estimated values are in fair agreement with those observed more directly by recent radar and satellite techniques.

Figure I-11 shows the distribution of ionospheric currents by using the K method on the left and that obtained by the KRM method on the right. The input data were 5-min average values at every MLT hour for the three invariant magnetic field components obtained from the IMS Alaska meridian chain of observatories for the period between March 9 and April 27, 1978. Figure II-5(a) shows the input data. For details of the input data, see Akasofu et al. (1980a). One can see that the large-scale patterns are quite similar, in spite of the fact that the conductivity models by both methods are considerably different. Figure I-12 shows the distributions of field-aligned currents for the two models. Again, both methods resulted in similar distributions of the region 1 and region 2 field-aligned currents (Iijima and Potemra, 1976), although details are significantly different.

Figure I-13 shows the electric field distribution obtained by the two methods. In the K method, the electric field is not one of the outputs. However, as shown in Figure I-10, one can infer the electric field distribution by using the calculated ionospheric current and by assuming the ionospheric conductivity. Note that in this model, the ratio of the east-west and north-south current densities is assumed as 2:1 everywhere (Akasofu et al., 1980a). This assumption seems reasonable in view of some recent observations that the ionospheric

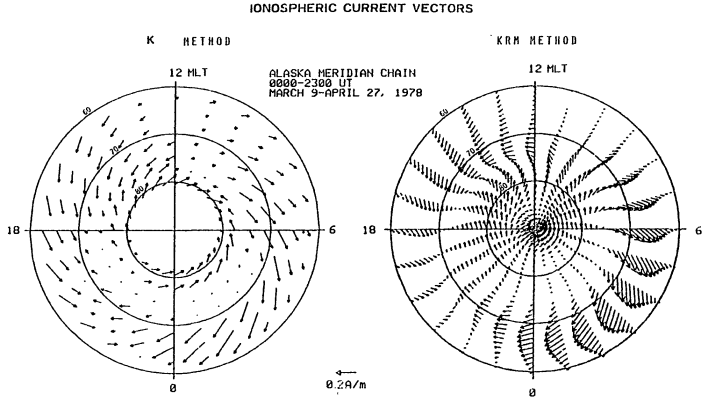

Figure 1-11 Comparison for the calculated ionospheric current vectors between the K and KRM methods (Akasofu et al., 1983).

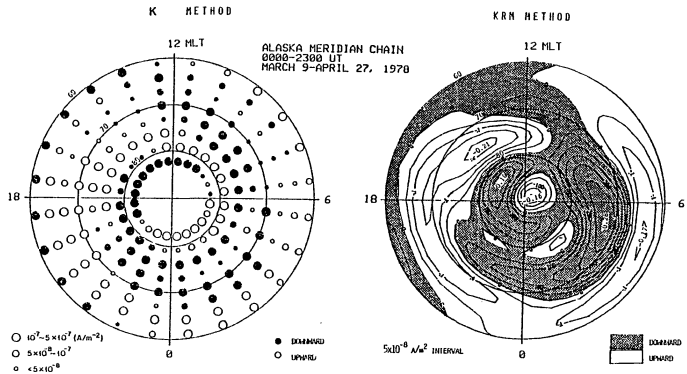

Figure I-12 Comparison for the estimated field-aligned current between the K and KRM methods (Akasofu et al., 1983).

Figure I-

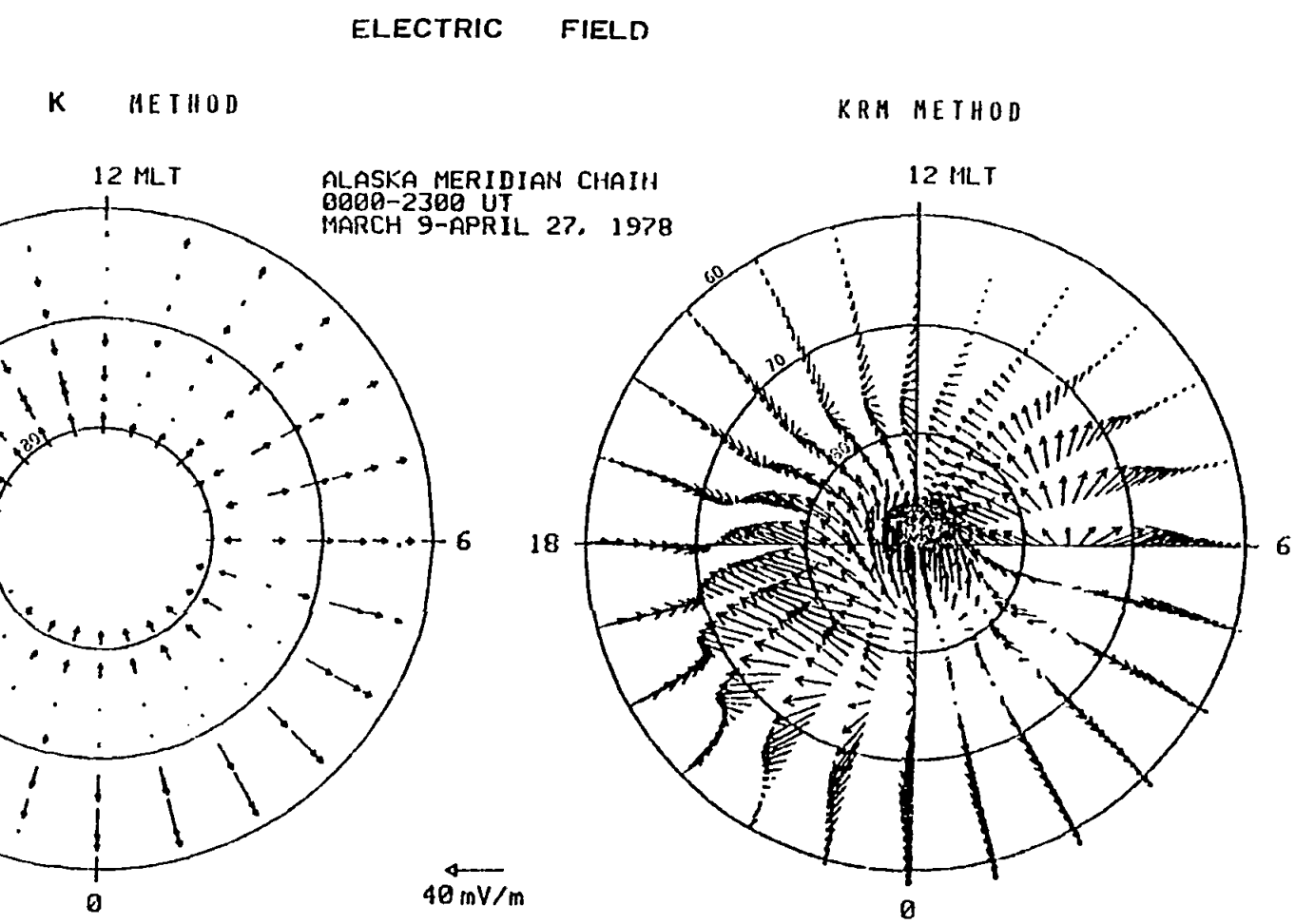

13 Comparison for the estimated electric field vectors between the K and KRM methods (Akasofu et al., 1981).

electric field has mainly the north-south component in auroral latitudes (e.g., Heppner, 1977) and the Hall to Pedersen conductivity ratio is typically 2 (Brekke et al., 1974). During the different degrees of magnetic activity, different conductivity ratios were used (Akasofu and Ahn, 1981). However, the assumption of a uniform value of this ratio for the entire ionosphere provides a strong restriction to the results in the K method. Although such an assumption can be removed for a large memory size computer, the current ratio should not be given a priori as an input but must be solved as an output such that the electric field, the conductivity, the ionospheric current, the field-aligned currents and ground magnetic perturbations are all consistent. In generating the electric field distribution of the K method in Figure I-13, it is simply assumed the uniform conductivity within the belt between the 61° and 84° latitudes; the conductivities, Σ_P = 5 mhos and Σ_H = 10 mhos. In the KRM method, however, the electric field can be obtained as one of the outputs by assuming a conductivity model. Further, the method can deal with a variety of conductivity. The conductivity model used in producing the electric field of the KRM method in Figure I-13 is shown in Figure II-5(b). For detail comparisons of the above two methods, see Akasofu et al. (1981), Kamide (1982) and Akasofu et al. (1983).

As mentioned above, the KRM method is more convenient to deal with realistic conductivity models than the K method. Further, the electric field distribution, which is quite sensitive to the choice of conductivity model, is one of the outputs. Due to such a practical point of view, the KRM method is adopted in this study.

CHAPTER II A CONDUCTIVITY MODEL FOR THE POLAR IONOSPHERE

1. Introduction

In modeling ionospheric current systems on the basis of magnetic or electric field observations, by either ground-based or satellite-borne instruments, accurate knowledge of the conductivity of the polar ionosphere is essential; for a recent review paper on this subject, see Greenwald (1982). One solution to this problem is to have a large number of either ground-based or satellite-borne ionospheric sounders and/or incoherent scatter radars. However, such a solution cannot be realized at this time. The lack of accurate conductivity models has recently become acute as powerful computer codes have been developed to model instantaneous distributions of ionospheric and field-aligned currents, with a time resolution of ~ 5 minutes or less, on the basis of simultaneous magnetic records from a very large number of magnetic observatories, (e.g., Kamide et al., 1982a). Thus, a fully compatible distribution of the conductivity over the polar region is required to make this particular magnetic study accurate.

Kamide and Matsushita (1979 a,b) assumed a Gaussian type distribution of the form,

$$\Sigma(\theta,\lambda) = \Sigma(\max) \exp\left[-\frac{(\theta-\theta_o)^2}{D_\theta^2} - \frac{(\lambda-\lambda_o)^2}{D_\lambda^2}\right]$$

where (θ_o,λ_o) gives the center location of the enhanced conductivity region at which $\Sigma(\theta,\lambda)$ is maximum, namely $\Sigma(\max)$. The two constants D_θ

and D_λ specify the Gaussian distribution for latitudinal and longitudinal directions, respectively. Recently, Wallis and Budzinski (1981) and Spiro et al. (1982) have developed advanced conductivity models which depend statistically on geomagnetic activity indices. Such models are certainly better than any conductivity models in the past. However, since one now has to deal with complex current patterns over the entire polar region at particular instants with a high time resolution, it is not possible to specify all characteristics of a given substorm and thus of the conductivity distribution by a single parameter, such as the AE or Kp index; at two instants with the same value of the AE index, the current patterns may be significantly different. Likewise, at two instants with the same value of the AE index, the auroral distribution and the conductivity distribution may be significantly different.

Thus, this new progress in determining three-dimensional current systems demands conductivity models which can reflect conditions on an instantenous basis. However, since the number of ionospheric sounders in the polar region is very limited, one must find a method to estimate the global conductivity distribution with presently available data. As a first step toward such a goal, it is of great interest to examine whether or not the magnitude of magnetic disturbances, one of the most readily available quantities, is related in any simple, but quantitative way to various ionospheric quantities we are interested in.

It is examined in this thesis how the magnitude of magnetic disturbances is related empirically to the local ionospheric conductivities

and electric fields although the latter is not used in constructing conductivity models. Specifically, examined are possible relationships of the magnitude of the horizontal component magnetic disturbances with the height-integrated Pedersen and Hall conductivities. The ionospheric quantities are deduced on the basis of measurements by the Chatanika radar facility. The magnitude of the simultaneous horizontal component magnetic field variations is determined using magnetic records from College, the closest standard magnetic observatory to Chatanika. For this purpose, both published radar data (Baron, 1972; Brekke et al., 1974; Baron and Chang, 1975; Banks and Doupnik, 1975; Wedde et al., 1977; Doupnik et al., 1977; Rino et al., 1977; Brekke and Rino, 1978) as well as unpublished data are used.

2. Data Analysis

Since most of the Chatanika radar data are averaged in time and space, we take the time resolution of our data to be 30 minutes. Thus, 30-minute averages of the College magnetic field perturbations, more specifically, the north-south component (ΔH) data are used. The average values thus determined are averaged over the period of individual positive and negative 'bay' events; in this way events lasting less than 30 minutes are eliminated. Such a procedure can emphasize large bay events (which is interested in this study) and tend to suppress long-lasting weak disturbances. The main difference between such "event" plots and "individual point" plots is that the latter has a large cluster of points around $\Delta H \sim 0$.

The empirical relationships of the north-south magnetic component (ΔH) with the height-integrated Hall (Σ_H) and Pedersen (Σ_P) conductivities, their ratios (Σ_H/Σ_P) and the north-south component of the electric field (E_{NS}) are obtained separately for positive ($\Delta H > 0$) and negative ($\Delta H < 0$) events. These empirical relationships with ΔH are shown in Figure II-1, II-2, II-3 and II-4 and also are listed in Table II-1. In the plots which show the relationship of ΔH with Σ_H, Σ_P, etc., the events are weighted in terms of the product of their duration and the magnitude ΔH, and the relative importance thus determined is indicated by the size of circles. The product is proportional to the radius of the corresponding circle. In this way one can distinguish large, and long-lasting events, from spike-like events.

Unfortunately, it is very hard to make reliable error estimates, since the data used in this chapter came from various sources. However, a rough error estimation for each quantity is made and shown in Table II-1.

(a) Conductivities

Before determining the relationship of ΔH with the conductivity values obtained by the Chatanika radar, the solar EUV contribution is subtracted from the height-integrated conductivities by employing the empirical relation between the solar zenith angle and the conductivities obtained by Mehta (1979). After making this correction, the relationships of the height-integrated Hall and Pedersen conductivities with the magnitude of the corresponding ΔH component of magnetic disturbances

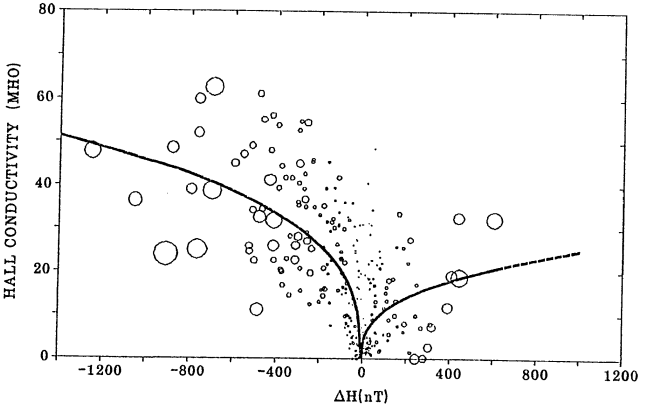

Figure II-1 The relationship between the height-integrated Hall conductivity measured from the Chatanika radar and the north-south component (ΔH) of the magnetic field disturbance observed at College. The radius of each circle represents the weight of each event. The solid curves are best fit curves.

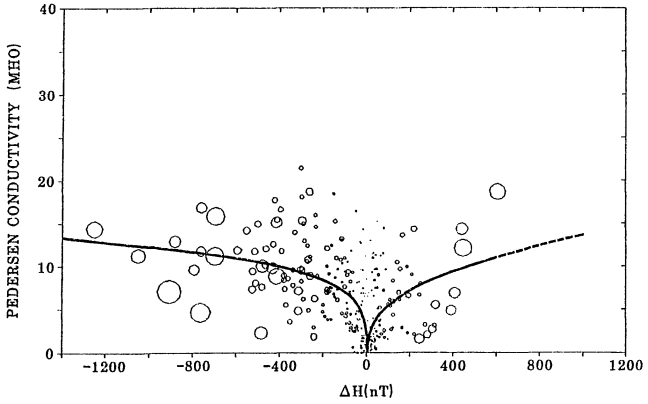

Figure II-2 Same as Figure II-1 for the relationship between the height-integrated Pedersen conductivity and ΔH.

TABLE II-1

The empirical relations between ΔH and several ionospheric quantities. The units of the north-south component of magnetic disturbance (ΔH), the north-south component of electric field (E_{NS}), the height-integrated conductivities (Σ_H, Σ_P) and the auroral particle energy injection rate (u_A) are nT, mV/m, mho and mwatt/m^2, respectively. Except the conductivity ratio (Σ_H/Σ_P), the empirical relations are expressed for positive ($\Delta H > 0$) and negative events ($\Delta H < 0$), separately. The error estimate corresponds to one standard deviation. The quantity u_A is expressed also in two different ways, since Σ_H is expressed in terms of ΔH.

	$\Delta H < 0$	$\Delta H > 0$
Σ_P	$2.43(\Delta H)^{0.24} \pm 6.7$	$0.70(\Delta H)^{0.43} \pm 6.2$
Σ_H	$4.36(\Delta H)^{0.34} \pm 9.8$	$2.10(\Delta H)^{0.36} \pm 7.6$
E_{NS}	$-1.31(\Delta H)^{0.48} \pm 11.0$	$5.09(\Delta H)^{0.35} \pm 14.6$
Σ_H/Σ_P	$2.8 - \tanh\left(\frac{\Delta H + 50}{200}\right) \pm 0.7$	
u_A	$0.011(\Sigma_H)^{1.99}$	
	$0.20\ (\Delta H)^{0.68}$	$0.05\ (\Delta H)^{0.71}$

are shown in Figure II-1 and Figure II-2, respectively. In spite of a considerable scatter of the points, it can be seen that both Σ_H and Σ_P tend to increase systematically as $|\Delta H|$ increases. Table II-1 lists the least-square expression of the relationship between Σ_H and ΔH and also between Σ_P and ΔH. The enhancement of Σ_H is much more clearly seen during negative bay events than during positive bay events. For positive ΔH portions, it is not easy to express the relation of Σ_H for positive bays by a simple expression. It is assumed, however, that the expressions for $\Delta H>0$ and $\Delta H<0$ have similar forms, hence, the obtained expression is only a tentative one. Note also that the growth rates of both Σ_H and Σ_P become less for large values of $|\Delta H|$. Such a trend was also reported by Vanyan and Osipova (1976).

In Figure II-3, is shown the relation between the conductivity ratio Σ_H/Σ_P and ΔH. It is striking that there is a difference in the response of this ratio to positive and negative ΔH values. During negative bays, the ratio increases with ΔH, but the rate of the increase decreases for large values of ΔH and tends to approach an asymptotic value of about 3.8. In contrast the ratio approaches an asymptotic value of about 1.8 during positive bay events. Table II-1 lists the empirical relationship between Σ_H/Σ_P and ΔH.

(b) Electric Field

Since electric field data are also available from the Chatanika radar, the relationship between the north-south component of the electric field E_{NS} and ΔH is examined. The results are shown in Figure II-4. The best fit curve shown there is listed in Table II-1. From

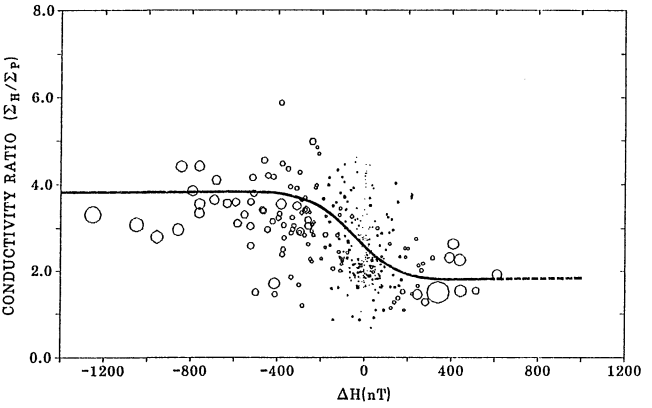

Figure II-3 Same as Figure II-1 for the relationship between the conductivity ratio (Σ_H/Σ_P) and ΔH.

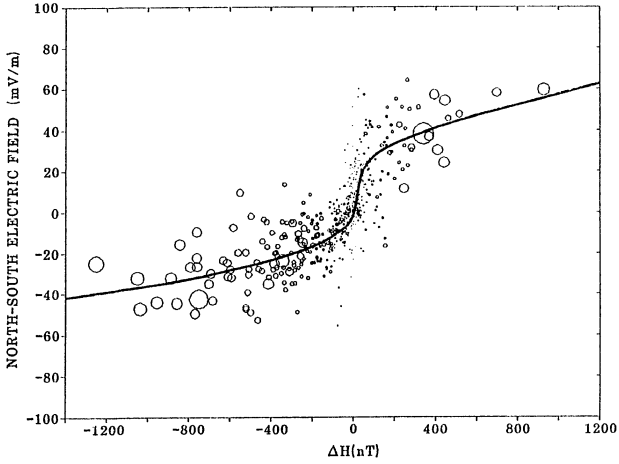

Figure II-4 Same as Figure II-1 for the relationship between the north-south component of the electric field measured from the Chatanika radar and ΔH.

Figure II-4 one can see several interesting trends between the two quantities. As is well known, the direction of the electric field is mostly northward during positive bay events and southward during negative bay events. As magnetic activity increases, the electric field is enhanced, and the enhancement is more prominent during positive bay events than during negative bay events.

The east-west component of the electric field is also examined in the same way. However, due to its highly variable nature and small magnitude, it is difficult to derive a meaningful empirical relation with ΔH, although the eastward component is mostly associated with positive bay events and the westward component mostly with negative bay events.

3. Conductivity Models for the Polar Ionosphere

As the first step in constructing a global conductivity model, the observed magnetic field perturbation distribution is expressed by a magnetic potential function represented by a spherical harmonic series, see Chapter I. Figure II-6a is an example of input data corresponding to the maximum epoch of an intense substorm. From this series, one can recalculate ΔH on regularly spaced grid points; the grid size can be adjusted. Once ΔH variations are determined at each grid point, it is possible to estimate Σ_H and Σ_P values over the entire polar region by applying the empirical formulae obtained in the previous section.

However, it is important to emphasize that the empirical formulae listed in Table II-1 are derived from the radar and the ground magnetic observations at auroral latitudes alone. In particular, ΔH variations

in the polar cap region are known to be caused mainly by sources other than overhead ionospheric currents (e.g., Heppner et al., 1971). It is also unreasonable to assume that the ΔH variations in the subauroral zone are due to overhead ionospheric currents. Thus, the empirical relations obtained in the previous section cannot be applied directly to the polar cap ionosphere and the subauroral zone. Fortunately, however, conductivity estimates based on satellite measurements of precipitating particles have now become available (Wallis and Budzinski, 1981; Spiro et al., 1982), although there is no 'direct' estimate of the conductivity in the polar cap region except for several rocket measurements (cf., Vanyan and Osipova, 1976). These studies show that the height-integrated conductivities Σ_H and Σ_P in the polar cap region seldom exceeds several mhos. Because of this low variability of the conductivity in the polar cap ionosphere, it may be possible to construct a reasonable global conductivity model with fair accuracy by introducing a reasonable reduction factor for the value of Σ_H and Σ_P in the polar cap and the subauroral zone.

Thus the next step is to find such a reduction factor in both inside (the polar cap) and outside the oval. We consider a weighting function which is proportional to the latitudinal distance from the latitude at which $|\Delta H|$ or $\Sigma_H(\Sigma_P)$ maximizes. By scanning the calculated conductivity value along each MLT meridian, we can find the latitudes at which ΔH and thus Σ_P and Σ_H have a local maximum. If there is only one maximum of the conductivity within the average auroral oval (determined by Feldstein) along a particular meridian $\lambda = \lambda_i$, the weighting function

the meridian is defined by

$$R(\theta,\lambda_i) = \exp\left[-\left(\frac{\theta_{LM}-\theta}{D_{\lambda_i}}\right)^2\right]$$

where θ_{LM} is the colatitude of local maximum, and D_{λ_i} is a constant proportional to the local maximum value of Σ_H. Note that the larger the magnitude of Σ_H, the wider the shape of the Gaussian weighting function, as implied by Feldstein's ovals for different Q values.

Finally, the conductivity value at a grid point Σ' is determined simply by multiplying the calculated value, Σ from the empirical formula in Table II-1 by the weighting function, R defined above, $\Sigma' = \Sigma \cdot R$.

Generally, the local maximum in each MLT sector is found within the average auroral oval determined by Feldstein, but sometimes several local maxima could be found along a single MLT meridian, some even outside the average oval. In order to reduce confusion arising from such a situation, we adopt the "auroral region" which is defined as follows: Consider first the belt is bounded by the poleward boundary of the quiet time Feldstein oval (Q=0) and the equatorward boundary of the disturbed time oval (Q=7) (Feldstein and Starkov, 1967; Whalen, 1978). Determine the north-south width ℓ of the oval in each MLT meridian and extend the poleward boundary poleward by $\ell/4$ and the equatorward boundary equatorward by $\ell/4$. We consider only the maxima which occur within this "auroral region". When a maximum is found in either inside (polar cap) or outside of it, it is ignored, although such an occurrence is rather rare. If more than two are found, only the two largest

significant peaks are selected. Then each peak has its own weighting function, say R_1 and R_2 for the peaks located at the colatitudes θ_1 and θ_2, respectively ($\theta_2 > \theta_1$). Thus, one needs to choose a weighting function either R_1 or R_2 for every grid point along the meridian. Let θ_o be the colatitude which is located between two peaks and satisfying the condition $R_1(\theta_o,\lambda) = R_2(\theta_o,\lambda)$. Then the weighting function to be chosen at a grid of colatitude θ is given by

$$R(\theta,\lambda) = \begin{cases} R_1(\theta,\lambda) \; ; & \theta < \theta_o \\ R_2(\theta,\lambda) \; ; & \theta > \theta_o \end{cases}$$

Unfortunately, the above procedure tends to make the conductivity values in the polar cap and the nightside subauroral zone too low. Since there are various sources of ionization in the E region of the ionosphere other than the solar EUV and auroral particle bombardment (such as the ring current particle precipitation, the polar rain, etc.), we add an extra contribution to each of the grid points over the entire polar region. Finally, the solar EUV contribution is added to the auroral enhanced conductivity distribution calculated by the above procedure. Due to the extra source of enhancement, the final values are increased as much as 1.0 mho for Σ_H and 0.5 mho for Σ_P over the entire polar region. For the background conductivity, the model originally developed by Tarpley (1970) and improved by Richmond et al. (1976) is employed, since it allows one to estimate the conductiviy below the latitude of the auroral zone, as well as the entire polar region.

At the present time, some arbitrariness in the above procedure is inevitable, although we have made some independent examinations by obtaining the total potential drop across the polar cap for a large number of cases (using the KRM method developed by Kamide et al., 1981) and by comparing them statistically with the observed values; the total potential drop is quite sensitive to the conductivity values in the polar cap and the subauroral zone.

It is believed that in spite of the arbitrariness, the steps taken in the procedure described above indicates one of the ways to effectively utilize the presently available data.

Further, the steps can be improved. For example the new Greenland incoherent scatter radar data will considerably improve the weighting function. Therefore, it is hoped that this study points one of the directions, we should take in the future in studying the geomagnetic disturbance field.

In the following, the empirical formulae for Σ_H and Σ_P are applied to two data sets of ground magnetic perturbations to demonstrate their ability in estimating the global distribution of electric fields and currents.

(a) The average Alaska meridian chain data

Using the average Alaska meridian chain data obtained by Akasofu et al. (1980a) as the input data (Figure II-5a), the present model is compared with the Gaussian distribution model which has been devised by Kamide and Matsushita (1979a,b), and been extensively used by Kamide and Akasofu (1981) and Akasofu et al. (1981). The Gaussian model is shown

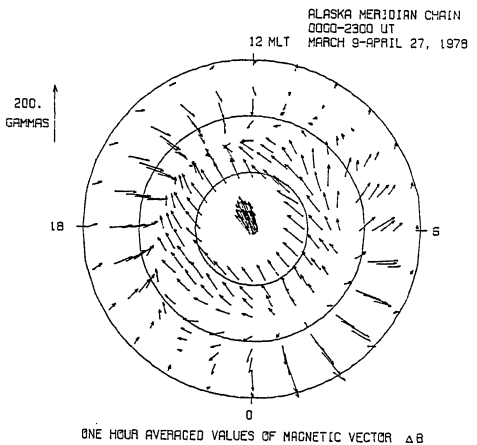

Figure II-5(a) The average magnetic daily variation vectors obtained from the IMS Alaska meridian chain of magnetic observatories (Akasofu et al., 1980). This is the input data used in generating the conductivity distributions in Figures II-5(b), (c) and (d).

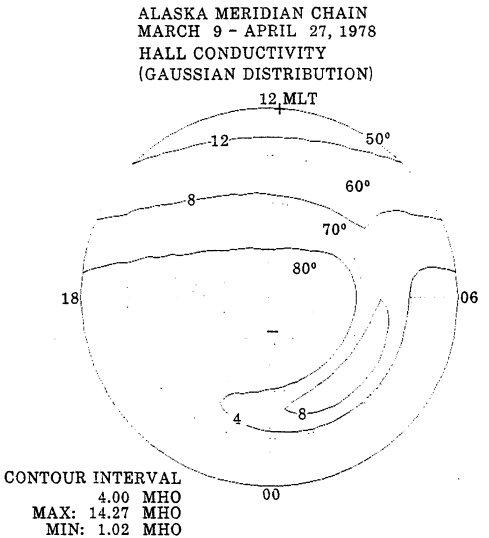

Figure II-5(b) Isocontours of the Hall conductivity distribution based on the Gaussian distribution model. The Pedersen conductivity distribution of this model has basically the same pattern as the Hall conductivity except the magnitude of the nightside auroral enhanced zone is reduced to about half of the value of the Hall conductivity (Akasofu et al., 1983).

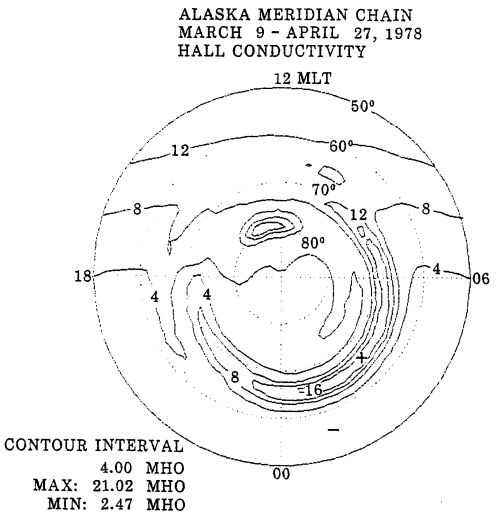

Figure II-5(c) The Hall conductivity distribution based on our study.

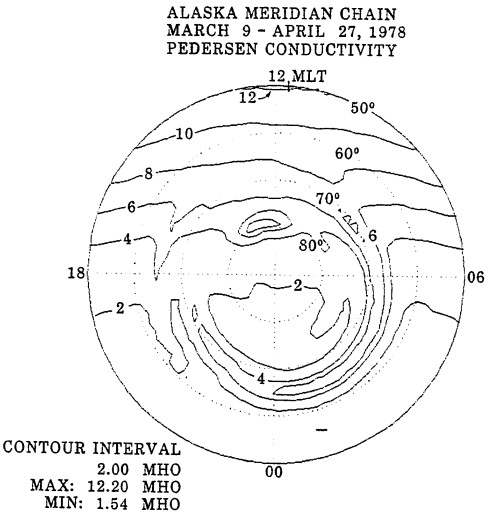

Figure II-5(d) Same as Figure II-5(c) for the Pedersen conductivity distribution.

in Figure II-5b. The distributions of Σ_H and Σ_P (determined in the way described in the previous section) are shown in Figures II-5c and II-5d, respectively. One can see that the two models show generally a similar enhanced belt at auroral latitudes in the morning sector, but the maximum value of Σ_H in the present model is much higher than that in the Gaussian model. The longitudinal extent of the enhanced zone is also greater in the present model than in the Gaussian model. There are several more enhanced regions in the present model which are absent in the Gaussian mode. They are the enhancements of the dayside cusp region, the eastward electrojet region in the evening sector of the auroral zone and a similar enhanced region at latitudes ~76° in the morning sector.

(b) 1200 UT on March 19, 1978

Since the goal of this chapter is to be able to construct a conductivity model at particular instants on the basis of the distribution of ΔH over the entire polar region, we examine here the conductivity distribution at 1200 UT on March 19, 1978. The magnetic field distribution at that moment was obtained from the six IMS meridian chain stations (Kamide et al., 1982a), see Section 3 in Chapter I. This epoch was during the maximum phase of a substorm and the AU(71) and AL(71) indices at this moment were 175 nT and -583 nT, respectively. Figure II-6a shows the global distribution of the magnetic field disturbance vectors at 1200 UT. Figures II-6b and II-6c show the Hall and Pedersen conductivity distributions estimated from the empirical formulae obtained in the previous section. In Figures II-6d and II-6e,

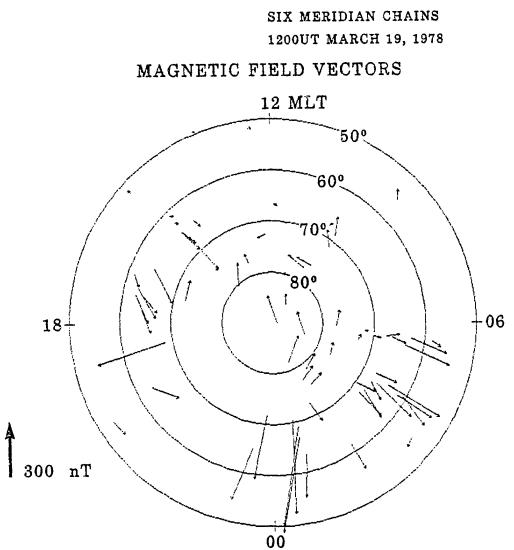

Figure II-6(a) The magnetic perturbation vectors observed from six IMS meridian chain stations at 1200 UT on March 19, 1978. This is the input data used in generating the conductivity distributions in Figures II-6(b), (c), (d) and (e).

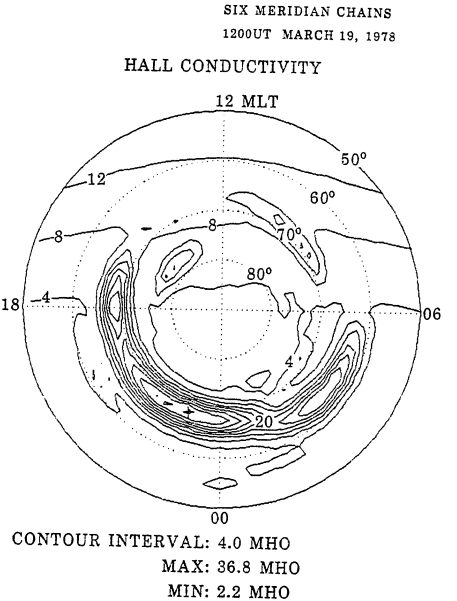

Figure II-6(b) Isocontours of the Hall conductivity distribution based on our model.

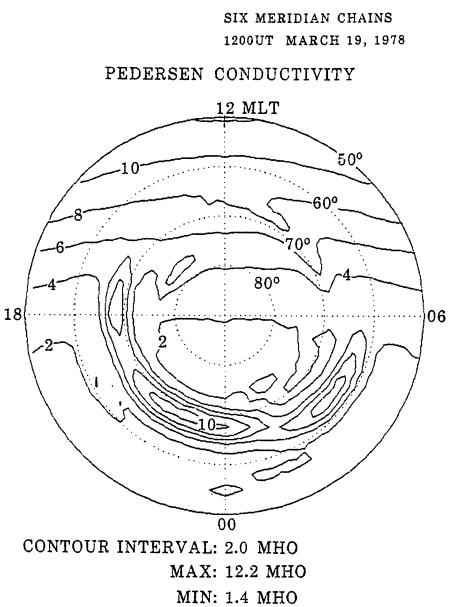

Figure II-6(c) Same as Figure II-6(b) for the Pedersen conductivity distribution.

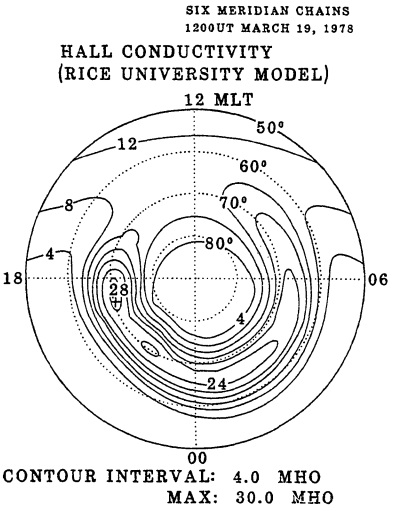

Figure II-6(d) Isocontours of the Hall conductivity distribution based on the model by Spiro et al. (1982).

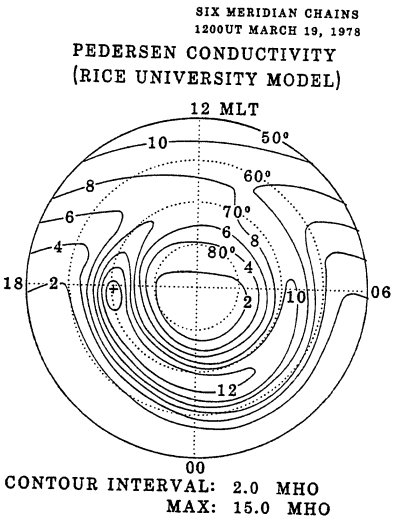

Figure II-6(e) Same as Figure II-6(d) for the Pedersen conductivity distribution.

we show Σ_H and Σ_P distributions based on the model developed by Spiro et al. (1982) for AE = 758 nT. One can see here again that the general features of the primary enhanced zone in both models agree reasonably well. However, there are several interesting differences to be noted between the two models. The magnitude and location of the maximum enhanced region are significantly different. In the model by Spiro et al. (1982), the maximum region appears at colatitude $\theta = 19°$, $\lambda = 1900$ MLT and the magnitude is about 30 mhos for Hall and 15 mhos for Pedersen conductivities. However, in the present model the maximum region appears at a little lower latitude than theirs, $\theta = 22^o$, $\lambda = 23$ MLT, and the magnitude is 37 mhos for Hall conductivity and 12 mhos for the Pedersen conductivity. The conductivity ratio Σ_H/Σ_P, at the maximum enhanced region is about 2 in the model by Spiro et al. (1982) and about 3.2 in the present model. We believe that from Figure II-3 the ratio in the Spiro et al. (1982) model seems too low. As in the previous example, one can see that there are enhancements in the dayside cusp region in the present model. This may partly be due to the fact that their particle data had the cut-off energy at 0.2 keV and that the minor enhancement was eliminated by their statistical treatment.

4. An Empirical Relation Between Height-integrated Hall Conductivity and Auroral Particle Energy Injection Rate

Recently, Wickwar et al. (1975) showed that the electron density profile measured by the Chatanika radar can be used to obtain the energy input rate due to precipitating particles. It was also pointed out that most of the contribution for the height-integrated rate of energy input

comes from near the peak of the ionization profile, which is usually between 90 and 130 km. If one takes into account the tendency that the height-integrated Hall conductivity emphasizes the electron density in the region below 125 km (Brekke et al., 1974), it is reasonable to expect that there exists an empirical relation between Σ_H and the auroral particle energy injection rate u_A. A high correlation between Σ_H and u_A can be seen in Figure II-7, which is taken from Murdin and Brekke (1980), but is slightly modified by taking 30-min averages of their original data. The units of u_A and Σ_H are in mwatt/m^2 and mho, respectively. Other good examples can also be found in Banks (1977).

Using the measurements by Murdin and Brekke (1980) and Banks (1977), a scatter diagram between Σ_H and u_A is constructed and is shown in Figure II-8. The best fit curve is listed in Table II-1, where the units of u_A and Σ_H are in mwatt/m^2 and mho, respectively. Note that this fit gives the same Hall conductivity-energy flux relation expected from a source of electrons with a Maxwellian velocity distribution of average energy 4 keV.

Since the empirical relation between Σ_H and ΔH has been established, it may be possible to rewrite the above expression as a function of ΔH. In this case the empirical relation will be two, depending on the sign of ΔH. The empirical formula used is included in Table II-1.

Figure II-9 shows an example of the global particle energy injection rate based on data at 1200 UT on March 19, 1978. One can see that the region where the energy injection rate is greater than 2

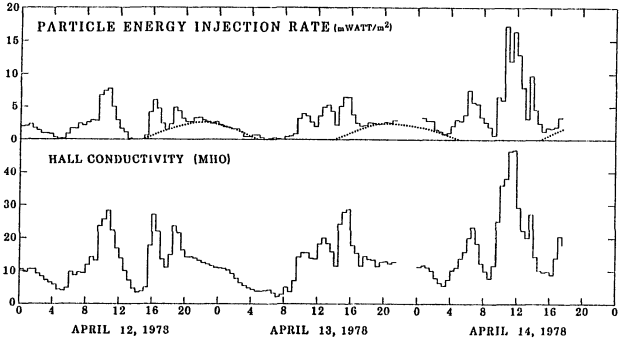

Figure II-7 The upper and lower panels show the particle energy injection rate and the height-integrated Hall conductivity both estimated from the Chatanika radar (Murdin and Brekke, 1980). The data are slightly modified by taking 30 minutes average. The dotted lines in the upper panel represent the solar EUV contribution. We used only the night-time data in this analysis.

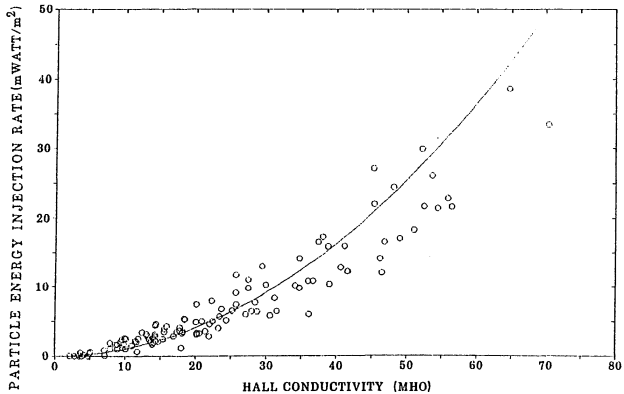

Figure II-8 The relationship between the particle energy injection rate and the Hall conductivity. The solid curve is the best fit curve between the two quantities. Each circle represents 30 min averaged event.

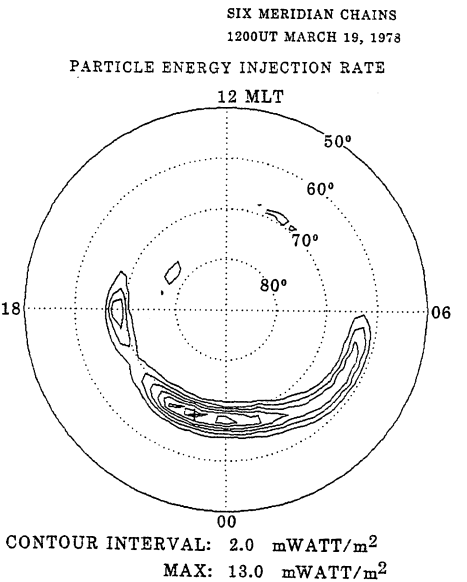

Figure II-9 Isocontours of the global particle energy injection rate at 1200 UT on March 19, 1978.

mwatt/m^2 coincides roughly with the nightside auroral oval. The maximum energy input rate is 13.0 mwatt/m^2 and is found around the magnetic midnight. The total particle energy injection rate integrated from the pole down to 50° in latitude is 0.38 x 10^{18} ergs/sec in this particular example.

CHAPTER III. GLOBAL IONOSPHERIC CURRENT DISTRIBUTIONS DURING SUBSTORMS

1. Introduction

Since the pioneering works of Birkeland and Chapman for the study of the ionospheric current using ground-based magnetic field data, enormous efforts have been made during the last half a century in understanding the magnetospheric substorm processes in terms of the growth and decay of the three-dimensional current system. However, it has long been known that it is not possible to determine uniquely the current system only on the basis of the distribution of the ground magnetic field data. In spite of such a fundamental difficulty, considerable progress has been made both in observational and theoretical studies.

During the last several years, a number of advanced computer codes for numerical modeling of inferring the three-dimensional current system have been developed by Kisabeth (1979), Mishin et al. (1980) and Kamide et al. (1981) based on entirely different principles. Moreover, comparing the algorithms of Kisabeth (1979) and Kamide et al. (1981) by using a common data set, Akasofu et al. (1981) concluded that the non-uniqueness problem is, for practical purpose, removed.

In the mean time, the IMS chain stations have provided invaluable ground magnetic field data and the individual chain group has contributed considerably in understanding the ionospheric current system. However, the data from one or two meridian chain observatories are not

enough to determine the instantaneous pattern of the global ionospheric current distribution. Moreover, it is hard to obtain the time sequential picture of the global current system associated with magnetospheric substorms by records from one or two chains of observatories. It is for these reasons that a joint effort was made to set up magnetic observatories along several magnetic meridians during the IMS. As a result, six meridian chains of observatories were operated in 1978. For the detailed description of the data set used in this study, see Kamide et al. (1982a) or UAG Report 87 (Kamide et al., 1982c).

As a result of such an effort, Kamide et al. (1982) obtained, for the first time, the three-dimensional current system over the entire polar region on an instantaneous basis by using the IMS chain station data and a computer code developed by Kamide et al. (1981). They also showed that the gross features of the instantaneous distributions of the ionospheric and field-aligned currents are remarkably similar to the daily average pattern during a very weak activity and at different substorm epochs and that the large scale current pattern grows and decays systematically as a whole.

The purpose of this chapter is to examine the growth and decay of a number of substorms in terms of the total ionospheric currents over the entire polar region by using the same procedure adopted by Kamide et al. (1982a). Since the data set is the most comprehensive one ever obtained, it is an ideal opportunity to re-examine the longstanding uncertainties in the current distribution during magnetospheric substorms. Particularly we are going to show the time-sequential

picture of the ionospheric current distribution over the entire polar region during magnetospheric substorms. In addition, the control of the interplanetary magnetic field (IMF) on the ionospheric current pattern is also examined. The conductivity model used in this study was developed recently by Ahn et al. (1982) and is explained in Chapter II. As shown by Kamide and Richmond (1982) the choice of conductivity model would not affect significantly the ionospheric current distribution.

2. Results

By using the current patterns and auroral activities, it is attempted to clarify the following points.

(i) Are there any characteristic patterns in the dayside high latitude region during each phase of a substorm? If so, is there any dependence of such patterns on the AE index, the IMF and the auroral electrojet activity in the night side auroral zone?

(ii) Is there any unique quiet time current system?

(iii) Many believe that an initial slow growth prior to a rapid growth is a growth phase signature. Then what are the true characteristics of the slow and weak growth phase? Or is it simply the same, but weak substorm? Is there any tendency that the first substorm after a quiet period is a weak one?

(iv) Are there periods during which the current system is identical or very similar to the substorm current system prior to substorm onset?

(v) How can one characterize the development of intense substorm current systems?

(vi) How is the recovery phase of an intense substorm current system characterized?

(vii) What are the characteristics of the current pattern in the high latitude zone above 80°? Are there any systematic changes in the current pattern during different phases and different intensities of substorms?

(viii) How accurate are AE(12) or AE(71) in describing substorm activity?

(a) The ionospheric current distribution

In this section, we will examine the total current distribution patterns of 48 instants which include various phases and different degrees of substorm intensity. Here, the total ionospheric current is defined simply as the sum of the Pedersen and Hall components of the ionospheric current. Although the distribution patterns of various ionospheric quantities are highly variable and have often localized variations during a substorm, it is possible to monitor changes of the global distribution pattern by the IMS meridian chains.

Figure III-1 shows the AU and AL indices of March 17, 1978 which were constructed by the records from 71 stations. The difference between the two indices gives the AE index. Fortunately, the IMF data

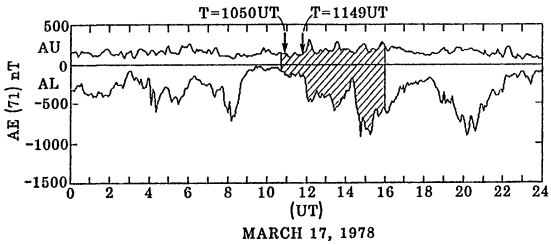

Figure III-1 The AU(71) and AL(71) indices of March 17, 1978, the shaded region indicates the time period examined in this study. The substorm onset times determined by the auroral photographs are also shown.

were available during March 18 and 19. Thus, Figure III-2 includes the IMF data together with the AU and AL indices for the two days. The shaded portions in Figures III-1 and III-2 are the time intervals examined in this chapter. The time T shown in the figures represent approximate onset times of substorms which are determined by using all-sky photographs and riometer records from the Alaska meridian chain stations.

Figures III-3 shows the total ionospheric current distributions at 1040, 1100, 1200, 1400, 1500, and 1700 UT on March 17. They are chosen to show the distributions during a disturbed condition. In terms of the AE index, the substorm had a slow growth which was subsequently followed by a rapid growth. Such a slow growth has been identified by a number of workers as a signature of growth phase. For the determination of the exact time of the expansion phase, however, it is important to examine the corresponding all-sky camera data. Fortunately, the Alaska meridian chain was more or less located in the magnetic midnight sector at the time. Although it was slightly overcast over College, the pictures in Figure III-4 shows clearly that there was an auroral breakup at about 1050-1051 UT on March 17. Thus, the current distribution at 1040 UT may be considered to represent an example of the pre-expansion phase. The most prominent feature of the distribution is the strong dayside current flows, which consist basically of a westward current in the high latitude zone and an eastward current along the southern edge of the former. Although it is not prominent, there is a weak westward electrojet in the morning sector. On the other hand, the strong

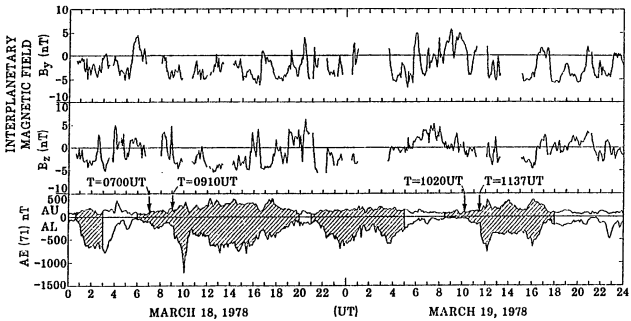

Figure III-2 The lower panel is the same as Figure III-1 for March 18 and 19, 1978. The upper and middle panels show the IMF B_y and B_z components of the two days, respectively.

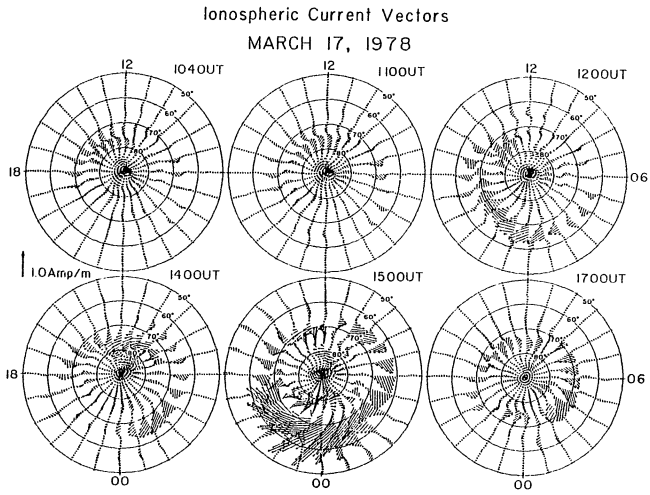

Figure III-3 The distributions of calculated ionospheric current vectors at 1040, 1100, 1200, 1400, 1500 and 1700 UT on March 17, 1978.

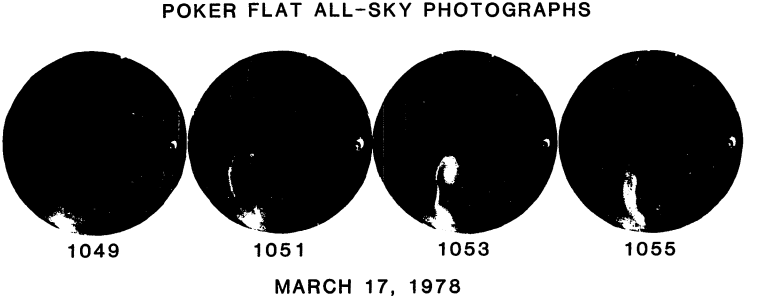

Figure III-4 The all-sky photographs of aurora taken at Poker Flat.

eastward current originated from the dayside is almost terminated at about 1900 MLT sector. It is also interesting to note that the current intensity in the auroral zone of the midnight and late evening sectors is extremely weak.

The epoch 1100 UT on March 17 was during the expansion phase of a weak substorm. One can see that the strong currents flowing in the dayside cusp region were still the dominant feature. However, the westward electrojet in the night sector was enhanced further (compared with that at 1040 UT) and seemed to be connected spatially with the westward current in the dayside cusp region. In the pre-midnight sector, a noticeable eastward electrojet emerged. Moreover, there is an indication that the westward electrojet contacted with the eastward electrojet at about 2000 MLT sector and a portion of the eastward electrojet joined with the westward electrojet flowing north of it. A close examination of the current distribution reveals that there is a weak eastward electrojet flowing south of the westward electrojet at about 1000 MLT sector. The current distribution in the polar cap did not show any systematic pattern. The AE index at the moment was 229 nT. In spite of such a low magnetic activity in terms of the AE index, it is interesting to note that the overall current system at 1100 UT basically consists of two noticeable auroral electrojets.

Another auroral breakup was observed over College at about 1150 UT. Simultaneously the College riometer recorded the onset of absorption. Further, the AE index increased abruptly from 348 nT to 630 nT just before 1200 UT. Thus, the current pattern at 1200 UT in

Figure III-3 may well serve as an example of the current pattern during the expansion phase. The distribution is generally enhanced compared to that at 1100 UT. In particular, the westward electrojet in the evening and midnight sectors is enhanced prominently and is extended deeply into the dusk sector. On the other hand, the portion of the westward electrojet in the late morning sector did not show any noticable enhancement. In contrast to the westward electrojet, the eastward electrojet in the evening sector shows fairly uniform enhancement. The strong current flows in the dayside cusp region seemed to shift toward the postnoon sector and also decayed slightly. The eastward electrojet in the late morning sector around 1000 MLT meridian seemed to move toward the dayside and enhanced slightly.

It is interesting to examine the changes of current pattern between at 1100 UT and 1200 UT, since both times coincided more or less with an early epoch of the expansion phase. One can see that there are several noticeable differences between the two current patterns. First, the portion of westward electrojet from the early morning to dusk sectors through the midnight sector was enhanced prominently in the current distribution at 1200 UT. A sharp increase of the AE index seemed due to this enhancement. On the other hand, the enhancement of the eastward electrojet in the afternoon and evening sectors was much less than that of the westward electrojet. Second, the locations of the auroral electrojets at 1200 UT showed noticeable shift. In particular, the portion of the eastward electrojet in the dusk sector shifted equatorward about 3° further compared to that at 1100 UT. Third, the

well developed current pattern in the dayside cusp region at 1100 UT waned considerably at 1200 UT. Fourth, there was a rapid deflection of ionospheric current direction in the polar cap, particularly above 80° in latitude in the pre-midnight sector. Such a deflection was reported as one of signatures characterizing the transition period from the growth phase to the expansion phase (Iijima and Nagata, 1972; Iijima, 1972; Kokubun and Iijima, 1972). The exact definitions of the growth phase and the pre-expansion phase will be discussed later.

Since the recovery phase seemed to start before 1400 UT, the ionsopheric current pattern at 1400 UT can be used as an example of the current pattern during the recovery phase of a substorm. The center of the westward electrojet moved toward 0300 MLT sector. Such a shift of the center of the westward electrojet during the recovery phase was reported by Kamide (1982). Comparing the locations of the auroral electrojets at 1400 UT with those at 1200 UT, one can see that the eastward electrojet in the dusk sector shifted slightly poleward, but no appreciable shift was found in the westward electrojet in the morning sector. Another interesting feature at 1400 UT in Figure III-3 is that there is a strong eastward current in the dayside cusp region. Such a current pattern was reported by Friis-Christensen et al. (1982), who found that a positive value of the IMF B_y component is responsible for the growth of such a current system. The topic will be discussed further later. Further, the eastward current seemed to originate from the midnight sector along the northern edge of the westward electrojet.

The College riometer showed again the onset of a very intense absorption at about 1427 UT. Simultaneously the AE index in Figure III-1 shows also a very sharp increase. At about 1500 UT, the substorm reached its maximum phase and gradually subsided, see Figure III-1. Comparing the pattern at 1500 UT with that at 1200 UT, one can see several interesting differences. First, the intensity and width of the westward electrojet seems to be proportional to the magnetic activity expressed in terms of the AE index. However, this feature is barely noticeable for the eastward electrojet. Second, the locations of both the westward and eastward electrojets in the evening and morning sectors shifted noticeably equatorward. Third, as far as the current distribution above 80° in latitude is concerned, there seems no major change in the pattern and intensity. Fourth, it is not clear whether there is an eastward electrojet along the southern border of the westward electrojet in the noon or morning sector. At 1700 UT, one can notice that the center of the westward electrojet moved toward the morning sector as the substorm subsided. Simultaneously both auroral electrojets, particularly the westward electrojet shifted rapidly poleward. On the other hand, there is an indication that the direction of the current flow in the polar cap seemed more or less to align sunward.

It is particularly interesting to compare the distribution patterns at 1400 UT and 1700 UT in Figure III-3, since the two instants were both dur ng the recovery phase of different substorms and the AE(71) index was the same, namely 525 nT and 525 nT, respectively. First of all, one

can notice that the westward electrojet at 1400 UT was located at about 6° lower in latitude than that at 1700 UT. In other words, in spite of its recovery phase the westward electrojet did not shift much poleward in the former event. Thus, when the magnetic activities of the two events are expressed in the standard AE(12) index, the latter event should have smaller value than that of the former, since the standard AE stations are located well below the auroral electrojets in the latter event. Actually AE(12) indices of the two events were 365 nT and 296 nT (Kamei and Maeda, 1981). As pointed out by Kamide et al. (1982a), Akasofu et al. (1983) and Kamide and Akasofu (1983), it is quite clear that the standard AE(12) index could not monitor the auroral electrojets accurately, particularly when the magnetic activity is below 250 nT in terms of AE(12) index. Second, the directions of current flows in the dayside cusp region in the two epochs were almost opposite. At 1400 UT, there was a strong eastward current flow, whereas there was a westward current flow at 1700 UT. This will be discussed further later. Third, there was a hint of an eastward electrojet along the southern edge of the westward electrojet in the morning sector at 1700 UT, but there was no signature of such a current flow at 1400 UT.

Although it is not shown here, the current distribution in the nightside sector at 1800 UT decayed considerably, while that in the dayside sector did not show any noticeable change. Thus, the current distribution of the dayside high latitude zone seems to be affected less by substorm activity than that of the night sector. Such a tendency can be seen also in the current distribution at 1040 UT.

Figure III-5 shows the six current distribution patterns during the substorm which seemed to begin at about 0100 UT on March 18. Due to the lack of the relevant data, however, it was not possible to determine accurately the onset time. At 0040 UT, weak current flows are noticeable only in the dayside cusp region, the polar cap region and the dawn sector of the auroral zone. The subsequent current distribution at 0050 UT shows the enhanced current flows in the dayside cusp region and a relatively well developed westward electrojet along the entire morning sector auroral zone. In spite of the strong eastward current in the dayside cusp region, there is no definite indication of an eastward electrojet in the auroral zone, except for a weak segment of it at about 65° in latitude in the evening sector. However, the current distribution in the polar cap region did not show any noticeable change either in pattern or intensity. It is interesting to note that the current pattern in the dayside cusp region is quite similar to that at 1400 UT on March 17 in Figure III-3. Further, one can notice that both epochs have another similarity in the current distribution of the polar cap region. Note the clockwise current vortex in the midnight sector of the polar cap in both epochs.

The current distribution at 0100 UT is quite similar to that at 0050 UT, except that there is a strong westward current in the prenoon quadrant. It is an unusual feature. Moreover, it appeared suddenly after 0055 UT. The auroral electrojets were slightly enhanced compared to those at the previous epoch. However, the eastward electrojet is barely noticeable. At about 0105 UT, the westward electrojet in the

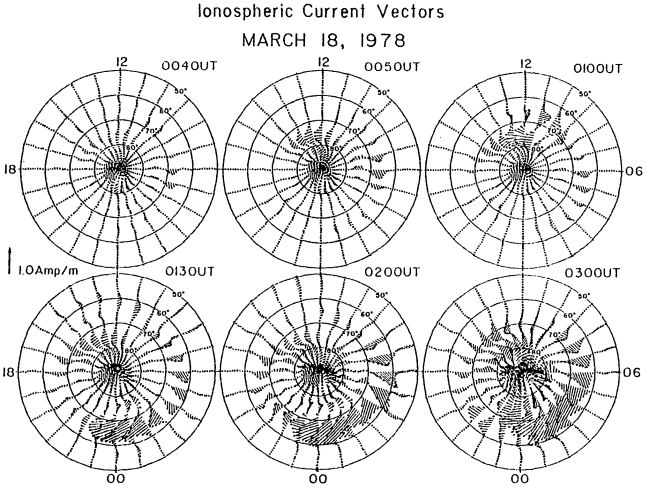

Figure III-5 Same as Figure III-3 for at 0040, 0050, 0100, 0130, 0200 and 0300 UT on March 18, 1978.

midnight sector was suddenly enhanced. Since then, the strong current flows in the dayside high latitude region wane gradually and the intensity of the auroral electrojets increase as the substorm intensifies. At 0130 UT, one can see a well-developed auroral electrojet system. Note the highly enhanced portion of the westward electrojet in the midnight sector.

As can be seen in the current distribution at 0200 UT, the auroral electrojets were enhanced further, while the current intensity in the dayside sector was slightly reduced. On the other hand, there occurred a prominent widening of the belt and a slight equatorward shift of the auroral electrojet belt particularly in the dawn and dusk sectors. In spite of the changes in the current pattern during the epochs mentioned above, no significant change was found in the polar cap region, although there was only a weak enhancement of the current intensity.

At 0300 UT, there was an indication of the recovery phase. For example, the center of the westward electrojet moved from the midnight to the early morning sector. Several other changes deserve mentioning. First, the current intensity in the dayside cusp region was enhanced prominently. Further the pattern was also changed. Second, the weak eastward current flowing along the poleward boundary of the westward electrojet in the midnight and early morning sectors at 0200 UT changed its direction almost completely and was enhanced prominently at 0300 UT. Third, the enhancement of the current intensity in the polar cap was also unusual.

Figure III-6 shows the ionospheric current distributions during a weak disturbance between 0550 UT and 0820 UT. It is particularly interesting to examine the change of the current pattern during such a period, since the pattern thus obtained can be compared with that of an intense disturbance. In order to decide the phase of the substorm, the auroral photographs taken at Fort Yukon (69.2°, in eccentric dipole coordinate) and Sachs Harbor (77.3°, in eccentric dipole coordinate) were used. Although they are not shown here, a faint arc appeared over the northern horizon of Fort Yukon at about 0704 UT. Then it brightened at 0706 UT. Subsequently, a westward traveling surge was seen over the northern horizon at about 0731 UT and left the field of view at about 0746 UT. On the other hand, there was a faint arc over the southeastern horizon of Sachs Harbor at about 0716 UT. Then the arc brightened at about 0718 UT. Since then a very strong auroral activity was observed between 0735 UT and 0802 UT. In spite of such data, it is still hard to decide the exact time of the expansion phase, since the stations were not in the midnight sector at the time. However, it seemed reasonable to assume that the expansion phase started at about 0700 UT. Thus, the current distribution at 0630 UT in Figure III-6 may be identified as an example of the pre-expansion phase.

It is also worthwhile to examine whether there is any significant changes in the current pattern during the pre-expansion phase. For the purpose, the current distributions between at 0530 and 0630 UT on March 18 were examined. The magnetic activity during that period was fairly uniform and low in terms of the AE index; see Figure III-2. The average

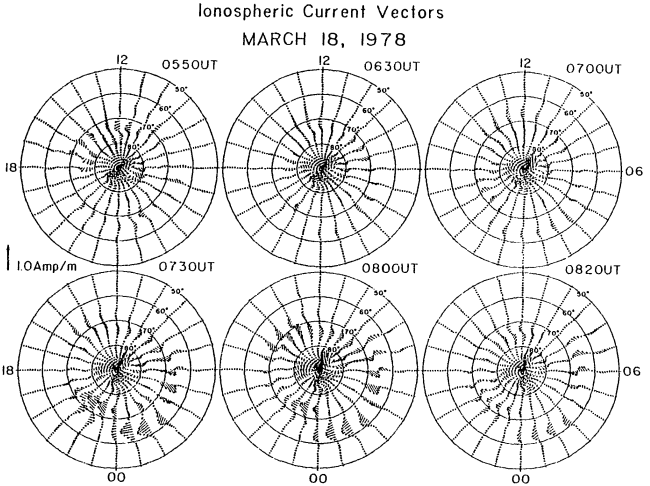

Figure III-6 Same as Figure III-3 for at 0550, 0630, 0700, 0730, 0800 and 0820 UT on March 18, 1978.

AE index was about 125 nT during the period. As a typical example of the current pattern during such a period, the current pattern at 0550 UT, is selected and shown in Figure III-6. Several interesting features deserve noting. First, there is a noticeable eastward electrojet almost in the entire morning sector, except the early morning sector. It is an unexpected feature. Although it is not shown here, such a current pattern was quite prominent from about 0535 UT and persisted until about 0600 UT. On the other hand, it would be also interesting to examine the sign change of the IMF B_z component during the period. Since there is a slight delay of the ionospheric response to the IMF change, the current pattern at 0550 UT seemed to be related to the northward turning of the IMF at about 0515 UT. It will be discussed further later. Second, the current pattern of the afternoon sector shows a strong spatial variation. Third, it is worth mentioning that the current pattern in the polar cap region above 80° in latitude basically consisted of two current vortices. Similar patterns were found in the polar cap region of the previous examples. Although the current patterns at intermediate epochs are not shown in Figure III-6, the current pattern at 0550 UT evolved gradually into that of 0630 UT. The transition started first in the nightside auroral zone. The overall current density of the region was gradually reduced. At about 0610 UT, the eastward electrojet in the midnight and early morning auroral zones was replaced by a weak westward electrojet. However, the current pattern in the sunlit hemisphere and the polar cap region particularly above 70° in latitude did not show any noticeable change except a slight

reduction in intensity. As a next step, the eastward electrojet in the late evening auroral zone was gradually enhanced. Simultaneously the weak westward electrojet in the midnight and early morning sectors was also enhanced and intruded deeply into the evening sector along the northern edge of the eastward electrojet in the pre-midnight quadrant. At about 0620 UT, the current pattern was quite similar to that at 0630 UT, except that there was still a noticeable eastward electrojet in the prenoon quadrant about 65° in latitude. However, there was no appreciable change in the current pattern of both the sunlit and nightside hemispheres above 80° in latitude. Although there was no sudden change in the current distribution during the period, one can notice that the substorm type current distribution which basically consists of two auroral electrojets emerges gradually in the nightside auroral zone, before the expansion phase which was determined by the auroral breakup. Such a gradual change of current pattern will be shown again in Figure III-10.

It was assumed tentatively above that the expansion phase of the weak substorm started after 0630 UT. However, it seemed more reasonable to assume that the time of the expansion phase was at about 0700 UT, since the auroral activities were observed from the Alaska meridian chain stations only after 0700 UT. Further, there was a sudden increase of the AE index from 181 nT to 258 nT within 5 minutes just after 0655 UT. If the expansion phase of the substorm started at about 0700 UT, it is clear that the substorm activity started before it in terms of current distribution. Thus, it would be appropriate to introduce a

phase prior to the expansion phase. Let us call this phase tentatively as 'development phase'. In this particular example, the phase seemed to start at about 0610 UT and lasted before the start of the expansion phase. However, the AE index did not show any noticeable increase during the 'development phase'. Thus, one would not be able to determine the 'development phase' on the basis of the AE index.

The current distribution at 0630 UT in Figure III-6 is an example of a 'development phase'. One can see that there is a well developed westward electrojet, which extended from the prenoon to premidnight sectors through the morning sector. In spite of some ambiguities in the late afternoon sector, it is also clear that there is an eastward electrojet in the dusk sector. If one recalls that there is a large data gap in the late afternoon sector which corresponds to the Arctic Ocean and eastern Siberia, however, such ambiguities can be partially understood.

It is of great interest to see whether there is any signature of the twin-vortex current pattern, or the DP 2 current (c.f. Chapter 1) which was originally proposed by Nishida (1968) on the basis of the equivalent current distribution. It has long been thought to be the signature characterizing the current pattern during the growth phase (Iijima and Nagata, 1970 and 1971; Kokubun, 1971; Kokubun and Iijima, 1972; Pudovkin and Troshichev, 1972; Nishida and Kamide, 1982). However, such a signature could not be found in the ionospheric current distribution during the interval between 0530 UT and 0630 UT. Here our 'development phase' corresponds roughly to the growth phase in terms of

only the time sequential point of view, and has an entirely different current patterns. Further, it may not be possible to identify by the AE index.

Let us compare the current distributions at 0630 UT on March 18 in Figure III-6, with that at 1100 UT on March 17 in Figure III-3. The two epochs are approximately in their 'development' and expansion phases, respectively. The gross features are quite similar as far as the night side auroral zone is concerned. It is also important to note that the westward electrojet in both epochs were located more or less at about the same latitude. Strictly speaking the westward electrojet at 0630 UT, particularly in the dawn sector, is located at a slightly higher latitude than that at 1100 UT. To understand such a difference, a comparison of the AE index for the two epochs may be partially helpful. They were 264 nT and 168 nT at 1100 UT and 0630 UT, respectively. However, significant differences are found in the dayside cusp and polar cap regions. Particularly, it is hard to find any similarity between the current distributions at the two epochs in the polar cap region. Further, let us compare the current distribution at 0630 UT with that at 0700 UT in Figure III-6. The two epochs seem to be the 'development' and expansion phases, respectively. Here again, no significant change was found in the basic current distribution of the nightside auroral zone. However, the westward current in the dayside cusp region at 0630 UT shifted noticeably equatorward, while the current pattern in the polar cap did not show any change during the period. From the above comparisons, it seems that there is no distinct differ-

ence between the 'development' and expansion phases as far as the ionospheric current distribution in the nightside auroral zone is concerned. The main difference is manifested in the intensification of the current and a slight equatorward shift during the expansion phase.

At about 0730 UT on March 18, the disturbance seemed to reach its maximum phase in terms of the AE index. The current distribution at the moment in Figure III-6 shows enhanced auroral electrojets compared to those at 0630 UT. The enhancement of the westward electrojet is much more prominent than that of the eastward electrojet. Further, note the strong enhancement of the current intnesity in the midnight sector compared to that in the dayside sector. The westward electrojet seems to be connected with the westward current in the dayside cusp region and they formed an elongated oval. The current distribution at 0800 UT shows some indications of the recovery phase. Several changes are noticeable compared to the previous epoch. The current intensity in the midnight sector is reduced. However, the eastward electrojet in the dusk sector seems to be enhanced slightly. The current intensity in the postnoon sector was also enhanced. There is also a clear indication of the eastward electrojet along the southern edge of the westward electrojet in the morning sector. As can be seen in Figure III-2, the disturbance subsided and was weakest at about 0820 UT in terms of the AE index. The current pattern at 0820 UT is basically the same as that at 0800 UT, except that the overall current intensity is reduced slightly.

It is interesting to see whether there is any difference between the current distributions at 1700 UT in Figure III-3 and at 0820 UT in Figure III-6, since both epochs were more or less at the end of the recovery phase. A significant difference can be found in the location of the auroral electrojets. The auroral electrojets at the former epoch were shifted toward the polar cap region compared to those of its maximum phase at about 1500 UT in the same figure, while those of latter event did not show any appreciable shift compared to its maximum phase at about 0730 UT in Figure III-6. Then one may ask why such a shift of the auroral electrojets was possible in one epoch but not in the other. The readily recognizable difference found from in Figures III-1 and III-2 is that the former epoch (1700 UT on March 17) was in the recovery phase of a major substorm, while the latter (0820 UT on March 18) was in the same phase but was followed immediately by a major substorm. A similar situation was also found in Figure III-3; although the current distributions of the intermediate epochs are not shown, the substorm at about 1100 UT on March 17 did not show such a poleward shift of the auroral electrojets during its recovery phase, and indeed it was also followed immediately by a major substorm. Such a small substorm may be called the weak activity prior to the major activity (WPM). Thus, there is some indication that the auroral electrojets of the WPM type do not seem to shift noticeably poleward during its recovery phase.

Figure III-7 shows other examples of a time sequential development of the current distribution pattern during an intense substorm, the most

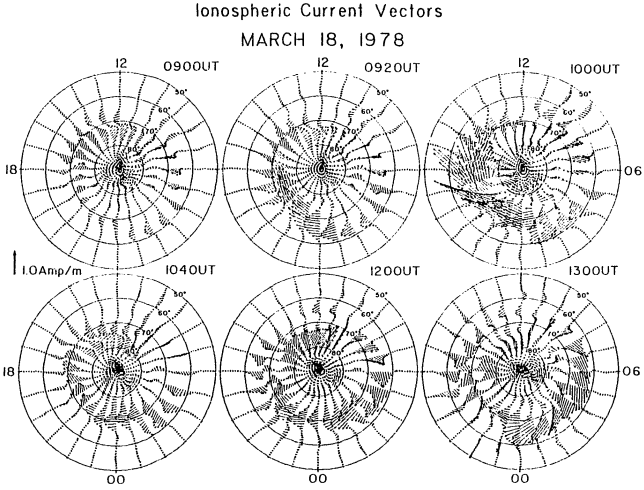

Figure III-7 Same as Figure III-3 for at 0900, 0920, 1000, 1040, 1200 and 1300 UT on March 18, 1978.

intense substorm during the three days used in this study. Since the substorm developed immediately after a small disturbance, it is hard to identify the 'development phase' characteristics. As can be seen from Figure III-2, the AE index increased abruptly from 328 nT to 623 nT within 5 minutes just after 0910 UT. The all-sky photographs from Fort Yukon showed that the faint arc over the southern horizon brightened suddenly at about 0902 UT and the breakup occurred at about 0907 UT. Thus, one may assume that the current distribution pattern at 0900 UT in Figure III-7 has some characteristics of the 'development phase'. It is surprising to find that the overall current pattern at 0900 UT is very similar to that at 1100 UT on March 17 in Figure III-3, in spite of the fact that there was a breakup at 1100 UT on March 17 and no breakup at 0900 UT on March 18. Particularly, the well-developed westward electrojet at both epochs are remarkable. The current pattern in the dayside cusp region of the two events also shows a remarkable similarity except that the whole current system at 0900 UT is located at a slightly lower latitude than that at 1100 UT. Further, one can notice that there was an eastward electrojet along the southern edge of the westward electrojet in the prenoon quadrant of both events. Such a current system was also reported by Rostoker and Hron (1975) and Hughes and Rostoker (1979). As pointed out earlier, however, no similarity was found between the current distributions in the polar cap region for the two events.

It was mentioned earlier that the standard AE(12) index could not monitor the auroral electrojet properly during the period of low

magnetic activity. Here is another interesting example. Let us compare the current distributions at 0730 UT in Figure III-6 and at 0900 UT in Figure III-7. The AE(71) index for the two epochs were 346 nT and 380 nT, respectively. One can notice readily that the main contribution to the index in the former epoch (0730 UT) came from the current flow in the night side auroral zone, while it came from the day side cusp region in the latter epoch (0900 UT). Thus, during the slightly disturbed period, in terms of the AE(71) index, say about 350 nT, even the AE(71) index could not monitor the auroral electrojets properly as far as the night side auroral zone is concerned. This problem is particularly serious during the early phase of substorm, since the strong current flows are found quite often in the dayside cusp region during such a period. See such examples in the current distributions at 1040 UT and 1100 UT in Figure III-3, at 0050 UT and 0100 UT in Figure III-5, and at 0900 UT in Figure III-7. On the other hand, the standard AE(12) indices of the previous two epochs were 347 nT (0730 UT) and 293 nT (0900 UT), respectively. In this case, the index seemed to monitor reasonably the nightside auroral electrojets. This is because the standard AE(12) stations are located latitudinally well below the cusp region. The AE(71) index includes magnetic activities from both the dayside cusp region and the nightside electrojet region, and the former activity tends to obscure the latter activity.

At 0920 UT in Figure III-7, the overall current intensity was enhanced. In particular, note the enhancement of the westward electrojet in the pre-midnight and midnight sectors. Since the

expansion phase seemed to start about 0910 UT, the enhanced current intensity is considered as the result of the DP 1 current (c.f. Chapter 1) in the midnight sector. When the substorm reached its maximum phase at about 1000 UT, the intensity of the westward electrojet was greater than 2.5 A/m. Besides their enhancement in intensity, the belts of auroral electrojets, particularly in the dawn and dusk sectors, were shifted slightly equatorward compared to those at 0920 UT. On the other hand, the eastward electrojet in the early evening sector seemed to be slightly reduced its intensity. Further, it is clear that the westward current in the dayside cusp region seemed to decay, while the eastward current flowing along the southern edge of the former was slightly enhanced.

The current distribution at 1040 UT in Figure III-7 shows an example of the pattern during the recovery phase. Several interesting changes deserve noting. First, the overall auroral electrojet belt seemed to shift poleward. Second, as mentioned earlier, the position of the maximum current density in the westward electrojet moved toward the early morning sector. Third, the current distributions of the polar cap above 80° in latitude and in the dayside sector showed also slight changes. In particular, the changes in the dayside sector are interesting. The poleward shift of the eastward current and the reduction of its intensity seemed to be the characteristics of the recovery phase. On the contrary, the westward current in the dayside cusp region was strongly enhanced. Further, the overall current pattern is more or less similar to that at 0900 UT in the same figure as far as

the dayside cusp region is concerned. Thus, such changes may be related to the early phase characteristics of the subsequent substorm. From Figure III-2, one can see that a new substorm started at about 1040 UT on March 18.

Although there was an abrupt increase of the AE index after 1200 UT on March 18, it is not clear whether the current distribution at 1200 UT of Figure III-7 could be used as an example of the 'development phase'. However, several interesting changes are readily noticed from the current distribution at 1200 UT, compared to that at 1040 UT. First, the enhancement of the eastward electrojet in the entire dusk sector is prominent. Further, it shifted equatorward. Second, the westward current in the dayside cusp region was also prominently enhanced and seemed to connect spatially with the westward electrojet in the dawn sector. Third, the enhancement of the westward electrojet was only noticeable in the dawn sector.

As can be seen in Figure III-2, the period between about 1200 UT and 1600 UT on March 18 was a strongly disturbed one. The average AE index during the period was greater than 900 nT. During such a prolonged period of disturbance, it is hard to determine the exact time of the maximum phase based only on the basis of the AE index. Further, it is not clear whether there were several maxima or not. In spite of such uncertainties one can notice that there were some changes of current distributions during the period. Although the current distributions at 1300 UT in Figure III-7 and 1400 UT in Figure III-8 are quite similar to each other, one can notice that they were different

from that at 1200 UT in Figure III-7. From the comparison of the current distirbutions at 1200, 1300 and 1400 UT, several interesting changes emerge, although such changes were repeatedly discussed from the previous examples. First, the strong westward current in the dayside cusp region decayed noticeably. Second, the westward electrojet was gradually enhanced and shifted equatorward. Particularly such a change was noticeable in the midnight sector. On the other hand, the enhancement of the eastward electrojet was not prominent compared to the westward electrojet. Third, the current distribution at 1400 UT in Figure III-8 has a very complicated structure in the premidnight quadrant and the early morning sector compared to any other previous examples. Since there was a large data gap over the eastern Siberia, one must be cautious in interpreting results. Basically, the harmonic analysis is nothing more than an interpolation. Thus, such an interpolation cannot correctly reproduce features on scales smaller than the distance between observatories (Kroehl and Richmond, 1979). Although there exist a number of geomagnetic observatories between IZMIRAN and Alaska chain observatories, the data gap between the two chains is more than 110° in longitudinal direction. Thus, any feature found in this region should be interpreted with an extreme caution. However, we could not exclude the possibilities of unknown intrinsic reasons, for example due to the multiple onsets and multiple surges (Rostoker et al., 1980).

At 1600 UT on March 18 in Figure III-8, one can see that there are some indications of the recovery phase, which were already pointed

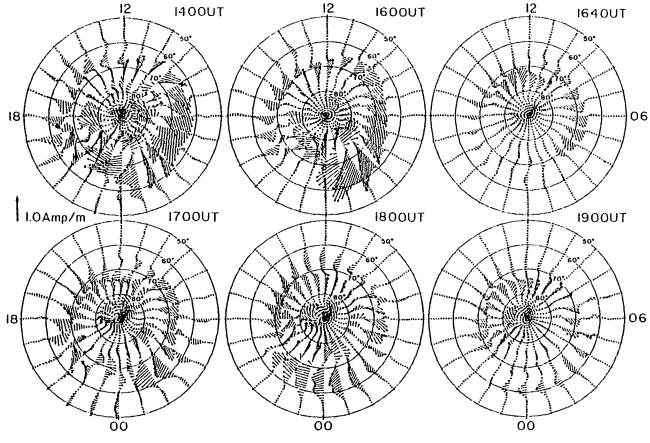

Figure III-8 Same as Figure III-3 for at 1400, 1600, 1640, 1700, 1800 and 1900 UT on March 18, 1978.

out. The auroral electrojets in the dawn and dusk sectors shifted poleward and the maximum current density region of the westward electrojet moved from the midnight to the early morning sectors. The current distribution pattern of the late evening and midnight sectors still showed a very complicated structure. However, at about 1600 UT, the data gap region mentioned above moved in the early morning sector. Thus, there must be some intrinsic reason for the presence of the complicated current pattern in the late evening and midnight sectors.

At 1640 UT, the magnetic activity seemed to be reduced to its minimum level in terms of the AE(71) index. The current distribution at the epoch in Figure III-8 is very similar to that at 1700 UT on March 17 in Figure III-3. The poleward shift of the westward electrojet in the early morning sector is noticeable. Moreover, the center of the westward electrojet also moved from the midnight to the morning sector. However, one can see also some differences between the current distributions at the two epochs. First, the intensity of the westward current in the dayside cusp region at 1640 UT on March 18 is higher than that at 1700 UT on March 17. Second, the eastward electrojet in the dusk sector at the former epoch is located slightly in a lower latitude than that at the latter epoch. Thus, the comparison seemed to suggest that the current distribution at the former epoch (1640 UT) has some early 'development phase' characteristics. From Figures III-1 and III-2, it is clear that the former epoch is followed immediately by the subsequent substorm. However, the current distributions of the two epochs seem to be different with that of the WPM.

The subsequent substorm reached its maximum phase at around 1715 UT on March 18 in terms of the AE(71) index. As can be seen in Figure III-2, however, the substorm seemed to have a complex structure. The current distribution at 1700 UT on March 18 in Figure III-8 shows well developed auroral electrojets in the dawn and dusk sectors. On the other hand, the current pattern in the midnight sector is quite a complicated one. Although it will be discussed later, the change of the current pattern in the dayside cusp region is also worth noting.

In spite of no significant change of the magnetic activity in terms of the AE index from 1700 UT to 1800 UT, some interesting changes can be seen from the current distribution at 1800 UT. First, the westward electrojet in the midnight sector evolved to a well developed one. For comparison, it is worth mentioning that the AE(71) indices of the two epochs, 1700 UT and 1800 UT on March 18, were 582 nT and 593 nT, respectively. On the other hand, the standard AE(12) index recorded exactly same value, 495 nT for the two epochs. Thus, it seems that the auroral electrojet system could be considerably different between two epochs during which the magnetic activities are almost the same in terms of the AE(12) or AE(71) index. Such examples are abundant. The AE(71) index of the epoch 0400 UT on March 19 was 593 nT. Thus, the magnetic activity was quite comparable with those of the two epochs mentioned above in terms of the AE(71) index. However, one can see the corresponding current distribution in Figure III-9 is considerably different with those at the two epochs mentioned above. Further, the

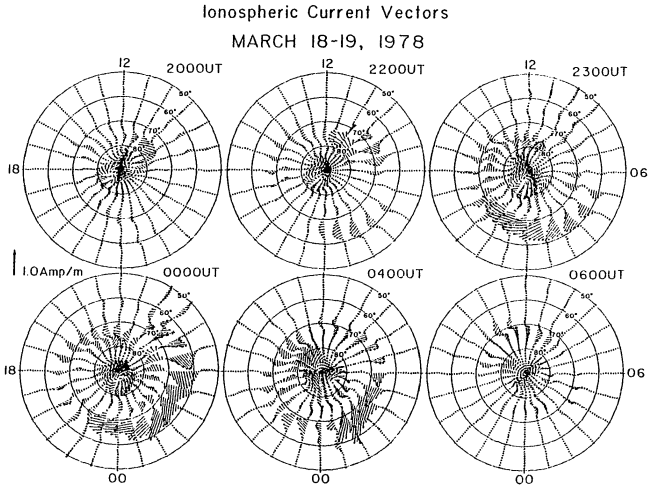

Figure III-9 Same as Figure III-3 for at 2000, 2200, 2300 UT on March 18, 0000, 0400 and 0600 UT on March 19, 1978.

current pattern in the dayside cusp region shows also significant differences.

The current distribution at 1900 UT in Figure III-8 shows the characteristics of the recovery phase. For example, the auroral electrojets in the dawn and dusk sector shifted noticeably poleward. However, there is still a considerably strong westward electrojet in the midnight and early morning sectors. At this moment, it may be worthwhile to examine the change of the IMF in Figure III-2. At about 1600 UT on March 18, there was a brief period of positive values of the B_z component. It seemed to be related to the period of low magnetic activity at about 1640 UT. The subsequent intensifications shown in the current distributions at 1700 UT and 1800 UT seemed to relate with the southward turning of the IMF at about 1630 UT. However, the period was interrupted by a brief northward turning of the IMF at about 1800 UT. Then, the IMF turned southward again for about an hour. Thus, it was expected to have another disturbed condition in the current distribution. However, as can be seen in the current distributions at 1900 UT in Figure III-8 and 2000 UT in Figure III-9, no definite signature of the 'development phase' was found. The only one found, as mentioned above, was the relatively strong westward electrojet in the midnight and the early morning sectors at 1900 UT in Figure III-8. Thus, the brief southward turning of the IMF seemed to be responsible for it.

The current distribution at 2000 UT in Figure III-9 showed a magnetically quiet condition which seemed to be the result of the north-

ward turning of the IMF at about 1900 UT on March 18. Although there is a hint of the westward electrojet in the midnight sector, the current pattern at 2000 UT is characterized by a strong current flows in the dayside cusp and the polar cap regions. Since the subsequent substorm occurred about one hour and a half later, the current distribution at 2000 UT seems to represent the condition near the very end of the recovery phase. A similar example can be found at 0600 UT on March 19 in Figure III-9.

The southward turning of the IMF shortly after 2100 UT on March 19 seemed to trigger another substorm. The current distribution at 2200 UT in Figure III-9 showed a well-developed auroral electrojet system except in the pre-midnight sector. There seemed to be a discontinuity in the westward electrojet in the dawn sector. This is partially understood, since the zone coincides more or less with the large data gap mentioned earlier. The strong current flows in the high latitude zone of the prenoon quadrant is quite similar to that at 0100 UT on March 18 in Figure III-5. In the next section, such current flows will be discussed further. Shortly after 2300 UT, the substorm seemed to reach its maximum phase.

The flow pattern of the westward electrojet at its maximum phase of the different substorms sometimes has a very complicated structure. For example, the westward electrojets at the epochs at 1200 UT on March 17 in Figure III-3, at 0200 UT on March 18 in Figure III-5, at 2300 and 2400 UT on March 18 in Figure III-9 and at 1200 UT on March 19 in Figure III-12, have a relatively simple structure, while those at 1500 UT on

March 17 in Figure III-3, at 1000 and 1300 UT on March 18 in Figure III-7, at 1400 UT on March 18 in Figure III-8 and at 1600 UT on March 19 in Figure III-12 have a complicated structure. There is an indication that the stronger the magnetic activity, the more complicated the structure of the westward electrojet. However, one can notice that the simple type of the westward electrojet is usually found in the substorm which is the first one of multiple onset type substorm (or substorm sequence) or an isolated one. Thus, when a new substorm starts before the previous one subsides, the signatures of the both substorm seem to co-exist. Wiens and Rostoker (1975) showed that when the westward electrojets develop in succession, the new electrojet appears to the northwest of the previous one. Their result may be understood as an effect of superposition of the westward electrojets as a result of successive substorms.

The current distributions at 2300 and 0000 UT in Figure III-9 show the maximum phase characteristics of a substorm. The well-developed electrojet system is remarkable. Note that the weak westward current flowing along the northern edge of the eastward electrojet in the dusk sector seems to be interrupted near the dayside cusp region by the eastward current which originated in the dawn sector along the northern edge of the westward electrojet. Thus, one can see that there is a pair of currents flowing in the opposite directions along the entire auroral zone. This topic will be discussed in the next section. At about 0400 UT on March 19, the center of the westward electrojet moved toward the morning sector and the eastward electrojet in the dusk sector shifted

poleward. Thus, it is definitely a characteristic of the early recovery phase. On the other hand, the pattern at 0600 UT seemd to be an example of the late recovery phase.

Since the substorms examined so far were followed by another within less than two hours, it was hard to figure out a reliable current distribution pattern during a quiet period and the 'development phase'. From such a view point, the substorm which reached its maximum phase shortly after 1200 UT on March 19 is a good example for this particular purpose, since the substorm started after an almost four-hour long quiet period. Although it is not enough time for the magnetosphere to return to its ground state from the previous disturbance (Kamide et al., 1977), it is the best example of the three day data used in this study. As can be seen from Figure III-2, the IMF B_z component showed positive value during the period.

The purpose of Figure III-10 is to show how the current distribution of the 'early' phase of a substorm evolves. In order to examine the weak current density during its low magnetic activity, we adopt a different scale value here for this particular purpose. In Figure III-10 the scale of the current density is increased 2.5 times compared with all the other figures to examine the weak activity. The current distribution at 0830 UT in Figure II-10 shows a very complicated structure. Thus, one may consider that all features might be due to the noises from the numerical procedure used in this study. However, several interesting features deserve mentioning. First, although it looks irregular, the current distribution in the entire auroral zone

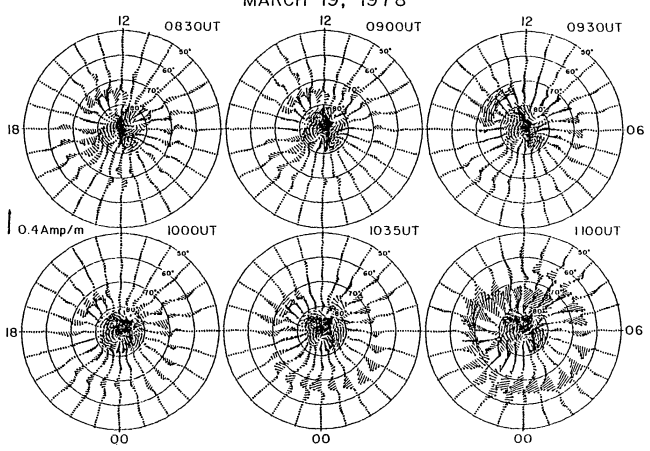

Figure III-10 Same as Figure III-3 for at 0830, 0900, 0930, 1000, 1035 and 1100 UT on March 19, 1978. Note that a different scale value is used in this figure.

shows rather strong east-west component. Further a pair of oppositely directed current flows were found in both dawn and dusk sectors. Let us compare the current pattern with that at 0000 UT on March 19 in Figure III-9. One can see that the directions of the current flows in the entire auroral zone are almost opposite in both epochs. Second, the relatively strong current flows in the dayside cusp region are common features during quiet period. Third, the strong current vortices in the polar cap region were also mentioned repeatedly as a characteristic during such a period. Thus, in spite of its apparent irregularity, the current pattern at 0830 UT suggests several interesting features during quiet period. At 0900 UT, the current distribution shows some changes compared to that at 0830 UT. Particularly, the eastward electrojet in the auroral zone in the morning sector became quite prominent, while the westward electrojet along the northern edge of the former noticeably reduced its intensity. However, no significant change is found in the current pattern of the dusk sector. Such an eastward electrojet in the morning sector was already mentioned in the current distribution at 0550 UT on March 18 in Figure III-6.

It is worthwhile to compare such changes of the current distribution with those of the IMF. However, one must take into account that the delay time of the ionospheric response to the IMF change is about 10 to 40 minutes. Thus, it is hard to identify exactly specific changes of the ionospheric current distribution with the corresponding IMF changes. In spite of such uncertainty, one can get a rough idea that the current distribution between ~0730 UT and 0930 UT in Figure III-10

was reflecting the condition during which the IMF B_z component was positive between ~0600 UT and 0815 UT. From Figure III-2, however, it is not clear whether the IMF B_y component was positive or negative during this particular epoch, because it had irregular changes of 'period' of ~30 minutes. At about 0830 UT, the IMF B_z component became null, while the B_y component definitely showed a positive value.

At 0930 UT, there was an interesting change in the ionospheric current distribution compared to that at 0900 UT. The unusual eastward electrojet in the morning sector was replaced by a westward electrojet. Another interesting point was that there was almost no change in the pre-midnight sector, except the slight reduced current density. At 1000 UT, one can see a well-developed westward electrojet in the auroral zone. Although it is not quite prominent, there is also an eastward electrojet in the early evening sector. The uncertainty in the early evening sector seems to come partially from the data gap in that region.

Although there was no significant change of the magnetic activity in terms of the AE index, noticeable changes in the current distribution occured during the four instants discussed above. In other words, the unorganized current distribution pattern at 0830 UT has evolved into that of a substorm period. An interesting point is that the IMF B_z component was close to null or positive at that time or earlier, but not negative. Thus, the decrease of the IMF B_z component from about ~4 nT to ~0 nT could have triggered the growth of the substorm pattern.

At this point, it is appropriate to consider the relation between the current distribution pattern and the AE index during such a period of low magnetic activity. First, it is useful to know the AE(71) indices of the instants. They were 111, 121, 191 and 95 nT at 0830, 0900, 0930 and 1000 UT, respectively. In this context, it may be worth mentioning the recent results of Kamide and Akasofu (1982) and Akasofu et al. (1983). They showed that the standard AE(12) index below 250 nT could not properly monitor the auroral electrojets. Thus, it is a nice opportunity to examine again whether the new AE(71) index could properly monitor the auroral electrojet, since we have the current distributions during the period of such a low magnetic activity. One can easily see that in spite of the lowest AE(71) index value, the best example of a well-developed auroral electrojets was found at 1000 UT. Further, it is hardly true that the current distribution at 0930 UT has more well defined and stronger auroral electrojets than that at 1000 UT, in spite of its higher AE(71) index. There was even an eastward electrojet in the morning sector auroral zone at 0900 UT, although the AE(71) index of the moment is quite comparable with that of 1000 UT. Thus, during periods of low magnetic activity, it seems that even the AE(71) cannot monitor the changing patterns of the auroral electrojet activity. Moreover, the magnitude of AE(71) is not reliable during such periods.

It is worthwhile to review several interesting features in the polar cap region during the period of low magnetic activity in conjunction with the recent observational and theoretical studies of the region. First, according to the observations (Lassen, 1969, 1972, 1979;

Eather and Akasofu, 1969; Berkey et al., 1976; Meng and Akasofu, 1976; Lassen and Danielson, 1978; Ismail and Meng, 1982) the polar cap arcs tend to appear during magnetically quiet periods or during periods when the IMF B_z component is positive. Moreover, they are not observed during strongly disturbed periods. Such observations seem to be closely related with the fact that during quiet periods the polar cap current density is relatively strong compared with that in the auroral zone. Second, the current pattern in the polar cap basically consists of several current vortices. In spite of such complexities in the current pattern, one can see that there exist similar patterns both in the examples of Figures III-6 and III-10. There are two current vortices in the polar cap region above 80° in latitude in the examples of Figure III-6. One in the dawn sector has a clockwise vortex and the other in the midnight sector has a counterclockwise vortex. In the dusk sector, however, there is an approximately sunward current flow. On the other hand, there seem to be three current vortices in the examples of Figure III-10. The two vortices, one in the post midnight quadrant and the other in the pre-noon quadrant seem to correspond to the two vortices mentioned above in the examples of Figure III-6. Furthermore, since the third vortex located approximately in the pre-midnight quadrant has a large sunward current component, it seems to relate with the sunward current flow in the examples of Figure III-6. It is interesting to point out that Horwitz and Akasofu (1979), Burke et al. (1979, 1982) and Akasofu and Roederer (1983) showed that during the periods of the IMF $B_z>0$, there occurs a four-cell pattern of convection instead of two.

Although the current pattern at 0830 UT in Figure III-10 and other examples of the low magnetic activity period in this study are not good enough to suggest any definite convection pattern, the strong current vortices in the polar cap region and the reversed current flows in the auroral zone may reflect the characteristics of magnetically quiet period.

Figure III-11 shows the all sky photographs over Fort Yukon during the period from 1021 UT to 1140 UT on March 19. There was no auroral activity until 1021 UT. A faint arc appeared suddenly over Fort Yukon at 1021 UT. Then it brightened and started to expand poleward at 1031 UT. Before arriving at the northern horizon, however, it faded out suddenly at 1037 UT. Since then, the faint arc moved gradually toward the southern horizon. Simultaneously another faint arc appeared over the northern horizon at about 1056 UT. Thus it is clear that there were two substorm activities during the period. If one uses only the AE index data, however, an enhanced AE after about 1030 UT on March 19 could be misidentified as a growth phase feature. In order to see further evidence of the small substorm, a portion of the riometer data from Inuvik, Fort Yukon and College were examined. As can be seen in Figure III-12, a small absorption was recorded at about 1030 UT. Moreover, it was only appreciable in Fort Yukon riometer. On the other hand, the one recorded at about 1135 UT was noticeable in all three station riometers, although it was recorded slightly later in the Inuvik riometer. Thus, it is further concluded that the substorm was very small and the activity was restricted in the narrow region. This

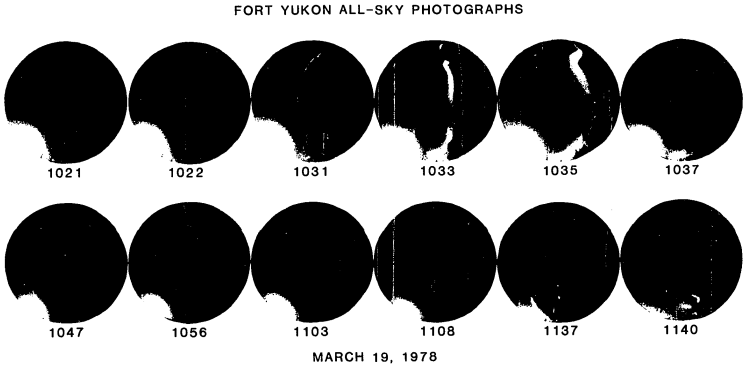

Figure III-11 The all-sky photographs of aurora taken at Fort Yukon.

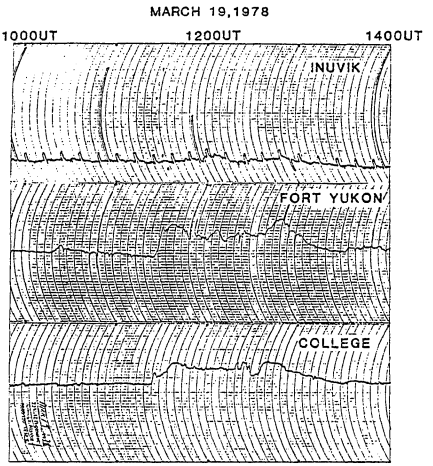

Figure III-12 The riometer records from Inuvik, Fort Yukon and College.

suggests that the substorm seems to be a WPM type; it showed a clear expansion phase at about 1020 UT. It is also interesting to note that the westward electrojet belt at 1035 UT in Figure III-10 is narrow. Furthermore, one can see that the belt was roughly over Fort Yukon (69° in the eccentric dipole coordinate). This means that the zone of the westward electrojet is matched more or less with the high absorption region or with the high Hall conductivity. Such a trend was already reported by Ahn et al. (1982) (c.f. Chapter II).

As mentioned earlier, there seems to be no distinct difference in the ionospheric current distributions of the auroral zone between the 'development phase' at 0930 UT and the expansion phase at 1020 UT in Figure III-10, except that the latter epoch has stronger current density than the former.

According to Nishida and Kamide (1982), there is an interval lasting about one hour between the IMF southward turning and the onset time of the substorm expansion phase during which the equivalent current system of the DP 2 type is developed. Thus approximately an hour before the onset time, 1035 UT, roughly the interval from 0930 UT to 1030 UT on March 19 seems to be a similar period suggested by Nishida and Kamide (1982). Therefore, the current distribution at 1000 UT in Figure III-10 might be taken as an example of such a phase. As mentioned repeatedly, however, it is hard to see any signature of the DP 2 current, as far as the ionospheric current distribution is concerned. Although they were not shown here, the current distributions at the intermediate epochs between 0930 UT and 1030 UT also did not show such a signature.

Further, the equivalent current systems during the period were examined. A noticeable twin-vortex current system occurred only after about 1035 UT. Thus, it was no longer the characteristics of the growth phase, since the expansion phase started at around 1035 UT.

The current distribution at 1100 UT in Figure III-10 seemed to have the characteristics of both the recovery phase and 'development phase', since the epoch coincided with the period between two auroral breakups. However, the enhanced current intensity in the dayside sector and the polar cap region seemed to represent characteristics of the 'development phase' or the early phase of a substorm. Further, one can notice that the intensity of the auroral electrojet in the night hemisphere was also enhanced compared to that at 1035 UT. Moreover, the auroral electrojets did not shift poleward. Such trends were already pointed out during the recovery phase of a small substorm which is followed immediately by a major one. Thus, there seems no definite recovery phase signature for such a WPM type. Throughout this study, it is not clear whether such a type of substorm is an independent one or simply a portion of the subsequent major one.

Besides the slight overall enhancement, the current distribution at 1135 UT on March 19 in Figure III-13 shows several interesting changes compared to that at 1100 UT in Figure III-10. Particularly, there was a noticeable change in the current pattern of the dayside cusp region. It will be discussed further in the next section. There were also appreciable changes in the current pattern of the polar cap region.

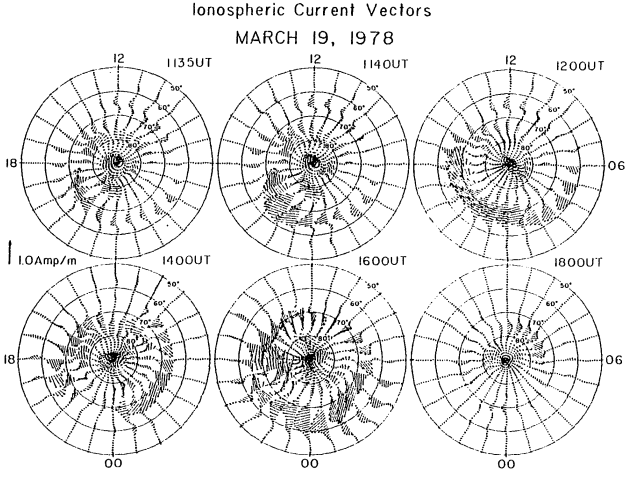

Figure III-13 Same as Figure III-3 for at 1135, 1140, 1200, 1400, 1600 and 1800 UT on March 19, 1978.

Note the sharp turning of the current direction in the pre-midnight sector around 80° in latitude.

It is interesting to compare the simultaneous all-sky photographs, magnetograms and riometer data. As mentioned earlier, there was a sudden brightening of aurora over Fort Yukon at about 1137 UT. The riometer data from the three stations in Figure III-12 show that there was a major cosmic radio noise absorption at about 1135 UT. Note the gradual delay of the onset time toward higher latitude observations. Further one can see that the AE index increased from 263 nT to 565 nT within 5 minutes at about 1135 UT. Thus, these observations confirm that the auroral and ionospheric substorms started simultaneously with the onset of the expansion phase of the polar magnetic substorm (Akasofu, 1968).

The current distributions at 1135 UT and 1140 UT in Figure III-13 were selected based on the above consideration. One can see that there was a sudden enhancement of the westward electrojet in the pre-midnight sector. However, it should be taken into account that the region is roughly matched with the missing data zone mentioned earlier. Thus it is concluded that a portion of the westward electrojet around the midnight sector or the late evening sector is suddenly enhanced during the early expansion phase, although there is some ambiguity of the exact location of the enhancement. The enhanced portion of the westward electrojet spreads gradually toward both the dawn and dusk sectors, as the substorm intensified. When the substorm reached its maximum phase at about 1200 UT, there was a fully developed westward electrojet in the

entire nightside sector. As mentioned earlier, however, the eastward electrojet in the evening sector did not show any appreciable enhancement.

The recovery phase of the substorm has also quite similar characteristics as those of the examples already examined. From the current distribution at 1400 UT in Figure III-13, one can see that the center of the westward electrojet moved toward the morning sector and the whole auroral electrojet system shifted poleward. The discontinuity of the westward electrojet in the pre-midnight sector seemed to relate with the data gap region mentioned earlier. On the other hand, the strong eastward electrojet in the dusk sector is quite unusual. Accordingly, the AU(71) index during the period increased prominently in Figure III-2. However, it is not clear why only the eastward electrojet was enhanced during the period.

At about 1600 UT, the substorm intensified again. As mentioned earlier, the current distribution during such multiple onsets shows a complicated structure. Note again the change of the current pattern in the dayside cusp region at 1600 UT in Figure III-13. The current distribution at 1800 UT is an example of the recovery phase. In spite of such a low magnetic activity, there is a well-developed auroral electrojet system. The strong westward current in the prenoon sector seems to be related with the dayside cusp region. Note the weak eastward electrojet in the dawn sector. Such a current system was observed frequently throughout this study. According to Rostoker and

Hron (1975), the chance of observing such a current system is about 50% in the prenoon quadrant.

(b) The ionospheric current pattern in the dayside high latitude zone

The effect of the IMF B_y component on the magnetic variations in the polar cap was found by Svalgaard (1968, 1972, 1973). Since then, a number of papers have been published on this subject. Most of these studies were based on the averaged data over an extensive period. Recently, Friis-Christensen and Wilhjelm (1975) and Akasofu et al. (1980) studied the subject using the magnetic meridian chain data. However, the studies have dealt only with the equivalent current distribution. More recently, Rostoker (1980) and Friis-Christensen et al. (1982) re-examined the subject based on the ionospheric current distribution using the University of Alberta and the Greenland meridian chain data, respectively. Unfortunately, they showed only the averaged conditions. Thus, in this section it is attempted to examine this topic using the instantaneous data set.

Let us compare the current pattern at 1100 UT in Figure III-10 with that at 0900 UT on March 18 in Figure III-7. The AE(71) index of the two epochs were 249 nT and 380 nT, respectively. In spite of the different degree of magnetic activities in terms of the AE index, one can see that the two current distribution patterns are quite similar to each other as far as the current patterns in the dayside cusp and the polar cap regions are concerned. In particular, note the current pattern in the postnoon sector at 0900 UT in Figure III-7, which

consists of a westward current in the higher latitude zone and an eastward current along the southern edge of the former. Almost the same type of current pattern is also found in the postnoon sector at 1100 UT in Figure III-10. However, there is an indication that the pattern at 1100 UT seemed to be located slightly in later afternoon sector than that at 0900 UT. In order to clarify this matter further, it seems helpful to examine the relative locations of the current vortices in the polar cap region of both the epochs. Note the current vortex in the prenoon quadrant. The center of the vortex at 1100 UT was located along 1000 - 1100 MLT meridian, while at 0900 UT it was located along 0800 - 0900 MLT meridian. Furthermore, the center of current vortex in the post-midnight quadrant at 1100 UT is located along 0300 - 0400 MLT meridian, while at 0900 UT it is located along 0200 MLT meridian. Thus, if the whole current pattern at 1100 UT is rotated in clockwise direction about 30°, one can see a number of features of the two current distributions can be identified in almost the same local time zone. However, one must be cautious in comparing the current patterns of different UT, since they might include UT dependent factors which result from the distribution of the six meridian chain stations and the resulting effect of conductivity distribution. Thus, it is desirable to examine another example. One can see that the current pattern at 1100 UT on March 17 in Figure III-3 has a similar orientation with that at 1100 UT on March 19 in Figure III-10 by rotating about 30° in counterclockwise direction. Although it is not a well-developed one, the current pattern at 0700 UT on March 18 in Figure III-6 has a quite

similar orientation with that at 0900 UT on March 18 in Figure III-7 without any rotation.

It is appropriate to recall that according to Ahn et al. (1982), the high Hall conductivity zone is more or less coincided with the westward current region. Thus, one can see, for example at 0900 UT March 18 in Figure III-7, that the zone of westward electrojet seems to delineate roughly an auroral oval. Moreover, it is interesting to note that the 'major axis' of the oval lies approximately along (1400-1500)-(0200-0300) MLT meridian through the pole. Here, the auroral oval is assumed to be represented by an elliptical shape and 'the major axis' means simply the longer axis of the ellipse. Such an axis can be drawn easily whenever there is a well developed westward electrojet. For example, the axis seems to lie approximately along the 1600 - 0400 MLT meridian at 1100 UT on March 19 in Figure III-10. However, it is not always easy to determine unambiguously the orientation of the axis with respect to the noon-midnight meridian, particularly when the oval is far from a closed circular shape. However, even in such a case, one can still get a hint of the axis by examining the current pattern of the dayside high latitude zone. Let us examine again the current distribution at 1100 UT on March 19 in Figure III-10. In particular, note the current pattern in the late afternoon sector. It basically consists of a westward current in the higher latitude zone and an eastward current along the southern edge of the former. The 'major axis' introduced above seems to lie along the meridian where the most strong current flows are found, say around 1600 MLT meridian, as far as

the current distribution in the dayside sector is concerned. Further, the axis determined from the dayside current pattern seems to pass the meridian where the westward electrojet shifted farthest equatorward in the night sector auroral zone. One can see that a similar current pattern is also found in the late afternoon sector at 1700 UT on March 17 in Figure III-3, except that the whole pattern shifted poleward compared to the previous example. Thus, it seems always possible to find out a 'major axis' of auroral oval.

One can notice that there are two different types of current patterns, as far as the dayside high latitude zone is concerned. Compare the current distribution of the dayside sector at 0900 UT on March 18 in Figure III-7 with that at 1400 UT on March 17 in Figure III-3. One type of current pattern represented by that at 0900 UT on March 18 consists of a westward current between 70° and 80° in latitude and an eastward current along the equatorward edge of the former. On the other hand, the other type represented by that at 1400 UT on March 17 has an oppositely directed current system compared to the first type. Further, the characteristic current pattern in the dayside seems to be located in the postnoon quadrant in the former type and the prenoon quadrant in the latter type. Note that the characteristic pattern at 1400 UT on March 17 occurred in the prenoon quadrant. Thus, it seems reasonable to draw a 'major axis' along 0900 MLT and 2100 MLT meridians, in spite of an ambiguity in the current distribution of the pre-midnight quadrant. Although examples of the latter type are not common in the data set used in this study, some of them are found in the current distributions at

0100 UT on March 18 in Figure III-5, 2200 and 2400 UT on March 19 in Figure III-9 and 1400 UT on March 19 in Figure III-12.

Using the average data observed at the magnetometer chain on the west coast of Greenland, Friis-Christensen et al. (1982) showed that there are two types of current patterns in the dayside high latitude region depending on the sign of the IMF B_y component. Since they used the average data, it is a good opportunity to compare their results with ours based on the instantaneous data. Unfortunately, the IMF data the entire periods were not available. Further the sign of the B_y component was mostly negative during the period used in this study. On March 17, 1978, only hourly averaged data are available for several hours (King, 1981). The data of the other two days are shown in Figure III-2 together with AE index.

As pointed out above, there seem to be basically two types of current pattern in the dayside high latitude zone. According to the results of Friis-Christensen et al. (1982), the former and latter patterns seem to correspond to their results during the periods of negative and positive B_y, respectively. A similar type of study has been made by Kamide and Akasofu (1982, unpublished) by using the Alaska meridian chain data. The current distributions (a) and (b) in Figure III-14 (Kamide and Akasofu, 1982) represent the conditions during $B_y < 0$ and $B_y > 0$ periods, respectively. They are basically similar to the results (their Figure 7) of Friis-Christensen et al. (1982). Rostoker (1980) also obtained quite similar patterns (his Figure 7). As a matter of convenience, let us call the current pattern at 1100 UT and 1400 UT

in Figure III-3 as the 'type A' and 'type B', respectively. The current pattern of the 'type A' occurs quite often in the postnoon quadrant and the 'type B' in the prenoon quadrant. One can see the 'type A' and 'type B' are quite similar to the current patterns of the 'toward sector' and 'away sector' periods in Figure III-14, respectively.

The angle ϕ in the Figure III-14 (Kamide and Akasofu, unpublished, 1982) is measured from the noon-midnight meridian to the 'major axis.' As mentioned earlier, the angle seems to change its direction and magnitude. It is worthwhile to mention the results of Meng et al. (1977). Using the DMSP auroral photographs, they introduced an off-center circle to fit the quiet auroral distribution. If a straight line is drawn connecting the center of the circle and the geomagnetic north pole, one can see that the straight line thus obtained looks quite similar to the 'major axis.' Thus, their Figures 1b, 2b and 3b seem to correspond with the 'B', 'A' and 'B' types, respectively.

It is interesting to note that how the westward electrojet in the night side auroral zone is spatially related to the westward current in the dayside high latitude zone. At 0900 UT on March 18 they were connected to each other and formed a closed oval shaped current system. At 1400 UT in Figure III-3, however, the strong eastward current in the dayside cusp region prevents such a spatial interconnection. One can also see that there is a similar pattern at 0000 UT in Figure III-9.

So far, no exact information is available for the delay time of the ionospheric response to the IMF change. Thus, it is hard to test the

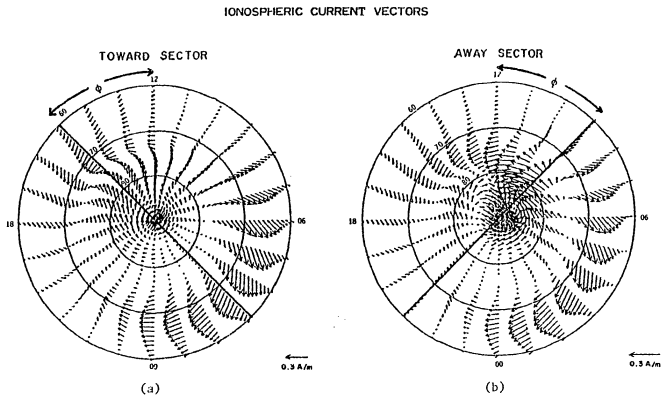

Figure III-14 The distributions of calculated ionospheric current vectors based on the Alaska meridian chain data. The distributions (a) and (b) are based on the two-day averaged data toward (March 31 and April 1, 1978) and away (April 18 and 20, 1978) periods, respectively (Kamide and Akasofu, unpublished, 1982).

current patterns of March 17 in Figure III-3 with only the incomplete hourly averaged IMF data. However, it seemed that the 'type A' current pattern at 1100 UT has evolved to the 'type B' one at 1400 UT. The current pattern at 1200 UT seemed to be the intermediate one of the two types. At 1100 UT, the 'major axis' introduced above lay in the postnoon quadrant and inclined approximately 30° with respect to the noon-midnight meridian. However, it shifted toward the prenoon quadrant and inclined about 30° - 45° with respect to the noon-midnight meridian at 1400 UT. On the other hand, the current patterns in Figure III-5 can be classified as a 'type B' except that at 0300 UT. Since there were missing data during the first half an hour of March 18, it is impossible to compare the current distribution patterns at 0040, 0050 and 0100 UT with the IMF data. According to the results of Rostoker (1980), Friis-Christensen et al. (1982) and Kamide and Akasofu (unpublished, 1982), the epochs 0130 and 0200 UT should be under the influence of the positive B_y component. However, one can see that the IMF B_y component in Figure III-2 shows negative value since 0030 UT on March 18. The current pattern at 0300 UT in Figure III-5 seems to be an intermediate type.

In Figure III-6, it is not easy to decide the current type of the first two examples, while the others may be identified as 'type A's. There was a brief period of positive B_y value which started at about 0530 UT and lasted for about an hour. However, there was no indication of the 'type B' in the current distributions at about 0630 UT. Due to the IMF data gap from 0640 UT to 0800 UT on March 18, the current

patterns at the other epochs in Figure III-6 could not be tested. The current distributions in Figure III-7 have a definite signature of 'type A', except those at 1040 UT and 1300 UT, since the westward current in the dayside cusp region do not seem to be connected with the westward electrojet in the nightside. During the whole period from 0900 UT to 1300 UT, the sign of IMF B_y component was negative except the period of missing data. The current distribution at 1700 UT on March 18 in Figure III-8 seems to be a 'type B' pattern. However, the current distribution at 1640 UT shows a clear indication of the 'type A' pattern. Thus there was a change in the current pattern of the dayside cusp region within 20 minutes. It is interesting to point out that the IMF B_y component changed suddenly at about 1630 UT on March 18 in Figure III-2. In Figure III-9, the current distributions at 2200, 2300 and 2400 UT seem to be 'type B's. Due to the intermittent data gaps during the period, however, it is hard to relate the current pattern with the IMF change.

There was an interesting period during which the IMF B_y component showed an appreciable positive value. It started at about 0820 UT on March 19 and lasted for more than two hours. Unfortunately during the period, the IMF B_z component did not show a noticeable negative value. In other words, the current intensity was not strong enough to decide the current type. Although it is weak, the current distribution at 1035 UT on March 19 seems to show the characteristics of the 'type B'. On the other hand, that at 1100 UT can be classified as a 'type A'. If one takes into account the slight delay of the ionospheric response to the IMF change, the current patterns at 1035 and 1100 UT seem to reflect

the conditions of the positive and negative IMF B_y components, respectively. Note in Figure III-2 that there was a brief period of negative B_y component from 1025 UT to 1100 UT on March 19. The current distributions at 1135 and 1140 UT in Figure III-13 seem to be 'type B's. At about 1100 UT, the IMF B_y component had a positive value. Shortly after that, unfortunately, there was a data gap again. In spite of the data gap, however the distributions at the above two epochs seemed to reflect the condition of positive B_y component, since there is a good reason to believe that the first part of the data gap seemed to be a positive value.

(c) The ionospheric Pedersen and Hall current distributions

It is worthwhile to examine the current distribution patterns of the Pedersen and Hall components separately. For this purpose, the Pedersen and Hall current distributions during 0830 UT - 1800 UT on March 19, 1978 are shown in Figures III-15, III-16, III-17 and III-18. The details of the procedures obtaining the current components are given in Chapter I. Since the Pedersen current has a strong north-south component, the current vectors are shown every 2 degrees in latitudinal direction.

The Pedersen current distribution at 0830 UT in Figure III-15 does not show any systematic pattern, except that there are strong current divergence and convergence in the polar cap region. In spite of the complicated current patterns, it is interesting to point out that the currents in the auroral zone flow mostly in the north-south direction. Since the Pedersen current flows along the direction of electric field,

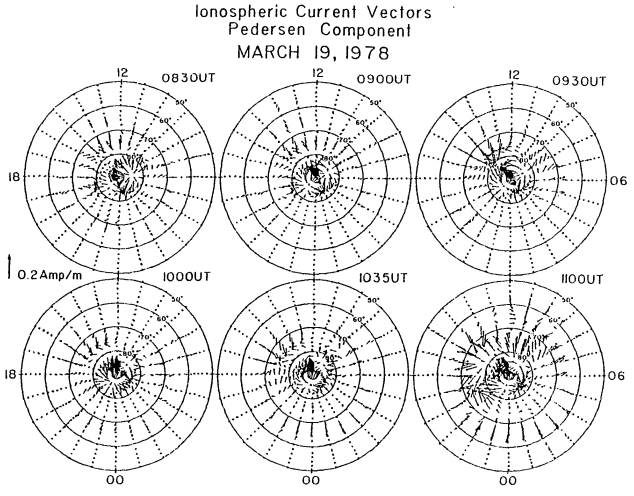

Figure III-15 The ionospheric Pedersen current distributions at 0830, 0900, 0930, 1000, 1035 and 1100 UT on March 19, 1978. Note the scale value is 0.2 Amp/m.

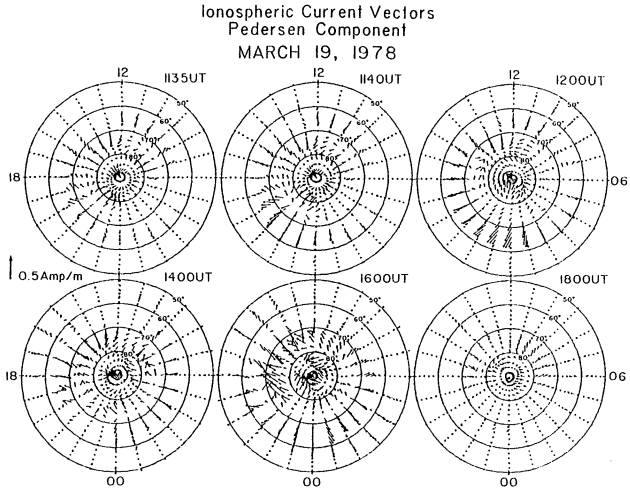

Figure III-16 Same as Figure III-15 for at 1135, 1140, 1200, 1400, 1600 and 1800 UT on March 19, 1978. Note the scale value is 0.5 Amp/m.

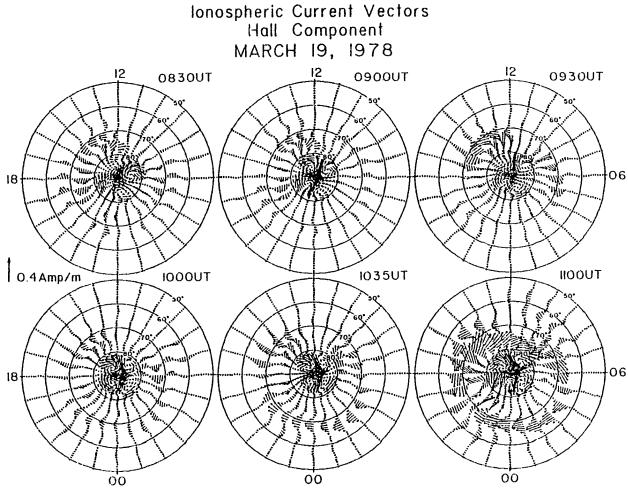

Figure III-17 The ionospheric Hall current distributions at 0830, 0900, 0930, 1000, 1035 and 1100 UT on March 19, 1978.

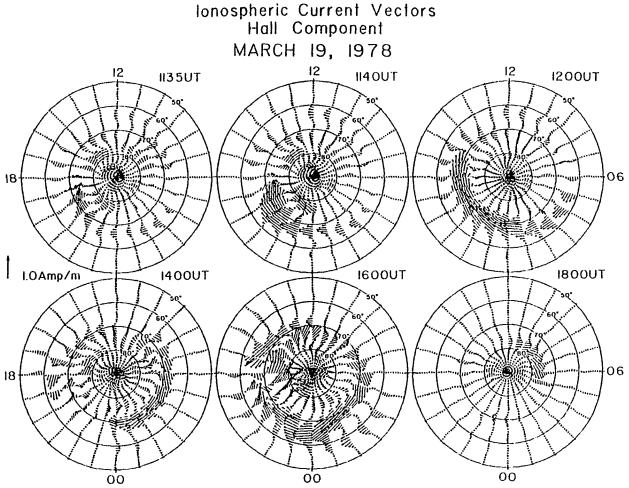

Figure III-18 Same as Figure III-17 for at 1135, 1140, 1200, 1400, 1600 and 1800 UT on March 19, 1978.

it is quite clear that even during such a low magnetic activity period, the direction of electric field is mostly north-southward. Note that there is a pair of current flows approximately 70° in latitude in the dawn sector, which consists of a westward current in the higher latitude zone and an eastward current along the southern edge of the former. On the other hand, one can see another pair of exactly the same but oppositly directed current flows in the dusk sector.

At 0900 UT, however, one can notice that there is a faint northward current flow in the auroral zone of the entire morning sector. Simultaneously the Hall current distribution in Figure III-17 shows a well-developed eastward electrojet along the entire morning auroral zone. Although it is less prominent than the eastward electrojet, a westward electrojet is also found in the dusk sector. If one takes into account the fact that the data gap region mentioned earlier coincides roughly with the dusk sector, it seems quite possible that there is a well-developed westward electrojet in the dusk sector. If this is the case, the directions of auroral electrojet both in the dawn and dusk sectors are exactly opposite to those during the substorm time. Furthermore, the IMF B_z component has positive value during the period. Therefore, there is a possibility that the convection motion is reversed during such a period.

The northward current in the morning sector at 0900 UT is replaced by the southward current in the Pedersen current distribution at 0930 UT on March 19. Simultaneously the eastward electrojet is replaced by the westward electrojet in the corresponding Hall current distribution in

Figure III-17. Such a reverse of the current flow direction was already mentioned in the previous section. During the three epochs mentioned so far, however, no significant changes in the current pattern has occurred in the dayside cusp and polar cap regions. The change in the evening sector of the auroral zone is also less prominent compared to that in the morning sector.

As mentioned earlier, the onset of the substorm occurred approximately at about 1020 UT (Figure III-2). From the Pedersen current distribution at 1000 UT in Figure III-15, however, one can see that the directions of the electric fields in the auroral zone clearly shows substorm conditions; northward in the evening sector and southward in the morning sector. Such a substorm signature is prominent in the corresponding Hall current distribution in Figure III-17.

Both the Pedersen and Hall current distributions during the expansion phase (e.g., 1035 UT) do not seem to be much different from those in the 'development phase' except that the overall current intensity is enhanced. On the other hand, it is interesting to compare the current patterns in the expansion phase with that in the quiet time. For example, let us compare the Hall current distribution at 1035 UT with that at 0900 UT. In spite of the drastic change in the nightside auroral zone, as mentioned above, there is no appreciable change in the dayside cusp and polar cap region. Thus, it is quite possible to assume that the dayside cusp and polar cap regions behave differently with the nightside auroral zone during substorm.

At 1100 UT, the Pedersen current distribution in Figure III-15 shows an interesting change. Note the enhancement of the current in the entire dayside sector. Although there is also an overall enhancement in the current density in the nightside auroral zone, however, it is much less than that in the dayside. Such a strong enhancement in the dayside sector does not seem to relate with the source which is responsible for the enhancement in the nightside auroral zone. However, the current distribution in the polar cap region does not show any noticeable change, except a slight enhancement. Note the current vortices in the Hall current distribution in Figure III-17.

It is interesting to examine the change of the current vortices in the polar cap region. One can see that such vortices are clearly shown in the Hall current distributions. At 0830 UT, two vortices are clearly seen; one in the midnight sector, the other in the morning sector. Note the two vortices have an opposite sense of rotation. At 0900 UT, there were four vortices. Note further the symmetry in the location and the sense of rotation. In spite of a slight change in the current density and location, the overall feature was persistent until 1100 UT. Although such vortices can also be seen in the later epochs (Figure III-18), the intensity is much less than that of the auroral electrojet. Furthermore, it is hard to find any noticeable symmetry in the distribution pattern of the vortices.

As mentioned earlier, the difference between the Pedersen current distributions at 1135 UT and 1140 UT in Figure III-16 is characterized by the enhancement of the current in the pre-midnight quadrant. Note

the significant northward current above 75° latitude in the pre-midnight quadrant. However, such a current flow seems to be a transient feature, since it decayed completely before 1145 UT. Comparing the Pedersen current distribution in the polar cap region at 1135 UT with that at 1100 UT, one can see that there was a drastic change. Moreover, it is hard to find any similarity among the current distributions in the polar cap region at 1200, 1400, 1600 and 1800 UT in Figure III-16. In other words, the current distribution patterns in the polar cap and dayside cusp regions do not seem to be controlled by the factor(s) which is responsible for the auroral electrojet in the nightside auroral zone.

At 1200 UT, the substorm almost reached its maximum phase in terms of the AE index. The Pedersen current distribution at 1200 UT in Figure III-16 shows strong current flows along the north-south direction in the entire auroral zone. The corresponding Hall current distribution in Figure III-18 is quite similar to the total ionospheric current distribution at 1200 UT in Figure III-13. Generally Hall current distribution pattern is similar to that of total ionospheric current except that the former has a smaller north-south component than the later, since Pedersen current usually has a strong north-south component. As the substorm subsided, the westward electrojet shifted to the morning sector and simultaneously to the higher latitude zone. Such a trend is also prominent in the Pedersen current distribution at 1400 UT in Figure III-16. Note the significant reduction of the current intensity in the pre-midnight quadrant. The effect of another intensification at about 1600 UT is clearly seen in both Hall and

Pedersen current distributions. At 1800 UT on March 19, the weak current flow in the dayside sector seems to reflect the quiet time condition. The Pedersen current distribution at the epoch is quite similar to others as far as the current flow in the dayside high latitude zone is concerned. It consists of a current convergence in the dusk sector and a divergence in the morning sector, although they were located slightly in higher latitude zone compared to those at other epochs.

It is worthwhile to compare the instantaneous Pedersen and Hall current distributions with the average ones obtained from the Alaska meridian chain data. Figures III-19 and III-20 show, respectively, the Pedersen and Hall current distribution based on the average Alaska meridian chain data (Akasofu et al., 1983). One of the main features of the distribution of the Pedersen current is the southward directed component in the latitudinal belt between 62° and 72° in the morning sector and a northward directed component in the same latitudinal belt in the afternoon sector. These north-south currents across the auroral oval are connected to the region 1 and 2 field-aligned currents. Note in particular the local time ranges in which the northward and southward currents are present. Note also how systematically their intensity varies as a function of latitude.

Another prominent feature of the Pedersen current is divergence of the current from about 76° in latitude in the midmorning sector and convergence toward the same latitude in the afternoon sector. Associated with this particular feature, there is a fairly intense

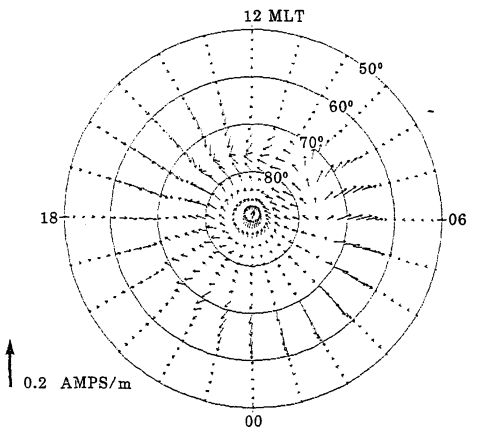

Figure III-19 The distribution of the Pedersen current in magnetic latitude-MLT coordinates based on Alaskan meridian chain data (Akasofu et al., 1983).

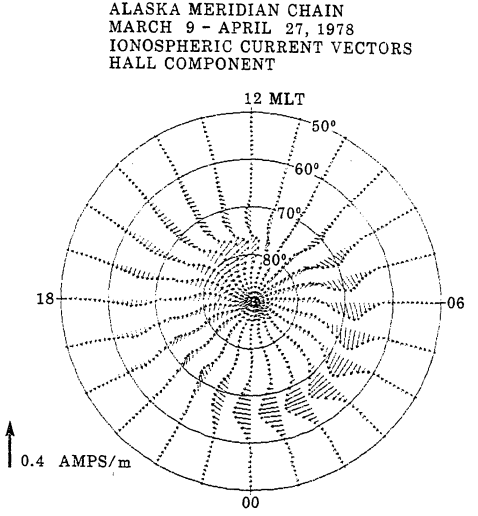

Figure III-20 Same as Figure III-19 for Hall current.

eastward component in the latitudinal belt between 70° and 80° in latitude in the day sector. The Harang discontinuity is manifested by a narrow belt in the late evening sector, along which a westward component of the Pedersen current flow and toward which a northward component flows from lower latitudes and a southward component flows from higher latitudes.

Such features are also prominent in the instantaneous distributions. However, it should also be mentioned that there are differences between the instantaneous and average distributions. First, as mentioned above, the instantaneous current distribution pattern in the polar cap region is noticeably different with the average one. Thus, there seems to be some other factor(s) which control the polar cap current distribution pattern. Second, the instantaneous current pattern in the pre-midnight quadrant shows noticeable difference from the average one. Such a difference is prominent particularly during expansion phase. The westward traveling surge seems to be responsible for it. Thus, there is a possibility that such a strong localized phenomenon produces a misleading picture of the overall current distribution pattern in the pre-midnight quadrant. Particularly, it is serious when the number of magnetometer stations is insufficient to give a good spatial resolution.

The average Hall current distribution (Figure III-20) is characterized by an intense westward component in the latitudinal belt between 62° and 72° in the morning sector and an eastward component in the same latitudinal belt in the afternoon sector. Such a distribution

is again expected from a large number of past studies, most recently by Hughes and Rostoker (1977, 1979), Rostoker and Hughes (1979) and Rostoker (1980). Note the diverging trend of current at about 75° in latitude in the day sector, together with two crescent flow patterns. In the past, many workers assumed that all Hall current lines close themselves in the ionosphere, forming two cells located in the morning-forenoon and the afternoon-evening sectors, respectively. Figure III-20 shows conclusively that such a practice is incorrect, in particular for the westward electrojet. At the "tips" of the two crescent patterns, the Hall current must be associated with field-aligned currents, a downward current from about ~1100 MLT sector and an upward current from about ~2200 MLT sector. In the Harange discontinuity region, the Hall current extends from the morning sector and has a significant northward component.

The differences between the instantaneous and average Hall current distribution patterns are found again in the polar cap region and the pre-midnight quadrant.

CHAPTER IV ENERGY DISSIPATION RATE OF THE POLAR IONOSPHERE

1. Introduction

The energy coupling between the solar wind and the magnetosphere is one of the key problems in magnetospheric physics. To study this problem it is important to estimate as accurately as possible the total energy dissipation rate U_T of the magnetosphere (cf. Akasofu, 1981). It is defined as the sum of the ring current energy injection rate U_R, the Joule heat production rate U_J in the polar ionosphere, the auroral particle energy injection rate U_A and others, namely

$$U_T = U_R + U_J + U_A + \ldots$$

In order to monitor, U_R, U_J, U_A, etc. on a continuous basis, as a function of time for an extended period, it is necessary, at present, to rely on geomagnetic indices; for a review of this particular subject, see pp. 128-130 and 185-188 in Akasofu (1981).

The International Magnetospheric Study (IMS) has provided us an opportunity to examine the relationship between U_J and U_A and the geomagnetic indices AE and AL, since six meridian chains of magnetometers were operated during the IMS. The computer method (Kamide et al., 1982a) to deduce the instantaneous distribution of ionospheric currents over the entire polar region on the basis of the six IMS meridian chain data is given in Chapter I.

One of the problems in this and many other studies of the polar current and electric-field studies has been that the instantaneous distributions of the height-integrated Hall (Σ_H) and Pedersen (Σ_P) conductivities over the entire polar region are not available. It is for this reason that Ahn et al. (1982) have devised a method to estimate empirically both Σ_H and Σ_P as a function of the north-south component (ΔH) of the horizontal magnetic disturbance vector (by using the Chatanika radar data and the simultaneous magnetic data from College), together with an appropriate latitudinal weighting function. For details, see Chapter II. Furthermore, they found that the auroral particle energy injection rate u_A is related to Σ_H and thus statistically to ΔH as well. The purpose of the present chapter is to present the relationships of U_J and U_A thus obtained with the two geomagnetic indices AE and AL.

2. Joule Heat Production Rate

The Joule heat production rate u_J (mwatt/m^2) is at a point defined as

$$u_J = \underline{I} \cdot \underline{E} = I_P E$$

where I, I_P and $\underline{E}$ are the height-integrated total current density, Pedersen current density and the electric field, respectively. Both quantities are a function of latitude and longitude. Thus, one needs the simultaneous measurement of E and I_P. The global Joule heat

production rate U_J is obtained by integrating u_J over the entire polar region.

Fortunately, the recent radar measurements of E and I_p has shed some light on the estimate of u_J, since they make it possible to estimate the Joule heat production rate for the first time. Most recently, Vickrey et al. (1982) estimated the Joule heat production rates within the latitudinal range of 62° - 68°, using the Chatanika radar measurements. Unfortunately, however, the radars would not measure simultaneously both the conductivities and electric fields for a wide range of the latitudinal and longitudinal directions with a time resolution of 5-10 minutes. This limitation is particularly serious when one attempts to infer how the Joule heat production rate varies over the entire polar region during individual substorms. Since it is unrealistic to build numerous radars or sounders to monitor the global distribution of E and Σ_p, we attempt to combine the past results of the radar and geomagnetic studies for our particular purpose.

Our inputs are instantaneous distributions of the ground magnetic perturbation vectors obtained from the six IMS meridian chain stations and standard magnetic observatories. We used data from 71 stations for three consecutive days, March 17, 18 and 19, 1978, with a 5-minute time resolution. Figure I-9 shows the combined X_m component (i.e., northward component in eccentric dipole coordinates) from all the 71 stations of three consecutive days, March 17, 18, and 19, 1978 (Kamide et al., 1982a). During the period used in this analysis, there occurred a number of intense and weak substorms. In the first part of this chapter

we chose four times to show how we obtain U_J and U_A; the epochs chosen as examples are 1200, 1300, 1400 and 1600 UT on March 18, 1978, and the AE indices at those times are 642, 934, 842, and 811 nT, respectively. The corresponding AL indices are -408, -613, -509 and -530 nT, respectively. From Figure I-9, one can see these epochs are quite disturbed.

The computer algorithm employed in this study is an improved version developed by Kamide et al. (1981). As they pointed out, the computed ionospheric currents and field-aligned currents do not seem to be very sensitive to the choice of the ionospheric conductivity model. However, the electric field obtained depends sensitively on the conductivity distribution. Therefore, a realistic conductivity model is essential for the determination of the Joule heat production rate as well as the electric potential distribution. Recently several conductivity models based on satellite particle measurements were published (Wallis and Budzinski, 1981; Spiro et al., 1982) and both models are expressed in terms of geomagnetic indices. However, the current systems in the polar ionosphere is highly variable and it is not sufficient to determine instantaneous current patterns only by a single geomagnetic index; for the same value of AE, the current pattern can be quite different.

For this reason, Ahn et al. (1982) developed a conductivity model which can reflect instantaneous conditions by knowing the general tendency that intense geomagnetic variations are associated with high

ionospheric currents and thus generally with a high conductivity. For details, see Chapter II.

The Pedersen conductivity distributions are shown in Figure IV-1. The Hall conductivity distributions are not shown here, since they have basically similar to the Pedersen conductivity distribution. Using the conductivity distribution thus obtained, one can calculate E and I_p distribution using the code of Kamide et al. (1981) over a network of points spaced 1° in latitude and 15° in longitude. Figure IV-2 shows the Pedersen current distribution at the four times. Since the Pedersen current flows along the direction of the electric field, one can have a rough idea of the direction of the electric field. From Figure IV-2, as well known, one can see that the direction of the electric field is generally northward in the evening sector and southward in the morning sector. Moreover, there is an indication that the electric field in the region from the late evening sector to the midnight sector has a westward component.

Using the distribution of I_p and E thus obtained, it is now possible to estimate the Joule heat production rate u_J at each grid point. Figure IV-3 shows the distribution pattern of u_J. It can be seen, first of all, that the main part of the enhanced zone of u_J in the evening sector is located always below the enhanced zone of conductivity. In other words, it is located just outside of the auroral oval. In the morning sector, however, the enhanced zone of u_J coincides more or less with the auroral oval. Second, the enhanced zones of u_J in both the evening and morning sectors are fairly uniform and the

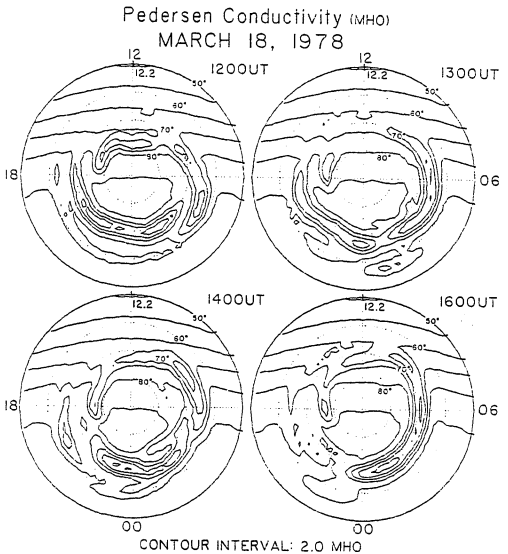

Figure IV-1 Isocontours of the global height-integrated Pedersen conductivity distributions constructed by the method developed by Ahn et al. (1982) for 1200, 1300, 1400 and 1600 UT on March 18, 1978. The numbers in each frame represent the maximum and minimum values. The lowest contour label is 2 mhos.

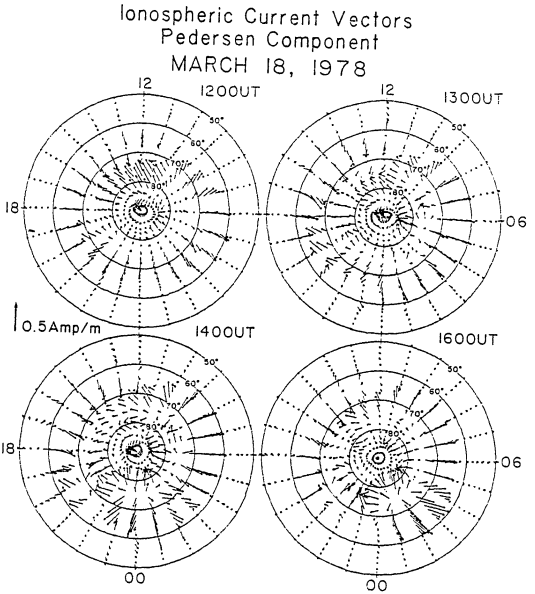

Figure IV-2 The distribution of the Pedersen current in magnetic latitude-MLT coordinates, for the same instants of Figure IV-1. The conductivity model used in this calculation was developed by Ahn et al. (1982).

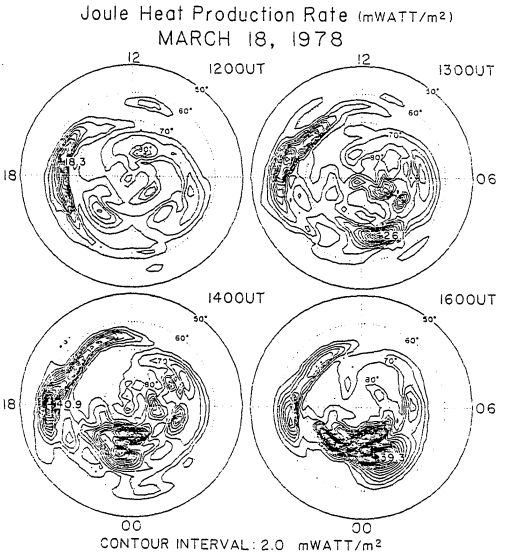

Figure IV-3 Isocontours of the Joule heat production rates based on the conductivity model developed by Ahn et al. (1982) for the same instants of Figure IV-1. The number in each frame represents the maximum energy production rate. The lowest contour label is 2 mwatt/m^2, where 1 mwatt/m^2 is corresponding to 1 erg/cm^{2}sec.

distribution of u_J particularly in the evening sector remains relatively stable during the disturbed period, while the enhanced zone in the midnight sector is highly variable and is localized.

It is worthwhile to compare the present results with other recent radar measurements of u_J. Banks et al. (1981) obtained the global pattern of u_J. One can notice from their results (their Figures 2, 3 and 5) that there exist stable enhanced zones of u_J in both the evening and morning sectors, particularly during summer months. Thus, their enhanced zones have similar characteristics to those we found in our results. One major difference from their results is the appearance of a high Joule heat production area in the midnight sector. This is partly due to the difference of the degree of disturbances we dealt with. Unfortunately, however, a quantitative comparison of the two results in terms of the magnitude of u_J is difficult, since they assumed a constant conductivity in estimating the distribution of u_J. Further, their distribution contains the dependence of substorm activity on UT, since their distributions were based on daily scan data, while ours are instantaneous distributions. By using eight days of synoptic data from the Chatanika incoherent scatter radar, Vickrey et al. (1982) obtained latitude-local time variations of u_J. From their result, for example, the April 6, 1977 event (their Figure 6) or the November 13, 1976 event (their Figure 11), one can get a rough idea of the magnitude of u_J. During the positive bay event ($\Delta H_{max} \sim 200$nT) of April 6, u_J is approximately 10 ~ 30 mwatt/m^2 and the negative bay event ($\Delta H_{max} \sim -800$nT) of the same day, u_J is greater than 30 mwatt/m^2. One

can see from our Figure IV-3 that the magnitudes of u_J are 41 mwatt/m^2 and 39 mwatt/m^2 in the positive and negative bay regions, respectively. The average AE index during the period (1200 UT-1600 UT on March 18, 1978) was 825 nT. Although the above comparison is only a 'spot-check', one can see that the present study provides values of u_J which are comparable to the past radar estimates. Most recently, Foster et al. (1983) made a statistical study of the Joule heat production in the polar region.

In order to obtain the global Joule heat production rate U_J, we divide the polar ionosphere into a large number of small cells and calculate u_J in each cell, by assuming that u_J is constant within each cell and represented by the value at the center of the cell. Then U_J is obtained as the sum of the product of u_J and the area of the corresponding cell. In this study, we divide the polar ionosphere into 960 cells, from the pole to 50° in latitude. Each cell is spaced 1° in latitude and 15° in longitude. From Figure IV-3, it is noticed that there is almost no contribution of Joule heat production below 50°.

The global Joule heat production rate U_J (one hemisphere) thus obtained for our chosen events in Figure IV-3 are 1.3×10^{11} watt; 2.0×10^{11} watt; 2.3×10^{11} watt and 2.1×10^{11} watt at 1200, 1300, 1400 and 1600 UT, respectively. Banks et al. (1981) estimated that the instantaneous power dissipation rate is about 10^{11} watt based on the electric field measurement by the Chatanika radar by assuming a constant height-integrated Pedersen conductivity. Bleuler et al. (1982) obtained the global Joule heat production as a function of the total field-

aligned current I_t; for $I_t \sim 6.0$ MA (which is equivalent to AE ~ 600 nT), they estimated the Joule heat production rate ~ 10^{11} watt during the equinoctial period.

Dividing the polar ionosphere into four 10° width concentric belts, we also compute the spatial partition of U_J. For example, at 1200 UT on March 18, 1978, the relative contribution of U_J are 10.8%, 31.2%, 49.5% and 8.5% for the zones bounded by 90°-80°, 80°-70°, 70°-60° and 60°-50°, respectively. At 1400 UT, they are 8.8%, 35.4%, 43.7% and 12.1% for the same zones.

From the above two estimates one can see that the most Joule heat dissipation occurs within the zone bounded by two latitude circles 80° and 60°. However, if the area of each belt is taken into account, the highest efficiency is found in the belt bounded by 80°-70°.

3. Auroral Particle Energy Injection Rate

In order to estimate the total energy consumption rate of the magnetosphere during magnetospheric substorms and storms, it is essential to obtain the auroral particle energy injection rate u_A and its integral U_A as a function of time. However, in order to obtain u_A at a point, one needs to know the energy spectrum, the pitch angle distribution and the differential flux of auroral particles involved; see Brekke (1976). Thus, it is very difficult to monitor this energy input rate continuously for an extended period.

Recently Wickwar et al. (1975) showed that the electron density profile measured by the Chatanika radar can be used to obtain the

height-integrated auroral particle energy injection rate u_A, by assuming that 35.5 eV are expended per electron-ion pair below 150 km (Rees, 1969). Since then several workers estimated the diurnal variation of u_A based on the 24 hour synoptic radar measurements (Banks, 1977; Murdin and Brekke, 1980; Vickrey et al., 1982). However, u_A obtained by the radar is far from instantaneous. An attempt was, therefore, made to deduce u_A by an indirect method.

It is quite reasonable to expect that there is a close relation between u_A and Σ_H, since most of the contribution for u_A comes from near the peak of the ionization profile, which is usually between 90 km and 130 km (Wickwar et al., 1975) and the main source of the height integrated Hall conductivity Σ_H is the electrons below 125 km (Brekke et al., 1974). On the basis of the above consideration, Ahn et al. (1982) derived an empirical relation between u_A and Σ_H based on the Chatanika radar measurements (Banks, 1977; Murdin and Brekke, 1980). For details, see Chapter II. The obtained relation is

$$u_A = 0.01 \ (\Sigma_H)^{2.0}$$

where the units of u_A and Σ_H are mwatt/m^2 and mho, respectively. They also derived empirical relations between Σ_H and the north-south component (ΔH) of magnetic disturbance field. Thus, it is possible to obtain the global distribution of u_A over the entire polar region using the ground-based magnetic data as the input on the basis of the following empirical relations:

$$u_A = \begin{cases} 0.046\ (\Delta H)^{0.71} & ;\ \Delta H>0 \\ 0.200\ (\Delta H)^{0.68} & ;\ \Delta H<0 \end{cases}$$

where the unit of ΔH is nT. From the above empirical relations, one can see that u_A is large in the region of negative ΔH variations.

In Figure IV-4 we show several examples of the u_A distribution for the same instants mentioned in the previous section. Two interesting features are evident from these examples. First, comparing with the Joule heat production rate u_J, the distribution pattern of u_A is well confined within a relatively narrow belt. The belt seems to be more or less a portion of the auroral oval. Second, as is expected from the above empirical relations, the strong enhancement of u_A is seen from the midnight to the morning sectors. The maximum values of u_A are 8.8 mwatt/m^2, 10.9 mwatt/m^2, 12.6 mwatt/m^2 and 13.5 mwatt/m^2 at the epochs of 1200, 1300, 1400 and 1600 UT on March 18, 1978, respectively.

Comparing the present results with other measurements, for example, those obtained by Vickrey et al. (1982), one finds that our estimate of u_A seems to be underestimated, since values above the range of 10-30 mwatt/m^2 are not uncommon in their results. One of the obvious reasons for this difference can be found from the fact that their estimation of u_A is based on the data averaged over 15 seconds, while ours is based on 30-min averaged data. Therefore the sharp peaks of u_A were tended to be smoothed out in our estimate. However, this underestimate of u_A does not seem to affect much on the estimation of the global input rate U_A. The reason can be found from the following consideration. From the scatter plots between u_A and the current density of electrojet

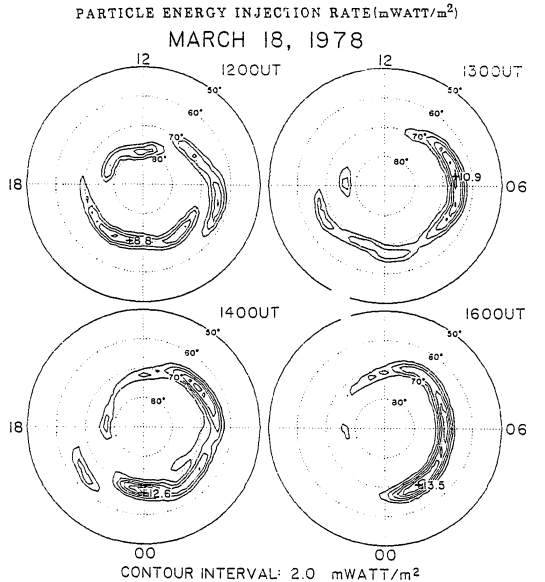

Figure IV-4 Isocontours of the particle energy injection rate based on the empirical relation developed by Ahn et al. (1982) for the same instants of Figure IV-1.

constructed by Vickrey et al. (their Figures 8 and 12), an empirical relation between the two quantities can be found readily in the zone of the westward electrojet as:

$$u_A \text{ (mwatt/m}^2\text{)} \sim 11.5 \times I_W \text{(A/m)}$$

where I_w is the current density of the westward electrojet. The relation in the eastward electrojet region is less prominent than in the westward electrojet region and could not be expressed by a simple form.

By comparing the ionospheric current distribution in Figure IV-5 with the distribution of u_A in Figure IV-4 one can find the region of the westward electrojet coincides well with the zone of the enhanced u_A. Further at 1600 UT, one can notice that the maximum current density (~1.5 A/m) region around 0200 MLT coincides with the maximum zone of u_A. Since the current density is known, u_A can be estimated using on the empirical relation obtainable from the results of Vickrey et al. (1982). The quantity u_A thus obtained at the maximum enhanced region is ~16.5 mwatt/m^2. This is comparable with our estimate ~13.5 mwatt/m^2 at the same region.

The global particle energy injection rate U_A can be obtained using the same network of grid as that for U_J. U_A (one hemisphere) thus obtained from the pole to 50° in latitude are 0.42×10^{11} watt, 0.39×10^{11} watt, 0.51×10^{11} watt and 0.45×10^{11} watt at 1200, 1300, 1400 and 1600 UT, respectively.

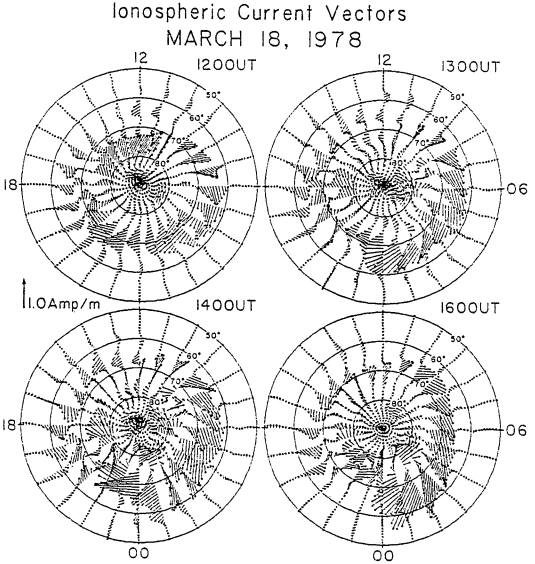

Figure IV-5 Distribution of calculated ionospheric current vectors based on the computer code developed by Kamide et al. (1981) for the same instants of Figure IV-1.

The spatial partition of U_A in the concentric belts defined in the previous section is also estimated. For example, at 1200 UT, it is found that the relative contribution of U_A are 1.8%, 46.8%, 50.6% and 0.8% for the zones bounded by 90°-80°, 80°-70°, 70°-60° and 60°-50°, respectively. At 1300 UT, the corresponding figures are 0.2%, 23.3%, 75.1% and 1.4%. For the purpose of comparison, we select a quiet period, not shown in Figure IV-4 they are 1.4%, 60.0%, 35.1% and 3.5% for the same zones. The three examples of u_A distribution show clearly that the enhanced zones of u_A shift northward as the magnetic activity decreases. Although the same type of behavior can be noted in the distribution of the Joule heat production rate u_J, the contraction and expansion of the enhanced zones of u_A in terms of magnetic activity is more prominent than that of u_J.

4. Total Ionospheric Energy Dissipation Rate

We define the total ionospheric energy dissipation rate u_I simply as the sum of the Joule heat production rate u_J and the auroral particle energy injection rate u_A. Similarly the total ionospheric energy deposition rate U_I is defined as the sum of U_J and U_A. However, we neglect the energy input by the plasma heat conduction from the magnetosphere into the ionosphere, since it is small in comparison with u_J and u_A, seldom being as large as 0.2 mwatt/m^2 in a stable auroral red arc (Rees, 1975). Another source due to the plasma wave heating is also neglected, since it is not well known yet, nor has the implication of the heat source to U_I established (Banks, 1980).

Before discussing the characteristics of U_I distribution, it is worthwhile to examine the relative ratio of U_J to U_A to get some idea about the relative contribution of U_J and U_A to U_I. The ratios thus obtained are shown in Figure IV-6 in terms of geomagnetic index AL. Each circle in the figure represents the ratio at each epoch which is chosen every hour from three day data mentioned in the previous sections. In spite of some scatter, there is a tendency that the ratio U_J/U_A does not change very much as the magnetic activity increases, although u_J/u_A are expected to vary at different locations and different times. Further, the scatter of data point is quite uniform and all data points are distributed within the range of 2 to 7.

The average value of the ratio obtained from the whole period is about 4.0. This means that the main contribution to the total ionospheric energy consumption comes from the Joule dissipation. This result seems to be inconsistent with the recent Chatanika radar measurement. According to Banks (1977) and Vickrey et al. (1982), the energy input by particle and Joule heating is generally comparable in magnitude. Although our estimation of U_A is slightly underestimated as mentioned in section 3, one may find more fundamental reasons why such a discrepancy is possible from the following consideration.

First of all, the Chatanika radar could cover only a limited portion of the polar ionosphere, including the vicinity of the auroral oval and oval itself. Thus, the conclusion based on this measurement could not be applicable over the entire polar ionosphere. As mentioned in sections 2 and 3, U_A is highly concentrated within the auroral oval,

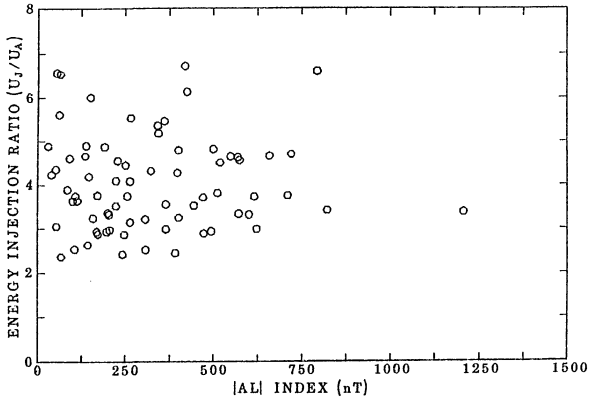

Figure IV-6 Scatter plot of energy injection ratio, U_J/U_A as a function of geomagnetic index AL(71).

whereas U_J is distributed over relatively wide region including the auroral oval. Therefore if one deals with the energy dissipation problem, using the results obtained only within a narrow zone, for example including the auroral oval and its near vicinity, the conclusion might be similar to the one obtained by the radar measurement. During the disturbed period shown in Figure IV-4 one can notice that the enhanced zone of u_A coincides well with the zone which the radar could cover, say ~62°-68°. Thus U_A seems to be quite comparable with U_J, as far as the narrow zone is concerned.

The distribution pattern of u_I is similar to that of u_J, except that the morning side auroral zone is slightly more enhanced compared to the rest of it, due to the particle energy injection. Thus, as can be seen in Figure IV-7, u_I in both morning and evening side are more or less balanced in terms of the magnitude.

5. The Empirical Relations Between the Energy Deposition Rates and the Geomagnetic Indices

It is highly desirable to derive empirical relations between the energy deposition rates in the ionosphere and the geomagnetic indices in studying the energy coupling between the solar wind and the magnetosphere. For this purpose, we use 72 hourly values on the three days, March 17, 18 and 19, 1978. The empirical relations obtained in this section are based on the improved geomagnetic index AL(71); see Kamide et al. (1982a) for the new geomagnetic indices. Figure IV-8 shows time variations of U_J and U_A and of the two geomagnetic indices.

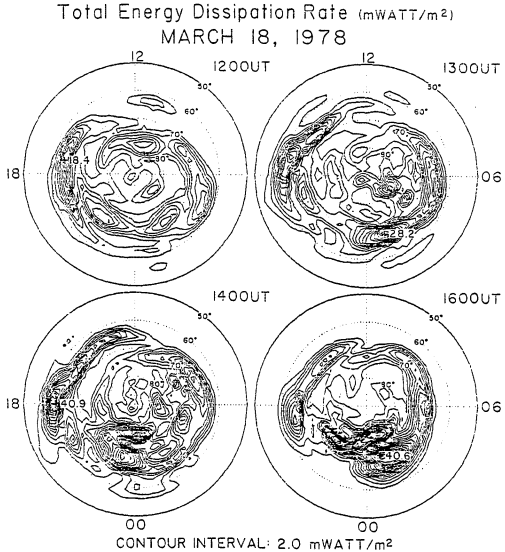

Figure IV-7 Isocontours of the total ionospheric energy dissipation rates for the same instants of Figure IV-1.

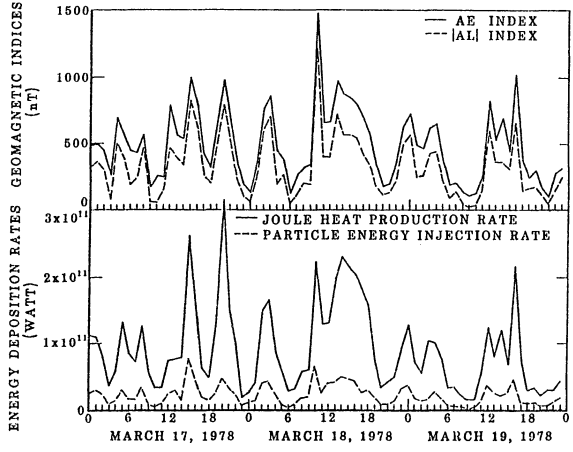

Figure IV-8 Upper panel shows the variation of geomagnetic indices AE(71) and AL(71) during March 17, 18 and 19, 1978. Lower panel shows U_J and U_A variations during the same period. Both panels are constructed by 72 instants taken every hour from the three days.

One can see that an intensification of magnetic activity always accompanies an enhancement of U_J and U_A. Further, one can notice that, as mentioned in Section 4, the ratio U_J/U_A is almost constant.

Figures IV-9a, IV-9b and IV-9c show the scatter diagrams of AL-U_J, AL-U_A and AL - U_I, respectively. From these diagrams, linear relations between AL index and the energy deposition rates can be deduced. (Although they are not shown here, the scatter diagrams of AE - U_J, AE - U_A and AE - U_I are also constructed. The results are very similar to Figures IV-9a, IV-9b and IV-9c, respectively.) In Table IV-1, the empirical relations are listed.

It is worth comparing the empirical relations with similar empirical relations obtained by others. Several attempts have been made to relate the magnetic perturbation vector (ΔH) and the overhead Joule heat production rate by a theoretical study (Cole, 1971) and observational data obtained from the Chatanika radar (Brekke and Rino, 1978; Murdin and Brekke, 1980). Murdin and Brekke (1980) expanded their empirical relations to include the average particle energy injection rate. However, the global Joule energy input rate has not been studied extensively in terms of magnetic activity indices.

Recently, Akasofu (1981) proposed simple linear relationships between the energy deposition rates U_J, U_A and AE index. According to Akasofu (1981), U_J (one hemisphere) is 0.45×10^{11} watt at AE = 450 nT. More recently, Nisbet (1982) derived theoretical relationships between the field-aligned currents, the geomagnetic indices and the

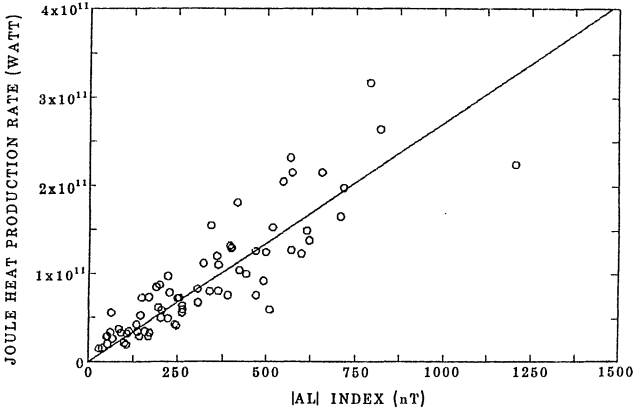

Figure IV-9(a) Scatter plots of U_J versus AL(71). Since AL has negative value, the absolute value notation is used in x-axis. Each data point is corresponding to an instant in Figure IV-8. Note U_A versus AL plot has a different scale with others in y-axis.

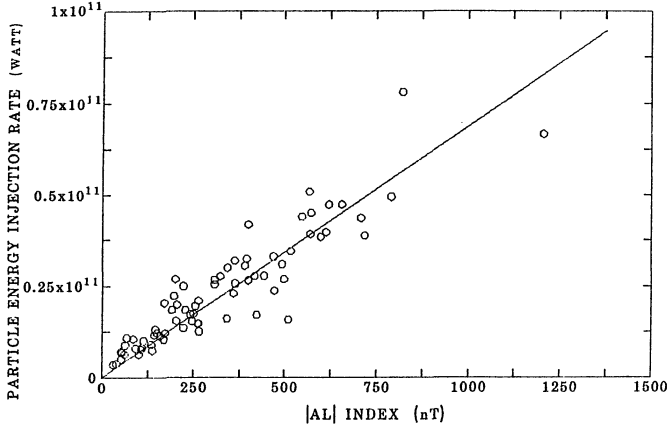

Figure IV-9(b) Same as IV-9(a) for U_A versus AL(71).

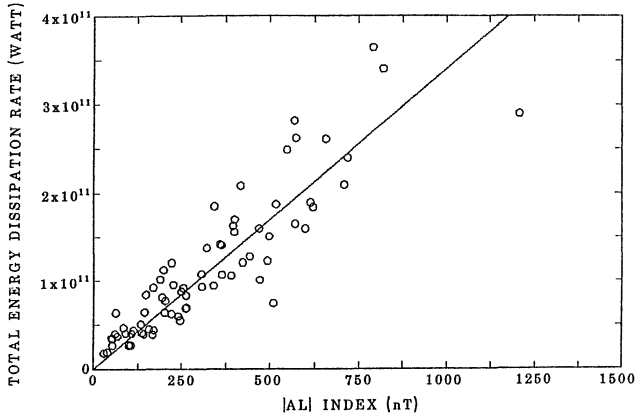

Figure IV-9(c) Same as IV-9(a) for U_I versus AL(71).

Table IV-1

Empirical relations between the energy deposition rates (one hemisphere) and the geomagnetic indices AL and AE. The units of energy deposition rates and geomagnetic indices are watt and nT, respectively. The number inside parentheses represent the number of magnetic stations used in generating the corresponding geomagnetic indices. 12 represents the standard indices, see Kamei and Maeda (1981).

	U_A	U_J	U_I
AL(12)	0.8×10^8(AL)	3.0×10^8(AL)	3.8×10^8(AL)
AL(71)	0.7×10^8(AL)	2.7×10^8(AL)	3.4×10^8(AL)
AE(12)	0.6×10^8(AE)	2.3×10^8(AE)	2.9×10^8(AE)
AE(71)	0.5×10^8(AE)	1.9×10^8(AE)	2.4×10^8(AE)

Joule heat production rate using a simplified model of the auroral ionosphere, the field-aligned currents, and the auroral electrojets. Since he expressed U_J in terms of both AL and AU indices and sorted the relations again in season, it is not easy to compare his results directly with ours. As an example, Nisbet (1982) shows U_J is 0.37 x 10^{11} watt at AE = 450 nT in equinoctial season. Our estimation of U_J is 1.04 x 10^{11} watt at the same magnitude of magnetic activity. Thus, our estimation of U_J is quite comparable with other presently available results in terms of magnitude. A rough estimate of U_J by Banks et al. (1981) is ~ 10^{11} watt.

Several U_A estimations have been made from the observational data (Hargreaves, 1966; Sharp and Johnson, 1968). Recently Wallis and Budzinski (1981) and Spiro et al. (1982) estimated U_A based on the satellite particle measurements in terms of geomagnetic indices K_p and AE, respectively. According to Wallis and Budzinski (1981), the estimated average U_A during moderately disturbed period, mean $K_p \sim 4_o$, is found about 0.12 x 10^{11} watt. It is hard to make a direct comparison to this result with that of Spiro et al. (1982), since one cannot convert K_p index into AE index easily. However, one can get some idea about the magnitude of U_A from the formula by Spiro et al. (1982), U_A = (0.875 x AE + 80) x 10^8 watt. For example, at AE = 450 nT, U_A is 0.47 x 10^{11} watt. U_A obtained from the formula proposed by Akasofu (1981) is 0.23 x 10^{11} watt at the same magnitude of magnetic activity. Our estimation of U_A based on AE(12) formula from Table IV-1 is 0.24 x 10^{11} watt.

CHAPTER V. CONCLUSIONS AND DISCUSSIONS

1. Ionospheric Conductivities

We believe that the present method of constructing the conductivity model satisfies, at least for the time being, the need for instantaneous distributions of the conductivities (Σ_P, Σ_H) which are required in analyzing magnetic field data by the computer code developed by Kamide et al. (1981). The empirical formulae obtained in this study can be supported by some of the recent studies of the conductivity and electric fields. For example, there are growing evidences that within the region of the westward electrojet, current enhancements in the ionosphere are produced primarily by increased conductivities, rather than an increased electric field (Foster et al., 1981). On the other hand, the northward electric field is the main contributor to the eastward electrojet in the evening sector (Kamide and Vickrey, 1982). The present statistical results are compatible with such observations. For all these reasons, it is hoped that the present method of constructing instantaneous conductivity models will be useful until an improved method will eventually be found.

Needless to say that future incoherent scatter radar data from Greenland will improve the expression for the weighting function. More data are also needed to improve the empirical relations for the positive events in the evening sector. Another major limitation of the present model comes from the lack of actual conductivity measurements in the polar cap and subauroral area.

It should be mentioned that the present empirical relation tends to yield higher values of conductivity values than the other two models (Wallis and Budzinski, 1981; Spiro et al., 1982). Their estimates are based on precipitating electron fluxes measured by satellites, while the present model is based on the observed electron density profiles observed from the earth's surface. Thus, the present estimates are based on more direct measurements than theirs, although their geographic coverage is much greater. It should be mentioned, however, that in their new calculations of the conductivities, Vickrey et al. (1981) used a different collision frequency coefficient which is one-half of the value given by Banks and Kockarts (1973). This is to take into account the reduced mass in transforming from the center-of-mass system to the laboratory system (cf. Rees and Walker, 1968; Stubbe, 1968). Through this new calculation of conductivities, it was indicated that the previous results which were used in this analysis were over-estimated by such amount. On the other hand, the new conductivity estimated by Vickrey et al. (1981) is still higher than the satellite estimates. Indeed, their Hall and Pedersen conductivities can often reach values exceeding 50 mhos and 25 mhos, respectively (the corresponding AE index ~800 nT), although such high values occur seldom in the satellite estimates. For the reasons given earlier, it is hoped that the satellite estimates will be improved by incoherent scatter radar data.

2. The Characteristics of Ionospheric Current Distributions During Substorms

(a) Summary of the results

We have combined the most comprehensive ground-based magnetic field data set ever obtained and the computer algorithm developed by Kamide et al. (1981) which can determine fairly accurately the three-dimensional polar current system. Further, we employed the conductivity model developed recently by Ahn et al. (1982). Although only 48 examples are shown in this paper, actually we have examined the ionospheric current distributions of almost every 5 minute data, totaling 864 events. In Chapter III, the growth and decay of the total ionospheric currents for a number of substorms were examined. In spite of the complexities of the individual events, it is possible to extract common features in the current distribution pattern during each phase of the magnetospheric substorms. Several interesting characteristics of each phase are summarized as follows:

(i) Quiet Time

During a quiet period only noticeable current flows are found in the polar cap and dayside cusp regions. Although the current pattern in the polar cap region are very complicated, some common features can be found. The current pattern consists of several current vortices. As mentioned earlier, such a pattern seems to be closely related with the four-cell convection pattern in the polar cap region during the period of IMF $B_z > 0$. Their orientation with respect to the noon-midnight meridian seem to be

variable. However, it is not clear whether there is any systematic variation in current pattern during quiet periods. On the other hand, although the current flows are weak, one can see that the east-west component is dominant in the auroral zone in the night sector (e.g., 0830 UT on March 19 in Figure III-10). Just before the 'development phase', there is a brief period during which an eastward electrojet is dominant in the entire morning sector auroral zone. See the examples of current patterns at 0550 UT in Figure III-6 and at 0900 UT in Figure III-10. The period seems to be related with the positive B_z component before the southward turning of the IMF. It is interesting to mention that according to Maezawa (1976) there is a reversed convection pattern during the period of the IMF $B_z > 0$.

(ii) 'Development phase'

The 'development phase' may be introduced to designate the time interval from the time of the appearance of a noticeable auroral electrojet system in the nightside auroral zone to the onset of the expansion phase. Since a well-developed westward electrojet is prominent even during an early epoch of the 'development phase', the substorm activity seems to start before the onset of the expansion phase. Further it is important to note

that there is no definite difference between the current patterns of the 'development phase' and expansion phase. During the 'development phase's examined in the previous section, no appreciable cosmic radio noise absorption were recorded. Thus, there is a possibility that the global electric field intensity is enhanced during such a period. Two examples, of 'development phase' examined in this study lasted respectively about 40 minutes and 50 minutes. However, 'the development phase' is different from the so-called 'growth phase' which has been identified by a slow growth of the AE index. As mentioned in (iii), the growth phase is a misidentification of a weak substorm prior to the major one (WPM).

It is hard to identify the 'development phase' of a substorm using the AE index, since the current is too weak, ~0.1 A/m, to manifest itself in the AE index or it is below the 'noise' level of the AE index; here, 'noise' refers to dayside cusp activity. Thus, even with the improved AE(71) index, it is hard to monitor the auroral electrojets properly during such a period of low magnetic activity, say below 200 nT.

Actually, the standard AE(12) index monitors the auroral electrojets better than the AE(71) index during the period when the dayside cusp region has a strong current flow compared to that in the auroral zone. Such a situation happens quite often, for example, just before the expansion phase.

(iii) DP 2 current and growth phase

It has long been suggested that prior to the expansion phase there occurs the DP 2 current distribution. However, this study does not confirm the presence of such a current system as far as the total ionospheric current distribution is concerned. Instead there is a current system, which is basically the same as the one during the expansion phase.

On the other hand, the equivalent current distribution does not show any definite signature of the so-called two cell convection pattern. It is only after the onset of the expansion phase that such a pattern, DP 2 current is prominent in the equivalent current system.

(iv) First substorm after a prolonged quiet period

It is interesting to examine the substorms which occur after a prolonged quiet period, although the data set used in this study does not contain many such examples. In our examples, these events start with a weak substorm and are then followed immediately by a much more intense one. Such an initial weak activity has been identified as a signature of growth phase by some workers. However, the auroral photographs during such a period show clearly that a weak substorm is in progress. A good example of such a period is found at about 1000 - 1100 UT on March 19 in Figure III-2. Such a substorm activity may be called as a WPM type.

(v) Substorm onset

A sharp intensification of negative ΔH disturbance and the AE index has been emphasized as a signature of the onset of the expansion phase (e.g. McPherron, 1970; Kokubun, 1971; Kokubun and Iijima, 1975). Noting the AE index at about 1140 UT on March 19 in Figure III-2 and the corresponding current distribution, however, it is clear that the most contribution to the sharp increase of the AE index comes from the stations only in the late evening and midnight sectors. There is no abrupt change of the global scale in the current distribution and intensity during the period of sharp increase in the AE index. Thus, as already reported by several workers, the so-called 'sharp onset' is only a local (evening or midnight) feature and has no major significance in the terms of the global current system. Further AE index and Fm (Kamide et al., 1982b) are not proportional to the overall current intensity during such a period.

(vi) Expansion phase

During the expansion phase, the belts of the auroral electrojets are slightly shifted southward. Particularly, such a shift is prominent in the dawn and dusk sectors. The enhancement of the eastward electrojet occurs mostly during the early epoch of the expansion phase and its intensity almost reaches its maximum value before the maximum phase of the substorm which is determined from the AE index.

On the other hand, the intensity of the westward electrojet steadily increases during the entire expansion phase. Moreover, the westward electrojet intrudes deeply into the evening sector along the poleward boundary fo the eastward electrojet. The maximum current density of the westward electrojet is found in the late evening or midnight sector.

It is worthwhile to mention that the current intensity in the polar cap region does not show any noticeable enhancement during the expansion phase. Simultaneously, the relatively strong current flows in the dayside cusp region shift equatorward and gradually decays.

(vii) Recovery phase

During the recovery phase the overall current intensity decreases and the center of maximum current density in the westward electrojet shifts toward the early morning sector (e.g., Kamide, 1982). The intruded part of the westward electrojet decays. Simultaneoulsy, the whole auroral electrojet system retreats poleward. On the other hand, the WPM type substorm does not show any poleward shift of the auroral electrojets during its recovery phase. However, it is not clear whether the recovery phase of a WPM type substorm is superposed on the development or expansion phase of the subsequent major substorm.

(viii) New substorm soon after the recovery phase of previous substorm

It does not seem that the whole auroral electrojets, once retreating poleward during the recovery phase, re-expand during the subsequent substorm unless a new substorm is followed immediately by the old one. Instead of re-expansion, it seems that a new electrojet system gradually emerges from the auroral zone of the nightside sector after a period of confusion in the current distribution pattern.

(ix) Effects of the IMF B_y component

Through this study, it is also found that there exists two types of current systems. The characteristics of the two current patterns are prominent particularly during the expansion phase. Further, the 'type A' and 'type B' are morphologically almost identical with those which were obtained from the averaged meridian chain data during the periods of negative and positive IMF B_y components, respectively. Unfortunately, the definite relation between the current types and the IMF B_y polarity has not been fully confirmed in this study. But, one must take into account that the following two limitations were imposed in this work. First, during the period examined in this study, the time span of positive B_y period was not enough to examine fully the 'type B'. Second, there was no exact information about the time delay of the ionospheric response to the IMF change.

(b) Schematic representation of current system

Here, the development of the substorm current system is schamatically represented during each phase of substorm. In Figure V-1, each type of current patter is shown separately for both the A and B types by summarizing the results mentioned in the above. It is extremely difficult to select an ideal current pattern of each phase and of each type from the limited data set. Further, due to the different degree of magnetic activity, considerable improvements are needed in the locations and thickness of current belts.

An important purpose of the figure is to show that there is a distinct difference in the relative location of the eastward and westward currents, particularly during expansion and maximum phases for the two types.

3. The Energy Dissipations in the Polar Ionosphere

In studying the energy coupling between the solar wind and the magnetosphere, it is crucial to be able to estimate the global energy input rate as a function of time. Recently, radars and satellites provide invaluable data for the Joule and particle heating rate estimates. However, due to the limited spatial and temperal resolution of the measurements, it is not possible to obtain instantaneously the distributions of u_J and u_A over the entire polar region. It is thus not possible to obtain U_J and U_A. In spite of such limitations, the Chatanika radar provided a unique opportunity in determining the empirical relationships between the conductivity, particle energy

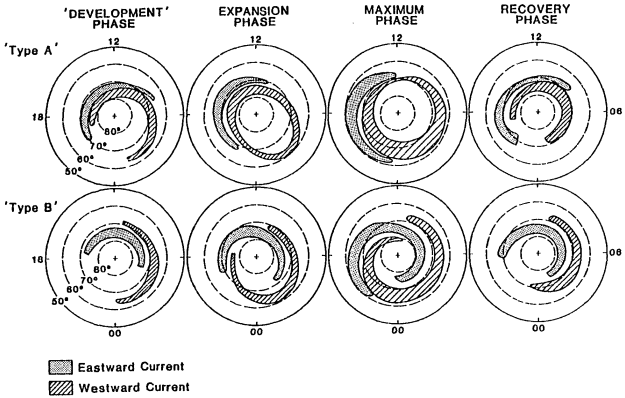

Figure V-1 Schematic representations of the ionospheric current distribution during each phase of substorm. The 'type A' and 'type B' patterns are shown separately.

injection rate and ground magnetic perturbations. Therefore, although crude, it is now possible to construct a global conductivity distribution and a global particle energy injection rate distribution at a particular instant, if the instantaneous ground magnetic perturbation data of the entire polar region can be provided. With such data set and the conductivity model developed by Ahn et al. (1982), one can estimate the global Joule heat production rate associated with the numerical scheme introduced by Kamide et al. (1981).

It may be appropriate to discuss here the accuracy of our estimate of the Joule heat production rate, since several simplifying assumptions have been used in the present thesis. Possibly errors emerge mainly from the following steps: (i) determining the empirical relationship of the height-integrated conductivities to ground-based magnetic variations ΔH at ~65°, (ii) constructing the weighting function to determine the conductivities in the polar-cap and sub-auroral altitudes, (iii) calculating the global distribution of the electric field.

The standard deviations in determining the conductivities as function of ΔH are about 9.0 mhos for Σ_H and about 5.4 mhos for Σ_P. These statistical deviations include the effects of neglecting the local time dependence of the empirical formulas. The weighting function is perhaps correct with accuracy of less than 50%, depending on the unknown latitudinal width of the auroral oval. The accuracy of the calculation of the global electric field is better than 5%, but the above errors in the estimation of Σ can significantly affect the final electric field, and thus the Joule heat production rate. However, according to an

'experiment' by Kamide and Richmond (1982), even a change of 100% in the conductivities (from 10 mhos to 20 mhos in the maximum region of Σ_H, and from 5 mhos to 10 mhos in the maximum region of Σ_P at auroral latitudes) causes a 20% change in the electric field strength. Since the Joule heat production rate is given by $\Sigma_P E^2 = I_P E$ (where I_P denotes the Pedersen current strength) and since our numerical estimate of the ionospheric currents is not very sensitive to the estimate of the conductivities (Kamide et al., 1982), the errors involved in the Joule heat production rate are expected to be almost the same order of magnitude as those of the electric field.

We have shown that the Joule heat production rate and particle energy injection rate thus obtained are comparable with the estimates made by the radar and the theoretical studies in terms of the general distribution patterns and the magnitudes, and have established the empirical relations between the global energy input rates and the geomagnetic indices, AE and AL. Several interesting conclusions are summarized as follows:

(i) The enhanced zone of u_A is well defined within the auroral oval and the location is very sensitive to the degree of magnetic activity. This tendency may be contrasted with that of the u_J distribution.

(ii) The enhanced zone of u_A is located near the northern edge of the enhanced zone of u_J in the evening sector, but in the morning sector the two zones are more or less overlapped.

(iii) The magnitudes of U_A and U_J in the auroral zone are comparable but the total ionospheric energy deposition rate U_I is dominated by the U_J by a factor of 4.0.

(iv) The ratio U_J/U_A does not seem to be affected by magnetic activity.

(v) From the scatter diagrams between the global energy deposition rates and the geomagnetic indices, one can conclude that the geomagnetic indices AE and particularly AL can be used as good monitors of the global energy deposition rates.

Effects upon the upper thermosphere due to the energy input U_J or U_A are beyond the scope of this thesis. However, our finding that U_J is the dominant energy source in the polar ionosphere has an important implication to the problem of thermospheric responses, since Banks (1977) suggested that the Joule heat production has a much more rapid effect upon the upper thermosphere than the particle energy injection.

Our method relies on various empirical relationships, it is important to calibrate U_J and U_A by other methods. Unfortunately, there is, at present, no other method to estimate such global quantities on an instantaneous basis. In the future, we plan to examine all the quantities for more and less disturbed periods as well.

Finally, it is suggested that the nearly constant ratio of U_J/U_A provides an important clue in understanding the solar wind-magnetosphere energy coupling problem. The constant ratio can be interpreted as the magnetosphere responding in such a fashion that the electric field

enhancement and the particle precipitation rate increase in harmony, as magnetic activity increases.

References

Ahn, B.-H., S.-I. Akasofu, and Y. Kamide, The Joule heat production rate and the particle energy injection rate as a function of the geomagnetic indices AE and AL, J. Geophys. Res., submitted, 1982.

Ahn, B.-H., R. M. Robinson, Y. Kamide, and S.-I. Akasofu, Electric conductivities, electric fields and auroral particle energy injection rate in the auroral ionosphere and their empirical relations to the horizontal magnetic disturbances, in press, Planet. Space Sci., 1982.

Akasofu, S.-I., Electrodynamics of the magnetosphere: Geomagnetic storms, Space Sci. Rev., 6, 21, 1966.

Akasofu, S.-I., Polar and magnetospheric substorms, Chap. 4, D. Reidel Publ. Co., Dordrecht-Holland, 1968.

Akasofu, S.-I., Physics of Magnetospheric Substorms, D. Reidel Publ. Co., Dordrecht-Holland, 1977.

Akasofu, S.-I., Energy coupling between the solar wind and the magnetosphere, Space Sci. Rev., 28, 121, 1981.

Akasofu, S.-I., and B. H. Ahn, Distribution of the field-aligned currents, ionospheric currents, and electric field in the polar region on a very quiet day and a moderately disturbed day, J. Geophys. Res., 86, 753, 1981.

Akasofu, S.-I., B.-H. Ahn, Y. Kamide, and J. H. Allen, A note on the accuracy of the auroral electrojet indices, J. Geophys. Res., submitted, 1983.

Akasofu, S.-I., B.-H. Ahn, and G. J. Romick, A study of the polar current systems using the IMS meridian chains of magnetometers: I. Alaska Meridian Chain, preprint, 1983.

Akasofu, S.-I. and S. Chapman, Magnetic storms: Their geometrical and physical analysis, and their classifications, pp. 40, 12. Particular magnetic storms, Studia. Geoph. et Geod. 5, 1961.

Akasofu, S.-I., S. Chapman, and C.-I. Meng, The polar electrojet, J. Atmos. Terr. Phys., 30, 227, 1965.

Akasofu, S.-I., Y. Kamide, and J. Kisabeth, Comparison of two modeling methods for three-dimensional current systems, J. Geophys. Res., 86, 3389, 1981.

Akasofu, S.-I., J. Kisabeth, G. J. Romick, H. W. Kroehl, and B.-H. Ahn, Day-to-day and average magnetic variations along the IMS Alaska Meridian chain of observatories and modeling of a three-dimensional current system, J. Geophys. Res., 85, 2065, 1980a.

Akasofu, S.-I., and C.-I. Meng, A study of polar magnetic substorms, J. Geophys. Res., 74, 293, 1969.

Akasofu, S.-I., and M. Roederer, Polar cap arcs and the open regions, Planet. Space Sci., in press, 1983.

Akasofu, S.-I., G. J. Romick, and H. W. Kroehl, The IMF B_y effects observed by the IMS Alaska meridian chain, J. Geophys. Res., 85, A5, 2079, 1980b.

Armstrong, J. C., and A. J. Zmuda, Field-aligned current at 1100 km in the auroral region measured by satellite, J. Geophys. Res., 75, 7122, 1970.

Armstrong, J. C., and A. J. Zmuda, Triaxial magnetic measurements of field-aligned currents at 800 kilometers in the auroral region: Initial results, J. Geophys. Res., 78, 6802, 1973.

Banks, P. M., Observations of joule and particle heating in the auroral zone, J. Atmos. Terr. Phys., 39, 179, 1977.

Banks, P. M., Energy sources of the high latitude upper atmosphere, C. S. Deehr and J. A. Holtet (eds.), Exploration of the Polar Upper Atmosphere, 113-127, D. Reidel Publ. Co., 1980.

Banks, P. M., and J. R. Doupnik, A review of auroral zone electrodynamics deduced from incoherent scatter radar observations, J. Atmos. Terr. Phys., 37, 951, 1975.

Banks, P. M., J. C. Foster, and J. R. Doupnik, Chatanika radar observations relating to the latitudinal and local time variations of joule heating, J. Geophys. Res., 86, 6869, 1981.

Banks, P. M., and G. Kockarts, Aeronomy, Part A, Academic Press, New York, 1973.

Baron, M. J., and N. J. Chang, ICECAP, '73a-Chatanika radar results HAES Report No. 15, Stanford Research Institute, Menlo Park, California, 1975.

Baumjohann, W., R. J. Pellinen, H. J. Opgenoorth, and E. Nielsen, Joint two-dimensional observations of ground magnetic and ionospheric electric fields associated with auroral zone currents, 4. Current systems associated with local auroral breakups, Planet. Space Sci., 29, 431, 1981.

Berkey, F. T., L. L. Cogger, S. Ismail, and Y. Kamide, Evidence for a correlation between sun-aligned arcs and interplanetary magnetic field direction, Geophys. Res. Lett., 3, 145, 1976.

Birkeland, K., The Norwegian Aurora Polaris Expedition 1902-1903, Vol. 1, 1st sec., Aschhoug, Christiania, 1908.

Birkeland, K., The Norwegian Aurora Polaris Expedition 1902-1903, Vol. 1, 2nd sec., Aschhoug, Christiania, 1913.

Bleuler, C., C. H. Li, and J. S. Nisbet, Relationships between Birkeland currents, ionospheric currents and electric field, J. Geophys. Res., 87, 757, 1982.

Bonnevier, B., R. Boström, and G. Rostoker, A three-dimensional model current system for polar magnetic substorms, J. Geophys. Res., 75, 107, 1970.

Boström, R., A model of the auroral electrojets, J. Geophys. Res., 69, 4982, 1964.

Boström, R., Currents in the ionosphere and magnetosphere, Ann. Geophys., 24, 681, 1968.

Boström, R., Polar magnetic substorms, in The Radiating Atmosphere, ed. by B. M. McCormac, p. 357, D. Reidel, Dordrecht-Netherlands, 1971.

Brekke, A., Electric fields, joule and particle heating in the high latitude thermosphere, J. Atmos. Terr. Phys., 38, 887, 1976.

Brekke, A., J. R. Doupnik, and P. M. Banks, Incoherent scatter measurements of E region conductivities and currents in the auroral zone, J. Geophys. Res., 79, 3773, 1974.

Brekke, A., and C. L. Rino, High-resolution altitude profiles of the auroral zone energy dissipation due to ionospheric currents, J. Geophys. Res., 83, 2517, 1978.

Burke, W. J., M. S. Gussenhoven, M. C. Kelly, D. A. Hardy, and F. J. Rich, Electric and magnetic field characteristics of discrete arcs in the polar cap, J. Geophys. Res., 87, 2431, 1982.

Burke, W. J., M. C. Kelley, R. C. Sagalyn, M. Smiddy, and S. T. Lai, Polar cap electric field structure with northward IMF, Geophys. Res. Lett., 6, 21, 1979.

Chapman, S., The electric current systems of magnetic storms, Terr. Magn. Atmos. Elec., 40, 349, 1935.

Chapman, S., and J. Bartels, Geomagnetism, Clarendon, Oxford, 1940.

Cole, K. D., Eccentric dipole coordinates, Austral. J. Phys., 16, 423, 1963.

Cole, K. D., Magnetic storms and associated phenomena, Space Sci. Rev., 5, 699, 1966.

Cole, K. D., Electrodynamics heating and movement of the thermosphere, Planet. Space Sci., 19, 59, 1971.

Doupnik, J. R., A. Brekke, and P. M. Banks, Incoherent scatter radar observations during three sudden commencements and a Pc5 event on August 4, 1972, J. Geophys. Res., 82, 499, 1977.

Eather, R. H., and S.-I. Akasofu, Characteristics of polar cap auroras, J. Geophys. Res., 74, 4794, 1969.

Feldstein, Y., Polar geomagnetic disturbances, Space Sci. Res., 8, 266, 1968.

Feldstein, Y. I., Polar auroras, polar substorms, and their relationships with the dynamics of the magnetosphere, Rev. Geophys., 7, 179, 1969.

Feldstein, Y. I., Magnetic field variations in the polar region during magnetically quiet periods and interplanetary magnetic fields, Space Sci. Rev., 18, 777, 1976.

Feldstein, Y. I., and G. U. Starkov, Dynamics of auroral belt and polar geomagnetic disturbances, Planet. Space Sci., 15, 209, 1967.

Feldstein, Y. I., and A. N. Zaitzev, Variation of the magnetic field in high latitudes on calm days of the IGY summer, Geomagn. Aeron. Engl. Transl., 7, 160, 1967.

Foster, J. C., J. R. Doupnik, and G. S. Stiles, Large scale patterns of auroral ionospheric convection observed with the Chatanika radar, J. Geophys. Res., 86, 11357, 1981.

Foster, J. C., J. P. St.-Maurice, and V. J. Abren, Joule heating at high latitudes, J. Geophys. Res., submitted, 1983.

Friis-Christensen, E., Y. Kamide, A. D. Richmond, and S. Matsushita, IMF control of high latitude electric fields, ionospheric and Birkeland currents determined from Greenland magnetometer data, preprint, 1982.

Friis-Christensen, E., and J. Wilhjelm, Polar cap currents for different directions of the interplanetary magnetic field in the Y-Z plane, J. Geophys. Res., 80, 1248, 1975.

Fukushima, N., Polar magnetic storms and geomagnetic bays, J. Fac. Sci. Tokyo Univ., 8, 293, 1953.

Fukushima, N., Spatial extent of the return current of the auroral-zone electrojet, 1. Ionos. Space Res. Jap., 23, 209, 1969.

Fukushima, N., and Y. Kamide, Partial ring current models for worldwide geomagnetic disturbances, Rev. Geophys. Space Phys., 11, 795, 1973.

Greenwald, R. A., Electric fields in the ionosphere and magnetosphere, presented at the Fifth International Symposium on Solar-Terrestrial Physics, Ottawa, Canada, 1982.

Hargreaves, J. K., On the variation of auroral radio absorption with geomagnetic activity, Planet. Space Sci., 14, 991, 1966.

Heppner, J. P., Polar cap electric field distributions related to the Interplanetary Magnetic Field direction, J. Geophys. Res., 77, 4877, 1972.

Heppner, J. P., Empirical models of high-latitude electric fields, J. Geophys. Res., 82, 1115, 1977.

Heppner, J. P., J. D. Stolarik, and E. M. Wescott, Electric-field measurements and the identification of currents causing magnetic disturbances in the polar cap, J. Geophys. Res., 76, 6028, 1971.

Horwitz, J. L., and S.-I. Akasofu, On the relationship of the polar cap current system to the north-south component of the interplanetary magnetic field, J. Geophys. Res., 84, 2567, 1979.

Hughes, T. J., and G. Rostoker, Current flow in the magnetosphere and ionosphere during periods of moderate activity, J. Geophys. Res., 82, 2271, 1977.

Hughes, T. J., and G. Rostoker, A comprehensive model current system for high-latitude magnetic activity, I, The steady state system, Geophys. J. R. Astron. Soc., 58, 525, 1979.

Iijima, T., Enhancement of the S_q^p field as the basic component of polar magnetic disturbances, Rep. Iono. Space Res. Jap., 27, 199, 1973.

Iijima, T., and T. Nagata, Signatures for substorm development of the growth phase and expansion phase, Planet. Space Sci., 20, 1095, 1972.

Iijima, T., and T. A. Potemra, The amplitude distribution of field-aligned currents at northern high latitudes observed by Triad, J. Geophys. Res., 81, 2165, 1976.

Iijima, T., and T. A. Potemra, Large-scale characteristics of field-aligned currents associated with substorms, J. Geophys. Res., 83, 599, 1978.

Ismail, S., and C.-I. Meng, A classification of polar cap auroral arcs, Planet. Space Sci., 30, 319, 1982.

Kamei, T., and H. Maeda, Auroral electrojet indices (AE) for January-June, 1978, WDC-C2 for Geomag. Data Book No. 3, Kyoto Univ., 1981.

Kamide, Y., The relationship between field-aligned currents and the auroral electrojets: A review, Space Sci. Rev., 31, 127, 1982.

Kamide, Y., B.-H. Ahn, S.-I. Akasofu, W. Baumjohann, E. Friis-Christensen, H. W. Kroehl, H. Maurer, A. D. Richmond, G. Rostoker, R. W. Spiro, J. K. Walker, and A. N. Zaitzev, Global distribution of ionospheric and field-aligned currents during substorms

determined using magnetic data from six IMS meridian chains: Initial results, J. Geophys. Res., 87, 8228, 1982a.

Kamide, Y., and S.-I. Akasofu, Global distribution of the Pedersen and Hall currents and the electric potential pattern during a moderately disturbed period, J. Geophys. Res., 86, 3665, 1981.

Kamide, Y., and S.-I. Akasofu, Notes on the auroral electrojet indices, Rev. Geophys. and Space Phys., submitted, 1982.

Kamide, Y., S.-I. Akasofu, B.-H. Ahn, W. Baumjohann, and J. L. Kisabeth, Total current electrojet estimated from the IMS Alaska meridian chain of magnetic observatories, Planet. Space Sci., 30, 621, 1982b.

Kamide, Y., S.-I. Akasofu, and A. Brekke, Ionospheric currents observed from the Chatanika radar and ground magnetic perturbations at the auroral latitude, Planet. Space Sci., 24, 193, 1976a.

Kamide, Y., and A. Brekke, Auroral electrojet current density deduced from the Chatanika radar and from the Alaska meridian chain of magnetic observatories, J. Geophys. Res., 80, 587, 1975.

Kamide, Y., and N. Fukushima, Positive geomagnetic bays in evening high-latitudes and their possible connection with partial ring current, Rep. Ionos. Space Res. Jap., 26, 79, 1972.

Kamide, Y., M. Kanamitsu, and S.-I. Akasofu, A new method of mapping worldwide potential contours for ground magnetic perturbations: Equivalent ionospheric current representation, J. Geophys. Res., 81, 3810, 1976b.

Kamide, Y., H. W. Kroehl, A. D. Richmond, B.-H. Ahn, S.-I. Akasofu, W. Baumjohann, E. Friis-Christensen, S. Matsushita, H. Maurer, G. Rostoker, R. W. Spiro, J. K. Walker and A. N. Zaitzev, Changes in the global electric fields and currents for March 17-19, 1978 from six IMS meridian chains of magnetometers, WDC-A Report UAG-87, 1982c.

Kamide, Y., and S. Matsushita, Simulation studies of ionospheric electric fields and currents in relation to field-aligned currents, 1, Quiet periods, J. Geophys. Res., 81, 3999, 1976.

Kamide, Y., and S. Matsushita, Simulation studies of ionospheric electric fields and currents in relation to field-aligned currents, 1. Quiet periods, J. Geophys. Res., 84, 4083, 1979a.

Kamide, Y., and S. Matsushita, Simulation studies of ionospheric electric fields and currents in relation to field-aligned currents, 2. Substorms, J. Geophys. Res., 84, 4099, 1979b.

Kamide, Y., P. D. Perreault, S.-I. Akasofu, and J. D. Winningham, Dependence of substorm occurrence probability on the interplanetary magnetic field on the size of the auroral oval, J. Geophys. Res., 82, 5521, 1977.

Kamide, Y., and A. D. Richmond, Ionospheric conductivity dependence of electric fields and currents estimated from ground magnetic observations, J. Geophys. Res., 87, 8331, 1982.

Kamide, Y., A. D. Richmond, and S. Matsushita, Estimation of ionospheric electric field, ionospheric currents, and field-aligned currents from ground magnetic records, J. Geophys Res., 86, 801, 1981.

Kamide, Y., and J. F. Vickrey, Relative contribution of ionospheric conductivity and electric field to the auroral electrojets, preprint, 1982.

Kawasaki, K., and S.-I. Akasofu, Polar solar daily geomagnetic variations on exceptionally quiet days, J. Geophys. Res., 72, 5363, 1967.

King, J. H., Interplanetary Medium Data Book, NSSDC, Goddard Space Flight Center, NASA, 1980.

Kisabeth, J. L., On calculating magnetic and vector potential fields due to large-scale magnetospheric current systems and induced currents in an infinitely conducting earth, in Quantitative Modeling of Magnetospheric Processes, Geophys. Monogr. Ser., 21, 473, ed. by W. P. Olson, Washington, D.C., 1979.

Kisabeth, J. L., and G. Rostoker, Development of the polar electrojet during polar magnetic substorms, J. Geophys. Res., 76, 6815, 1971.

Kokubun, S., Polar substorm development and interplanetary magnetic field, Planet. Space Sci., 19, 697, 1971.

Kokubun, S., and T. Iijima, Time-sequence of polar magnetic substorms, Planet. Space Sci., 23, 1483, 1975.

Kroehl, H. W., and A. D. Richmond, Magnetic substorm characteristics described by magnetic potential maps for 26-28 March 1976, Dynamics of the magnetosphere, edited by S.-I. Akasofu, pp. 269-286, D. Reidel, Hingham, Mass., 1980.

Lassen, K., Polar cap emissions, Atmospheric Emissions, ed. by B. M. McCormac and A. Omholt, p. 63, Reinhold, New York, 1969.

Lassen, K., On the classification of high latitude auroras, Geofys. Pub., 29, 87, 1972.

Lassen, K., The quiet-time pattern of auroral arcs as a consequence of magnetosphere convection, Det. Danske Meteor. Inst., R-56, Copenhagen, August, 1979.

Lassen, K., and C. Danielson, Quiet time pattern of auroral arcs for different directions of interplanetary magnetic field in the Y-Z plane, J. Geophys. Res., 83, 5277, 1978.

Maezawa, K., Magnetospheric convection induced by the positive and negative Z components of the interplanetary magnetic field: Quantitative analysis using polar cap magnetic records, J. Geophys. Res., 81, 2289, 1976.

McPherron, R. L., Growth phase of magnetospheric substorms, J. Geophys. Res., 75, 5592, 1970.

Mehta, N. C., Ionospheric electrodynamics and its coupling to the magnetosphere, Ph.D. thesis, University of California, San Diego, 1979.

Meng, C.-I., and S.-I. Akasofu, A study of polar magnetic substorms, 2. Three-dimensional current system, J. Geophys. Res., 78, 4035, 1969.

Meng, C.-I., and S.-I. Akasofu, The relation between the polar cap auroral arc and the auroral oval arc, J. Geophys. Res., 81, 4004, 1976.

Mishin, V. M., A. D. Bazarzhapov, and G. B. Shpynev, Electric fields and currents in the earth's magnetosphere, in Dynamics of the

Magnetosphere, edited by S.-I. Akasofu, pp. 249-268, D. Reidel, Hingham, Mass., 1980.

Murdin, J., and A. Brekke, Chatanika incoherent scatter radar measurements: A three day experiment, KGI Report No. 80:1, Kiruna, Sweden, 1980.

Nagata, T., and S. Kokubun, A particular geomagnetic daily variation (S_q^D) in the polar regions on geomagnetically quiet days, Nature, 195, 555, 1962.

Nisbet, J. S., Relations between the Birkeland currents, the auroral electrojet indices and high latitude Joule heating, J. Atmos. Terr. Phys., 44, 797, 1982.

Nishida, A., Coherence geomagnetic DP2 fluctuation with interplanetary magnetic variations, J. Geophys. Res., 73, 5549, 1968.

Nishida, A., N. Iwasaki, and T. Nagata, The origin of fluctuations in the equatorial electrojet: A new type of geomagnetic variation, Ann. Geophys., 22, 478, 1966.

Nishida, A., and Y. Kamide, Magnetospheric processes preceding the onset of an isolated substorm, a case study of the March 31, 1978 substorm, preprint, 1982.

Obayashi, T., and A. Nishida, Large-scale electric field in the magnetosphere, Space Sci. Rev., 8, 3, 1968.

Pudovkin, M. I., and O. A. Troshichev, On the types of current patterns of weak geomagnetic disturbances at the polar caps, Planet. Space Sci., 20, 1773, 1972.

Rees, M. H., Auroral electrons, Space Sci. Rev., 10, 413, 1969.

Rees, M. H. Magnetospheric substorm energy dissipation in the atmosphere, Planet. Space Sci., 23, 1589, 1975.

Rees, M. H., and J. C. G. Walker, Ion and electron heating by auroral electric fields, Ann. Geophys., 24, 1, 1968.

Richmond, A. D., H. W. Kroehl, M. A. Henning, and Y. Kamide, Magnetic potential plots over the northern hemisphere for 26-28 March 76, WDC-4 Report UAG-71, 1979.

Richmond, A. D., S. Matsushita, and J. D. Tarpley, On the production mechanism of electric currents and field in the ionosphere, J. Geophys. Res., 81, 547, 1976.

Rino, C. L., A. Brekke, and M. J. Baron, High-resolution auroral zone E-region neutral wind and current measurements by incoherent scatter radar, J. Geophys. Res., 82, 2295, 1977.

Rostoker, G., Polar magnetic substorms, Rev. Geophys. and Space Phys., 10, No. 1, 157, 1972.

Rostoker, G., Magnetospheric and ionospheric currents in the polar cusp and their dependence on the B_y component of the interplanetary magnetic field, J. Geophys. Res., 85, 4167, 1980.

Rostoker, G., S.-I. Akasofu, J. Foster, R. A. Greenwald, Y. Kamide, K. Kawasaki, A. T. Y. Lui, R. L. McPherron, and C. T. Russell, Magnetospheric substorms - Definition and signatures, J. Geophys. Res., 85, 1663, 1980.

Rostoker, G., and M. P. Hron, The eastward electrojet in the dawn sector, Planet. Space Sci., 23, 1377, 1975.

Rostoker, G., and T. J. Hughes, A comprehensive model current system from high-latitude magnetic activity, II, The substorm component, Geophys. J. R. Astron. Soc., 58, 571, 1979.

Sharp, R. D., and R. E. Johnson, Some average properties of auroral electron precipitation from satellite observations, J. Geophys. Res., 73, 969, 1968.

Silsbee, H. C., and E. H. Vestine, Geomagnetic bays, their occurrence frequency and current systems, Terr. Magn. Atmos. Elec., 47, 195, 1942.

Spiro, R. W., D. H. Reiff, and L. J. Mather, Jr., Precipitating electron average flux and auroral zone conductances-an empirical model, J. Geophys. Res., 87, 8215, 1982.

Stubbe, P., Frictional forces and collision frequencies between moving ion and neutral gases, J. Atmos. Terr. Phys., 30, 1965, 1968.

Svalgaard, L., Sector structure of the interplanetary magnetic field and daily variation of the geomagnetic field at high latitudes, Pap. 6, Dansk. Meteorol. Inst. Geophys., Charlottenlund, Denmark, 1968.

Svalgaard, L., Interplanetary magnetic-sector structure, 1926-1971, J. Geophys. Res., 77, 4027, 1972.

Svalgaard, L., Polar cap magnetic variations and their relationship with the interplanetary magnetic-sector structure, J. Geophys. Res., 78, 2064, 1973.

Tarpley, J. D., The ionospheric wind dynamo, 1, Lunar Tide, Planet. Space Sci., 18, 1075, 1970.

Vanyan, L. L., and I. L. Osipova, The electrical conductivity of the polar ionosphere, Geomag. Aeron., 15, 847, 1976.

Vestine, E. H., and S. Chapman, The electric current system of geomagnetic disturbance, Terr. Magn. Atmos. Elec., 43, 351, 1938.

Vickrey, J. F., R. R. Vondrak, and S. J. Matthews, The diurnal and latitudinal variation of auroral zone ionospheric conductivity, J. Geophys. Res., 86, 65, 1981.

Vickrey, J. F., R. R. Vondrak, and S. J. Matthews, Energy deposition by precipitating particles and joule dissipation in the auroral ionosphere, J. Geophys. Res., 87, 5184, 1982.

Wallis, D. D., and E. E. Budzinski, Empirical models of height integrated conductivities, J. Geophys. Res., 86, 125, 1981.

Wedde, T., J. R. Doupnik, and P. M. Banks, Incoherent scatter radar observations during August 4-7, 1972, Radio Sci., 12, 285, 1977.

Whalen, J. A., Auroral oval plotter and monograph, Environmental Research papers, No. 327, Air Force Cambridge Research Lab., Bedford, Mass., 1970.

Wickwar, V. B., M. J. Baron, and R. D. Sears, Auroral energy input from energetic electrons and joule heating at Chatanika, J. Geophys. Res., 80, 4364, 1975.

Yasuhara, F., Y. Kamide, and S.-I. Akasofu, Field-aligned and ionospheric currents, Planet. Space Sci., 23, 1355, 1975.

Zmuda, A. J., J. H. Martin, and F. T. Heuring, Transverse magnetic disturbances at 1100 km in the auroral region, J. Geophys. Res., 71, 5033, 1966.

Zmuda, A. J., J. C. Armstrong, and F. T. Heuring, Characteristics of transverse magnetic disturbances observed at 1100 km in the auroral oval, J. Geophys. Res., 75, 4757, 1970.